A STUDY OF COMPUTATIONAL FLUID DYNAMICS

APPLIED TO ROOM AIR FLOW

By

JAMES W. WEATHERS

Bachelor of Science

Oklahoma Christian University of Science and Arts

Oklahoma City, Oklahoma

1990

Submitted to the Faculty of the
Graduate College of the
Oklahoma State University
in partial fulfillment of
the requirements for
the Degree of
MASTER OF SCIENCE
May, 1992

A STUDY OF COMPUTATIONAL FLUID DYNAMICS

APPLIED TO ROOM AIR FLOW

Thesis Approved:

_____

Thesis Advisor

_____

_____

_____

Dean of the Graduate College

ACKNOWLEDGMENTS

While it may sound like the acceptance speech for an academy award recipient, there are quite a few people, too numerous to mention, who deserve credit for anything I accomplish, both now and in the future. All I have has been given to me from God and I am eternally grateful that His blessings have come in the form of family and friends who have supported me in all my endeavors.

I am very grateful to my advisor, Dr. Jeff Spitler, for taking a chance on a graduate student with a "less than perfect" grade-point average. Although his technical support and guidance made the project possible, his faith and confidence in me as a person is what I have valued and benefitted from the most.

I would like to thank the other members of my committee, Dr. Chambers and Dr. Lilley. Their insight and wisdom have been invaluable. I would especially like to thank Dr. Lilley for supplying me a copy of his three-dimensional, laminar, constant density fluid flow computer program, which formed the framework on which the present study was based.

"Behind every good man is a good woman." This saying doesn't do justice to the loving support and patience shown by my wife, Anita, over the past few years. Thank you.

TABLE OF CONTENTS

Chapter Page

Chapter Page

LIST OF TABLES

LIST OF FIGURES

Figure Page

NOMENCLATURE

The following list describes the nomenclature and symbols used throughout the report. Any deviations to this list are noted whenever needed in the report. In addition, the SI units are shown in parenthesis for those variables which contain units.

g_i, g_j, g_k	Tensor notation for gravitational acceleration	(m/s^2)
h	Enthalpy	(J/kg)
k	Thermal conductivity	(W/m·K)
k	Turbulent kinetic energy	(m^2/s^2)
k_{in}	Turbulent energy at room inlet	(m^2/s^2)
$k_{i,j,k}$	Turbulent energy at cell (i,j,k)	(m^2/s^2)
t	Time	(s)
x_i, x_j, x_k	Tensor notation for principle directions	
x_n	Normal direction	
q"	Heat flux vector	(J/m^2·s)
u', v', w'	Velocity fluctuations in x, y, and z-directions	(m/s)
y_n	Normal distance	(m)
A	Generic property	
A_{in}, A_{out}	Inlet and outlet cross-sectional areas	(m^2)
C_p	Specific heat	(J/kg·K)
C_μ, C_1, C_2	Constants for the k-ε model	
D	Mass divergence	(1/s)
F_μ, F_1, F_2, E	Empirical functions for the k-ε model	
P	Pressure	(Pa)
$P_{i,j,k}$	Pressure at cell (i,j,k)	(Pa)
R_T	Turbulent Reynolds number	
Ry	Local Reynolds number	
T	Temperature	(K)
T_o	Reference temperature	(K)
$T_{i,j,k}$	Temperature at cell (i,j,k)	(K)
U, V, W	Velocity components in x, y, and z-directions	(m/s)
U_{jet}	Inlet velocity	(m/s)

U_n	Normal Velocity	(m/s)
U_{out}	Outlet velocity	(m/s)
U_t	Tangential velocity	(m/s)
U_i, U_j, U_k	Tensor notation for velocity components	(m/s)
$\overline{U_i}$, $\overline{V_i}$, $\overline{W_i}$	Tensor notation for mean velocity components	(m/s)
$\tilde{U}$, $\tilde{V}$, $\tilde{W}$	Time-advanced velocity values	(m/s)
$U_{i,j,k}$	U velocity at cell (i,j,k)	(m/s)
$V_{i,j,k}$	V velocity at cell (i,j,k)	(m/s)
$W_{i,j,k}$	W velocity at cell (i,j,k)	(m/s)
α	Thermal diffusivity	(m^2/s)
$\hat{\alpha}$	Donor cell coefficient	
β	Thermal expansion coefficient	(1/K)
$\overline{\beta}$	Pressure divisor	
ε	Turbulent energy dissipation rate	(m^2/s^3)
$\varepsilon_{i,j,k}$	Turbulence dissipation rate at cell (i,j,k)	(m^2/s^3)
ε_{in}	Turbulent dissipation rate at room inlet	(m^2/s^3)
ϕ	Generic scalar quantity	
ρ	Density	(kg/m^3)
μ	Dynamic viscosity	(kg/m·s)
ν	Kinematic viscosity	(m^2/s)
ν_t	Turbulent viscosity	(m^2/s)
σ_k, σ_ε	Constants for the k-ε model	
ω	Relaxation factor	
ζ	Constant	
Δx, Δy, Δz	Cell dimensions	(m)
Δt	Time Step	(s)
ΔP	Pressure change or correction	(Pa)
Γ_i	Tensor notation for function in turbulent equation	
Π	Function in turbulent equation	
Θ	Function in turbulent equation	

CHAPTER I

INTRODUCTION

Overview

The accurate prediction of flow behavior within a room may significantly improve heating, ventilation, and air-conditioning (HVAC) design techniques. Successful predictions of room air flow yield such information as velocities, temperatures, and contaminant distributions which are useful to building design and analysis. Ventilation and indoor air quality are only two of the many areas which would benefit by the development and refinement of room air flow modeling.

The nature of room air flow requires the solution of the continuity and momentum (Navier-Stokes) equations in three dimensions. For typical room/system combinations, the flow is at least partially turbulent. Therefore, the solution process should somehow account for turbulence.

Advanced numerical methods and algorithms for the solution of the partial-differential equations governing fluid dynamics have existed for some time [Harlow, 1965;Launder, 1972]. However, the lack of sufficient computational capabilities hindered the existence of turbulent solutions which adequately modelled fluid flow in practical situations [Launder, 1974].

The overwhelming need for turbulent flow solutions has led to the development of numerous turbulent models. Coupled and uncoupled differential and algebraic equations were derived in an effort to approximate the nature of practical turbulent flows.

Recent technological advances in computing capabilities have broadened the potential for applications of numerical prediction in fluid flow. These applications are generally referred to as Computational Fluid Dynamics (CFD) and are increasingly being used to obtain solutions for problems which were previously deemed "unsolvable" due to their complexity or the lack of sufficient computing power.

The goal of this investigation is to research the various modeling techniques applicable in room air flow prediction, including turbulence models. These models would then be implemented in an attempt to evaluate the models through comparison to experimental data.

Fluid Dynamics Theory

This section details the basic fluid dynamic principles and equations which govern and describe the various facets of this project. In every instance, the minimal amount of explanation is presented, as it is assumed that the reader possesses a working knowledge of fluid mechanics. Some steps of the equation derivations have been omitted since derivations are provided in sufficient detail in most fluid mechanics references.

Conservation of Mass and Momentum

If an Eulerian description is applied to a laminar flow field and constant density is assumed, the following continuity (conservation of mass) equation results.

$$\frac{\partial U_i}{\partial x_i} = 0 \qquad (1.1)$$

The conservation of momentum equations are given by Eq(1.2), which is written in conservative form.

$$\frac{\partial U_i}{\partial t} + \frac{\partial}{\partial x_j}(U_i U_j) = -\frac{1}{\rho}\frac{\partial P}{\partial x_i} + g_i + \nu\nabla^2 U_i \qquad (1.2)$$

Energy Equation

If the conservation of energy is considered for a fluid engaged in laminar flow, the following equation represents the transport of heat within the flow field.

$$\frac{\partial T}{\partial t} + \frac{\partial}{\partial x_i}(U_i T) = \alpha(\nabla^2 T) \qquad (1.3)$$

Mean-Value Approach to Turbulence

Before a study of turbulence modeling in room air flow may begin, it is important to develop an understanding of the nature of turbulent flow. Turbulent flow has two primary characteristics, random and chaotic fluctuations in the fluid's velocity, and intense mixing on the macroscopic level.

These fluctuations and mixing create a fluid motion so complex that the exact details of the motion are undeterminable by a direct analytic approach. Therefore, solutions must be obtained using either a statistical or mean-value approach. This study uses theory derived from the mean-value approach.

Although the parameters associated with turbulent flow exhibit random fluctuations, these properties may be expressed instantaneously as the sum of the mean value ($\overline{A}$) and an instantaneous fluctuation (a'). Thus, for any property (A) in a flow field, its instantaneous value may be expressed as

$$A = \overline{A} + a' \qquad (1.4)$$

where the mean value ($\overline{A}$) is defined by the following equation.

$$\overline{A} = \frac{1}{\Delta t}\int_{t_1}^{t_2} A\,dt \tag{1.5}$$

where $\Delta t = t_2 - t_1$

The time increment (Δt) of Eq(1.5) is considered large in comparison to the period of the fluctuations. Because Eq(1.5) is true for any lower limit of the integration, the following equation is true for most practical situations.

$$\frac{\partial \overline{A}}{\partial t} = 0 \tag{1.6}$$

Applying the mean-value theory of Eq(1.4) to the properties within a flow field, the following equations are obtained for the velocity components.

$$\begin{aligned} U &= \overline{U} + u' \\ V &= \overline{V} + v' \\ W &= \overline{W} + w' \end{aligned} \tag{1.7}$$

The density and pressure may also be represented in the same way. However, any changes in density are assumed to be the result of temperature changes within the flow field.

Turbulent Flow Equations - Continuity

If the velocity expressions of Eq(1.7) are substituted into the continuity equation of Eq(1.1), the following equation results after a time average is taken.

$$\frac{\partial \overline{U_i}}{\partial x_i} = 0 \tag{1.8}$$

Subtracting Eq(1.8) from Eq(1.1),

$$\frac{\partial u_i'}{\partial x_i} = 0 \tag{1.9}$$

Thus, both the mean and fluctuating velocity components must individually satisfy the continuity equation. It is important to note that these equations are based strongly on the assumption that no turbulent density fluctuations exist. For most practical flow situations, it is generally sufficient to ignore Eq(1.9) and focus only on the continuity equation of the mean flow [Hinze, 1987].

Turbulent Flow Equations - Momentum

If the velocity expressions of Eq(1.7) are substituted into the momentum equation, Eq(1.2), and a time average is taken, the following equation will result.

$$\frac{\partial \overline{U_i}}{\partial t} + \frac{\partial}{\partial x_j}\left(\overline{U_i}\ \overline{U_j}\right) + \frac{\partial}{\partial x_j}\left(\overline{u_i' u_j'}\right) = -\frac{\partial}{\partial x_i}\left(\frac{P}{\rho}\right) + g_i + \nu\nabla^2\overline{U_i} \tag{1.10}$$

Although the mathematics of this process are anything but trivial, they are omitted. Detailed derivations are provided in several references [Hinze, 1987]. Eq(1.10) may be manipulated slightly to distinguish the right-hand side of the equation as containing both viscous and turbulent (Reynolds) stresses as shown by the following equation.

$$\rho\left(\frac{\partial \overline{U_i}}{\partial t} + \frac{\partial}{\partial x_j}\left(\overline{U_i}\ \overline{U_j}\right)\right) = -\frac{\partial P}{\partial x_i} + \rho g_i + \underbrace{\frac{\partial}{\partial x_j}\left(\mu\frac{\partial \overline{U_i}}{\partial x_j}\right)}_{\text{Viscous stresses}} + \underbrace{\frac{\partial}{\partial x_j}\left(-\rho\,\overline{u_i' u_j'}\right)}_{\text{Reynolds stresses}} \tag{1.11}$$

The fact that these Reynolds stresses consist of correlations of velocity fluctuations render the stresses impossible to solve. This incapacity to predict the correlations is known as the "Closure Problem." As a result, exact solutions are not possible.

Turbulence Modeling Theory

As mentioned in the previous section, the presence of the Closure Problem in turbulent flow poses an intractable problem. In an effort to meet the overwhelming need for computational results of turbulent flows, turbulence models were developed.

Turbulence models consist of a set of several equations which, when solved in conjunction with the proper forms of the momentum and continuity equations, approximate the behavior of the Reynolds stresses. Numerous models have been introduced through the years, with varying degrees of success. The success of a model is determined by the following three criteria.

Accuracy -	The model must be capable of providing solutions which are within tolerable bounds of accepted experimental results and the basic governing equations of fluid dynamics.
Generality -	The model must be capable of being implemented into a wide variety of flow conditions and geometry without requiring significant changes.
Easily - Implemented	Although computational capabilities have significantly increased, overly-complex models may increase the required computational time beyond the limits of feasibility.

Turbulence models are divided into the following classes, based on the number of additional partial-differential equations which must be solved.

Zero Equation - Model	The turbulence is described through the use of algebraic equations. Thus, the only partial differential equations requiring solution are the mean flow continuity and momentum equations.

One Equation - Model	A partial-differential equation for the turbulent velocity scale is solved in addition to the mean flow partial-differential equations.
Two Equation - Model	Two partial-differential equations for the turbulent velocity scales are solved in addition to the mean flow equations.

Although there are numerous models which may be employed, this study makes use of a two-equation model. See Rodi [1980] for descriptions of the other models.

k-ε Turbulence Model

To numerically simulate the turbulent flow, this study uses the k-ε turbulence model. It is a two-equation model which couples differential equations for the turbulent kinetic energy (k) and the turbulence dissipation rate (ε). The mathematics of the model begin by defining the turbulent kinetic energy as

$$k = \frac{1}{2}\overline{u_i u_i} \tag{1.12}$$

The Reynolds stresses of Eq(1.11) are then modelled by the product of a new term, the turbulent viscosity (ν_t), and the mean velocity gradient as shown by

$$\overline{u_i u_j} = \nu_t\left(\frac{\partial U_i}{\partial x_j} + \frac{\partial U_j}{\partial x_i} - \frac{2}{3}k\delta_{ij}\right) \tag{1.13}$$

where δ_{ij} = 1 for i=j
0 for i≠j

If this new expression for the Reynolds stresses is substituted into the momentum equation, the following new equation may be used as the conservation of momentum equation for turbulent flow. Note that the viscous stress is assumed negligible and that the equation is now coupled with the turbulent kinetic energy.

$$\frac{\partial U_i}{\partial t} + \frac{\partial}{\partial x_j}(U_i U_j) = -\frac{\partial}{\partial x_i}\left(\frac{P}{\rho}\right) + g_i + \frac{\partial}{\partial x_j}\left(\nu_t\left(\frac{\partial U_i}{\partial x_j} + \frac{\partial U_j}{\partial x_i}\right) - \frac{2}{3}k\delta_{ij}\right) \qquad (1.14)$$

(Note that the mean velocity values are assumed, and the bars denoting mean velocities have been omitted.)

This turbulent viscosity term (ν_t) is not a property of the fluid in the same way as the Newtonian viscosity. Rather, it is dependent upon the structure of the turbulence in the flow and may differ at various points throughout the flow. The turbulent viscosity may be determined empirically from Eq(1.15). although it is only one of several possible choices for the turbulent viscosity equation.

$$\nu_t = C_\mu \frac{k^2}{\varepsilon} \qquad (1.15)$$

where C_μ = constant (generally 0.09)

The resulting transport equations for the turbulent kinetic energy and its rate of dissipation are shown in the following equations. Again, it must be emphasized that only a very brief summary of this model is being presented. Further detail may be found in Rodi [1980] or Hinze [1987], as these references were used extensively in the development of this summary.

$$\frac{\partial k}{\partial t} + \frac{\partial}{\partial x_j}(U_j k) = \frac{\partial}{\partial x_j}\left(\frac{\nu_t}{\sigma_k}\frac{\partial k}{\partial x_j}\right) + \nu_t\frac{\partial U_i}{\partial x_j}\left(\frac{\partial U_i}{\partial x_j} + \frac{\partial U_j}{\partial x_i}\right) - \varepsilon \qquad (1.16)$$

$$\frac{\partial \varepsilon}{\partial t} + \frac{\partial}{\partial x_j}(U_j \varepsilon) = \frac{\partial}{\partial x_j}\left(\frac{\nu_t}{\sigma_\varepsilon}\frac{\partial \varepsilon}{\partial x_j}\right) + \frac{C_1 \nu_t \varepsilon}{k}\frac{\partial U_i}{\partial x_j}\left(\frac{\partial U_i}{\partial x_j} + \frac{\partial U_j}{\partial x_i}\right) - C_2\frac{\varepsilon^2}{k} \qquad (1.17)$$

It is very important to realize that intermediate steps in the derivation of Eq(1.16) and Eq(1.17) result in the presence of higher order correlations. The unsolvable nature of these correlations is alleviated by modeling the correlations in the equations.

The recommended values of the empirical constants and functions are given in Table 1.1. These values represent what is considered the "standard" k-ε model.

TABLE 1.1

CONSTANTS FOR THE "STANDARD" k-ε MODEL
[Launder, 1974]

C_μ	C_1	C_2	σ_k	σ_ε
0.09	1.44	1.92	1.0	1.3

Justification for k-ε Use

While detailed derivations of other turbulence models are not included, the justification for the use of the k-ε model should be addressed. With all of the potential turbulence models available, it is certainly valid to question the preference of one model over the others.

Because this project's researcher lacks sufficient experience in the area of turbulence modeling, he is forced to rely on the experience of others. As discussed later in the literature review, all the researchers modeling room air flow have used the k-ε model. Some of the researchers commented on the reason for the model's use, while others implied its use due to popularity. This "popularity" argument contains a

reasonable amount of validity. Using the same model as others should allow a better comparison of numerical results, as it eliminates a variable in the experimental process. The model's popularity also reduces the implementation difficulty since there are several references available discussing the numerical aspects of modeling turbulence through the use of the k-ε equations.

Because the k-ε model is a two-equation model, improved accuracy is obtained in comparison to less-complicated models. Researchers investigating some of the primary two-equation models have discovered that only the k-ε model yields experimentally substantiated results for regions far from solid boundaries or walls [Launder, 1974; Launder, et al., 1972]. For the other models to match the results, it was found necessary to replace some of the constants with empirical functions which added to the complexity of the models.

Necessity of Low-Reynolds Number Model

When discussing turbulent flow, it is convenient to mention an additional parameter, the Turbulent Reynolds Number (R_T).

$$R_T = \frac{k^2}{\varepsilon\nu} \tag{1.18}$$

Due to the nature of room air flow, there will always be regions (particularly near the walls) in which this number is quite small. In these regions, the viscous effects become significantly greater than any turbulent effects. Because the standard form of the k-ε model is valid only for high Reynolds number turbulent flows, difficulty arises.

There are two ways in which the fully turbulent k-ε model may be used for low-Reynolds number flow. These methods are known as wall functions and low-Reynolds models.

The wall functions, when used in conjunction with the standard k-ε equations, are intended to reproduce the logarithmic velocity profile of a turbulent boundary layer near the wall. No changes are made to the k-ε equations. Instead, the velocity profile is created through the use of complex expressions imposed as boundary conditions at the walls. Although a detailed derivation and explanation is not included, equations Eq(1.19) - Eq(1.22) represent wall functions introduced by Launder and Spalding [1974]. It is important to note in the following equations that values with the "wall" subscript (w) denote values at the wall, while values of U_t, k, and ε are values at the first node adjacent to the wall.

$$\frac{U_t}{\tau_w/\rho}\left(C_\mu^{1/2}k\right)^{1/2} = \frac{1}{\kappa}\ln\left(\frac{Ey_n\left(C_\mu^{1/2}k\right)^{1/2}}{\nu}\right) \tag{1.19}$$

$$\left(\frac{\nu_t\,\partial k}{\sigma_k \partial y_n}\right)_{wall} = 0 \tag{1.20}$$

$$\varepsilon^* = \frac{\left(C_\mu^{1/2}k\right)^{3/2}}{\kappa y_n}\ln\left(\frac{Ey_n\left(C_\mu^{1/2}k\right)^{1/2}}{\nu}\right) \tag{1.21}$$

$$\varepsilon = \frac{\left(C_\mu^{1/2}k\right)^{3/2}}{\kappa y_n} \tag{1.22}$$

where
- k = von Karman's constant (0.4)
- τ_w = shear stress at the wall
- E = function determined by wall roughness (9.0 for a smooth wall)
- ε* = value of ε used in the k-equation
- ε = value of ε used in the ε-equation

Wall functions have the significant benefits of reducing computational needs as well as allowing the addition of other empirical functions necessary for special boundary conditions. The primary concern with this method is that the high-Reynolds k-ε model with the logarithmic wall functions may not be suitable for use both near the wall and far away from it [Chen, 1990]. In addition, the traditional wall functions may not be appropriate for complex three-dimensional flow.

The second method for describing low-Reynolds number flow involves modifying the standard k-ε equations, making them valid throughout the full range of flow regions (laminar, buffer, and fully turbulent). Changes are made through the addition of the empirical functions F_μ, F_1, F_2, and E, as shown in the following low-Reynolds equations.

$$\frac{\partial k}{\partial t} + \frac{\partial}{\partial x_j}(U_j k) = \frac{\partial}{\partial x_j}\left(\frac{\nu_t \partial k}{\sigma_k \partial x_j}\right) + \nu_t \frac{\partial U_i}{\partial x_j}\left(\frac{\partial U_i}{\partial x_j} + \frac{\partial U_j}{\partial x_i}\right) - \varepsilon \tag{1.23}$$

$$\frac{\partial \varepsilon}{\partial t} + \frac{\partial}{\partial x_j}(U_j \varepsilon) = \frac{\partial}{\partial x_j}\left(\frac{\nu_t \partial \varepsilon}{\sigma_\varepsilon \partial x_j}\right) + \frac{C_1 F_1 \nu_t \varepsilon}{k} \frac{\partial U_i}{\partial x_j}\left(\frac{\partial U_i}{\partial x_j} + \frac{\partial U_j}{\partial x_i}\right) - C_2 F_2 \frac{\varepsilon^2}{k} + E \tag{1.24}$$

$$\nu_t = C_\mu F_\mu \frac{k^2}{\varepsilon} \tag{1.25}$$

$$R_T = \frac{k^2}{\nu\varepsilon} \tag{1.26}$$

$$R_y = \frac{\sqrt{k} y_n}{\nu} \tag{1.27}$$

where y_n = distance normal to the wall (m)

The following table contains the various empirical constants for three of the more popular low-Reynolds number k-ε models. For comparison, values are also given for the standard, high-Reynolds number model.

TABLE 1.2

LOW-REYNOLDS k-ε CONSTANTS
[Patel, 1984]

Model	C_μ	C_1	C_2	σ_k	σ_ε
Standard	0.09	1.44	1.92	1.0	1.3
Launder-Sharma	0.09	1.44	1.92	1.0	1.3
Chien	0.09	1.35	1.8	1.0	1.3
Lam-Bremhorst	0.09	1.44	1.92	1.0	1.3

Table 1.3 contains the values and expressions for the empirical functions which have been added to the original k-ε equations to model low-Reynolds number flow.

TABLE 1.3

LOW-REYNOLDS k-ε FUNCTIONS
[Patel, 1984]

Model	F_μ	F_1	F_2	**E**
Standard	1.0	1.0	1.0	0
Launder-Sharma	$\exp\left(\frac{-3.4}{(1+R_T/50)^2}\right)$	1.0	$1-0.3\exp(-R_T^2)$	$2\nu\nu_t\left(\frac{\partial^2 U}{\partial y_n^2}\right)^2$
Chien	$1 - \exp(-0.0115y^+)$	1.0	$1-0.22\exp\left(-\left(\frac{R_T}{6}\right)^2\right)$	$\frac{-2\nu\varepsilon}{y^2}\exp(-0.5y^+)$

Lam-Bremhorst	$[1 - \exp(-0.0165R_y)]^2 * \left(1 + \frac{20.5}{R_T}\right)$	$1 + \left(\frac{0.05}{F_\mu}\right)^3$	$1 - \exp(-R_T^2)$	0

As shown by Table 1.3, the "standard" k-ε model for fully turbulent flow is a special case of the low-Reynolds equations of Eq(1.23) and Eq(1.24). Therefore, a solution algorithm could easily employ the wall function or low-Reynolds algorithms by simply using the corresponding values of F_μ, F_1, and F_2.

Literature Review

This section presents brief descriptions of the published literature and recorded experimental results in the field of room air flow modeling and prediction. Although the list should not be considered exhaustive, the review should sufficiently represent the advances, findings, and contributions which are of particular relevance to this project.

Spitler

The experimental data used for comparative purposes in this project has been provided by Spitler [1990]. Spitler researched air movement and convective heat transfer using a full-scale 9 x 9 x 15 ft (2.74 x 2.74 x 4.57 m) room with 53 controllable heated panels, two ventilation inlets, and one outlet (see Figure 1.1).

The facility incorporated sixteen omni-directional air speed probes and numerous thermocouples which measured air temperatures within the room, air temperatures entering and leaving the room, and the various surface temperatures necessary in determining the convective fluxes at the walls. These probes obtained measurements at

896 locations within the room, thus providing an experimental grid of approximately 1 ft (0.30 m). Experimental data was collected using the seven room configurations described in Table 1.4.

TABLE 1.4

EXPERIMENTAL CONFIGURATIONS
[Spitler, 1990]

Configuration	Description
1	One inlet on the side wall
2	One square radial diffuser inlet in the ceiling
3	The side wall inlet with area reduced to 1/3
4	The side wall inlet with area reduced to 2/3
5	The side wall inlet with its jet being diverted toward the center of the room
6	The side wall inlet with furniture located in the center of the room
7	The side wall inlet with cabinets located throughout the room

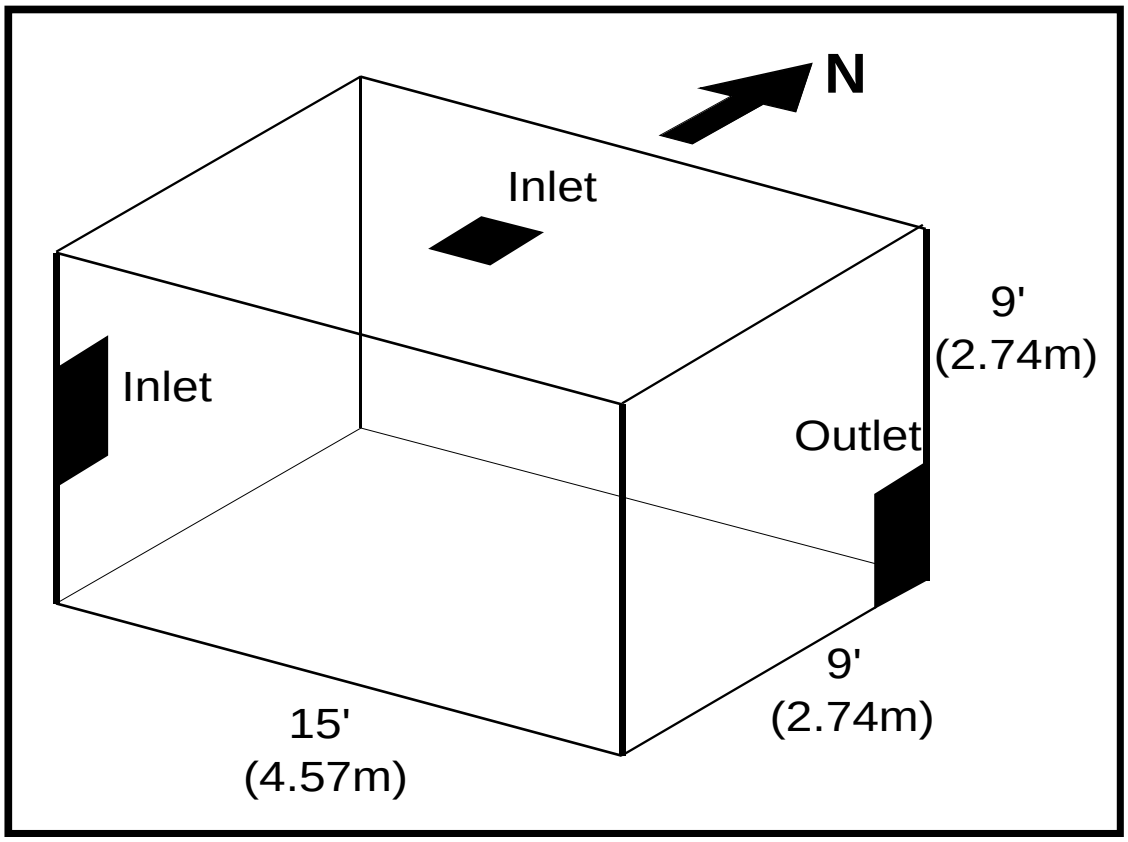

Figure 1.1. Experimental Facility
[Spitler, 1990]

In all of the room configurations, one ventilation outlet located on the east wall was used (see Figure 1.1). The dimensions of the inlets and outlets are shown in Table 1.5.

With the presentation of Table 1.5, it is important to note how inlet dimensions are generally used in room air flow studies to define non-dimensional parameters and distances. Throughout this report, dimensional distances are presented. In addition, results will be presented by defining distances with respect to the inlet width. Thus, $y/W=2$ would correspond to a distance equal to twice the inlet width.

TABLE 1.5

INLET AND OUTLET DIMENSIONS
[Spitler, 1991]

Location	Width (in)	Length (in)	Width (m)	Length (m)
Side Wall Inlet	15.75	35.58	0.40	0.90
Ceiling Inlet	15.75	15.75	0.40	0.40
East Outlet	15.75	35.58	0.40	0.90

The ventilation system was capable of providing between 2 and 100 ACH ("air changes per hour") of ventilation. This corresponds to volumetric flow rates of 40.5 - 2025 cfm (0.019 - 0.945 m^3/s). A total of 44 separate experimental tests were performed, as described in Table 1.6.

The use of the 53 controllable panels is of particular interest to the modeling aspect of this study. By controlling the temperature of the walls, the convective heat fluxes were measured and film coefficients for all surfaces were calculated. This data allows the imposition of temperature boundary conditions which are consistent with experimental data.

TABLE 1.6

EXPERIMENTAL TESTS
[Spitler, 1991]

Configuration	**Inlet Temperature (^oC)**	**Ventilation Rate (ACH)**
1	16, 21, 26	15, 30, 50, 70, 100
2	16, 21, 26	15, 30, 50, 70, 100
3	21	15, 30, 50, 70
4	21	15, 30, 70
5	21	15, 30, 70
6	21	30, 70
7	21	30, 70

Patel

An extensive review of the k-ε model for low Reynolds number flow was compiled by Patel [Patel, 1985]. In addition to the nature and derivation of the model, Patel also detailed the following eight variations or extensions of the model:

- Launder-Sharma
- Hassid-Poreh
- Hoffman
- Dutoya-Michard
- Chien
- Reynolds
- Lam-Bremhorst

In an attempt to compare the models, each model was implemented with the addition of the following equations to numerically predict flow in a two-dimensional boundary layer.

$$\frac{\partial U}{\partial x} + \frac{\partial V}{\partial y} = 0 \qquad (1.28)$$

$$U\frac{\partial U}{\partial x} + V\frac{\partial U}{\partial y} = -\frac{1}{\rho}\frac{\partial P}{\partial x} + \frac{\partial}{\partial y}\left(\nu\frac{\partial U}{\partial y} - \overline{uv}\right) \qquad (1.29)$$

The proposed models of Hassid-Poreh, Hoffman, Dutoya-Michard, and Reynolds failed to reproduce the simple case of this flat-plate boundary layer. Comparable results to experimental data were achieved through the use of the Launder-Sharma, Chien, and Lam-Bremhorst models. Despite these successful results, a refinement to the models was determined necessary if near-wall and low Reynolds number flows were to be calculated. Patel offered the following suggestions:

- Select a damping function for the shear stress which is in agreement with experimental evidence.
- Choose the low Reynolds number functions in the dissipation rate equation with a mathematically consistent near-wall behavior.
- "Fine tune" the functions to ensure that well-published features of wall-bounded shear flows over a range of pressure gradients would be produced.
- Distinct improvement of the predictions for adverse pressure gradient flows would require additional modifications to the high Reynolds number models.

Lam and Bremhorst

Since the emergence of the k-ε turbulence model, numerous researchers have introduced modifications to the basic models, particularly in an attempt to accurately predict low-Reynolds number turbulent flow. Perhaps one of the more significant modifications was introduced by Lam and Bremhorst [Lam & Bremhorst, 1981]. As with the previous models, the turbulent energy and its dissipation rate were modelled using Eq(1.23) and (1.24). The constants being used were the same as the original model: σ_k=1.0, σ_ε=1.3, C_μ=0.09, C_1=1.44, and C_2=1.92.

The primary difference exists in the functions F_μ, F_1, and F_2 in the low-Reynolds equations of Eq(1.23) and Eq(1.24). Previously, the values of these functions were assumed to be equal, or very close to unity. The research of Lam and Bremhorst found these assumptions to be invalid within a laminar or viscous sublayer. A new equation for F_μ was found to be

$$F_\mu = \left(1 - e^{-A_\mu R_y}\right)^2 \left(1 + \frac{A_t}{R_t}\right) \tag{1.30}$$

where A_μ = constant (0.0165)
A_t = constant (20.5)

This new equation is directly influenced by the presence of a wall, as F_μ will approach unity at large distances from a wall for increasingly high levels of turbulence. The proposed equation for F_1 was

$$F_1 = 1 + \left(\frac{0.05}{F_\mu}\right)^3 \tag{1.31}$$

Investigation showed that if F_1 was equal to unity, as previously assumed, additional terms would be required in the k-ε equations to yield reasonable results. In an effort to produce an equation which approaches zero as R_T approaches zero, the following equation for F_2 was introduced.

$$F_2 = 1 - e^{-(R_T)^2} \tag{1.32}$$

This new low-Reynolds form of the k-e model was tested by applying the technique to the case of fully developed turbulent pipe flow. Strong agreement was found with the experimental data. The principle advantage, as emphasized by the researchers, is that the presence of a wall function formula is not required.

Chen

As discussed earlier, one of the particular difficulties with modeling room air flow is that the k-ε model, although suitable for fully turbulent flow, requires the use of empirical functions near the wall. Chen explored the wall function problem as he attempted to accurately prediction low-Reynolds, turbulent, buoyant flow [Chen, 1990]. Chen used the Lam-Bremhorst version of the k-ε model [Lam & Bremhorst, 1981] to predict natural convection flow within cavities. This version of the model was chosen based on recommendations by previous researchers [Patel, 1985] and its relative ease of implementation into a computer algorithm. It was assumed that any temperature gradients within the cavity were small, therefore the use of Boussinesq approximation for buoyancy was performed through the addition of the following term in the momentum equations.

$$\beta g_i(T - T_o) \tag{1.33}$$

The effects of buoyancy in the turbulence equations were approximated using the following terms in the k-ε equations.

$$S_k = \frac{\beta \nu_t \partial(T-T_o)}{\sigma_h \quad \partial x_i} g_i \tag{1.34}$$

$$S_\varepsilon = \frac{1.44\varepsilon}{k} S_k \tag{1.35}$$

These source terms would then be included in the right-hand side of Eq(1.23) and Eq(1.24).

The first of the two simulations was performed on a small-scale, water-filled cavity. The second simulation was made on a full-scale, air filled cavity. The resulting velocity profiles were in good agreement with the measured values. However, the high-Reynolds number k-ε model with wall functions produced results which differed by as much as 61% from the experimental results.

Awbi

Perhaps the most significant application of CFD analysis in room air flow may be in the area of ventilation. Studies have shown that the thermal condition within a room is dependent on the turbulence intensity of the air motion and frequency of flow fluctuations, in addition to the air velocity and temperature distributions. Awbi presented numerical studies of various ventilation configurations through the use of CFD [Awbi, 1989].

Using the standard k-ε model, coupled with logarithmic wall functions, simulations were performed on the ventilation of both two and three-dimensional enclosures. Other simulations involved creating a fixed or constant load within the room to better investigate the effects of buoyancy. The numerical solutions produced reasonably good predictions of the velocity vectors within the room when compared to experimental results. Awbi carefully noted, though, that considerably more studies are necessary if CFD techniques are to be used as design tools with any degree of confidence.

Murakami, et al.

Murakami, et al. from the University of Tokyo, have contributed greatly to the study of numerically modeling room air flow. Each study has emphasized different facets of the overall problem, thus providing a better insight concerning the potential for CFD in ventilation design and analysis.

The first investigations were performed with the intention of verifying the validity of a three-dimensional numerical simulation for turbulence [Murakami, et al., 1987]. Simulations were performed and compared to experimental rooms with a 1:6 scale. The experimental rooms were scaled so that the Reynolds number would be identical to a full scale room based on the following equation.

$$R_e = \frac{U_o L_o}{\nu} \tag{1.36}$$

where U_o = inlet velocity (m/s)
L_o = width of the supply outlet (m)

The flow domain was covered with a rectangular mesh. Later investigations employed the use of boundary-fitted curvilinear coordinate systems [Murakami, et al., 1989a]. The air temperature was assumed to be completely uniform. Thus, buoyant effects were completely ignored. The high-Reynolds k-ε equations (Eq(1.16) and Eq(1.17)) were solved in conjunction with the momentum equation of Eq(1.14). The standard values for the equation constants were used and wall functions were used to simulate viscous effects near the wall.

The numerical simulations were reported to correspond "fairly good" with the experimental results from the scaled room.

Later investigations focused on the diffusion of particles within a ventilated room, with particular emphasis on the design and analysis of clean rooms [Murakami, et al., 1989b, 1990]. The same sets of equations and wall functions were used to analyze other scaled room configurations.

Scaling the room based on the inlet velocity and inlet width is questionable when investigating turbulent room air flow. Scaling in this way does not insure identical turbulent Reynolds numbers. In addition, the development of turbulent jets is based on other parameters which are completely independent of the Reynolds number at the inlet.

Objectives

The primary objective of this project is to evaluate the usefulness of computational fluid dynamic techniques in modeling room air flow. This evaluation process involves the implementation of the two models available for modeling turbulent air flow, in addition to a laminar flow algorithm. Through comparison to experimental data, model limitations, weaknesses, and strengths may be determined.

The secondary objective of the project is to investigate the potential usefulness of CFD analysis for building designers. Typically, the error of a simulation is in some way inversely proportional to the necessary computational resources (i.e., reducing the error requires greater computing resources). Obviously, simulations must be provided within tolerable limits of error. Depending upon the application, however, relatively simple models may provide acceptable results at reduced computing costs. This project will address these trade-offs between accuracy and computational resources.

CHAPTER II

SOLUTION METHODOLOGY

This chapter details the solution methodology for the project including discussions on discretization, grid selection, solution algorithm, and boundary conditions.

This methodology was implemented through the development of a Fortran 77 computer program capable of modeling three-dimensional, turbulent, buoyant flow using finite-difference techniques. The basis of this new program was a program previously developed for three-dimensional, laminar, constant density flow by Lilley [1988], in which the analysis and finite-difference methods are documented. These details for the p-u-v-w solution were implemented in the original laminar, constant density code [Lilley, 1991], which formed the framework on which the present study is based - the extension to turbulent flows via the two-equation k-ε model and the inclusion of buoyancy via the Boussinesq approximation.

Marker-and-Cell Representation

This investigation uses the Marker-and-Cell (MAC) method of defining variables within a flow field [Harlow & Welch, 1965]. For a given cell of dimensions Δx, Δy, and Δz, velocities are defined on the center of cell faces, while scalar quantities are defined at the center of the cell as shown in Figure 2.1.

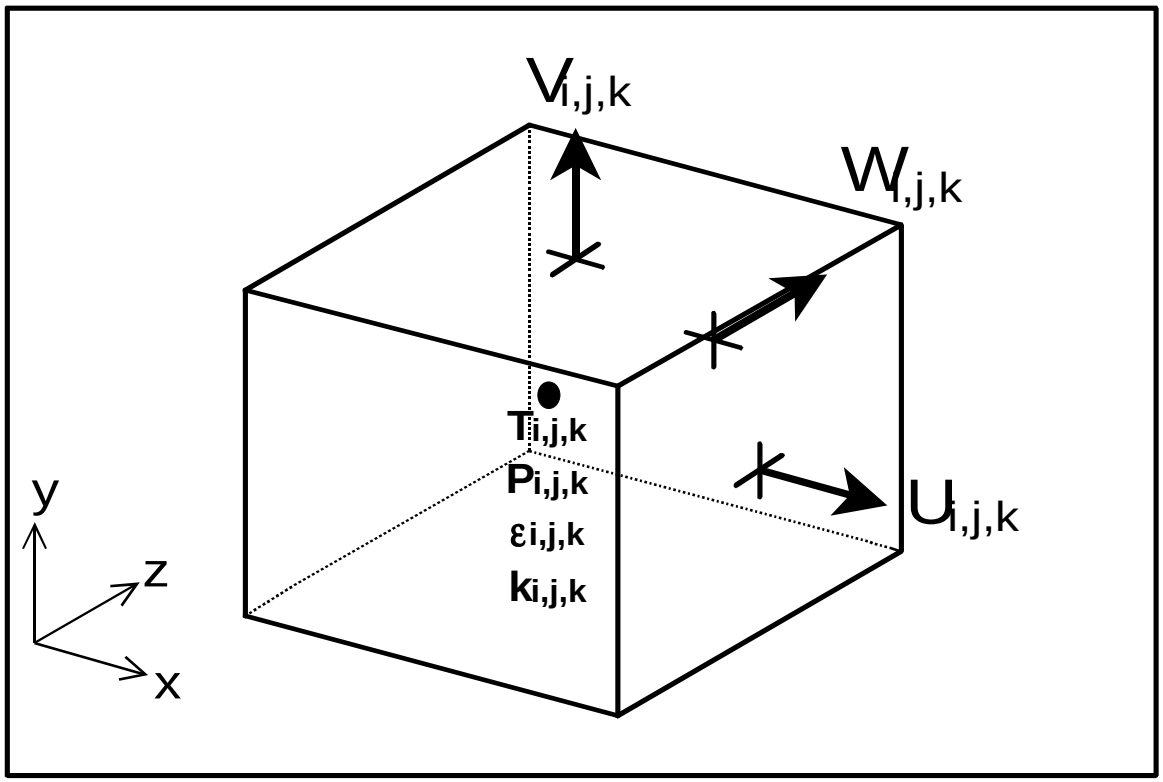

Figure 2.1. Marker-and-Cell Representation

Finite-Difference Approximations - Laminar Flow

Because the forms of the momentum and transport equations differ based on the nature of the flow, the resulting finite-difference equations will differ for laminar and turbulent flow. For this reason, the discussions on these representations will be presented separately. The finite-difference solution of the laminar flow equations is important for two reasons. First, some of the terms in the complex turbulent equations are identical to terms in the laminar equations. Thus, solution representations and algorithms may be easily developed for laminar flows before implementing the terms into the solution of the turbulent equations. Secondly, this project will investigate the simulation of the air flow

using the laminar equations. This will allow conclusions to be drawn concerning how well the laminar equations approximate the room air flow.

While several methods of approximating the continuity and momentum equations have been proposed, this study makes use of a method introduced by the Los Alamos Laboratory [Hirt, et al., 1975], a report which detailed the simplicity of the solution of laminar, time-dependent, incompressible fluid flow problems in two-dimensions. Its extension to three-dimensional flow was well-documented by Lilley [1988] with details incorporated into his computer code [Lilley, 1991], which formed the starting point of the present study.

Continuity Equation

The finite difference representation of the continuity equation, Eq(1.1), is shown by the following equation. For simplicity, tensor notation is dropped whenever finite-difference representations are discussed.

$$\frac{1}{\Delta x}(U_{i,j,k} - U_{i-1,j,k}) + \frac{1}{\Delta y}(V_{i,j,k} - V_{i,j-1,k}) + \frac{1}{\Delta z}(W_{i,j,k} - W_{i,j,k-1}) = 0 \qquad (2.1)$$

Momentum Equations

The momentum equations, Eq(1.2), can be manipulated to form explicit equations for the time-advanced velocity components. Using the original authors' notation for two-dimensional problems [Hirt, et al., 1975], Eq(1.2) is rearranged to form an explicit formulation for the time-advanced values of the x-component velocity (U) in the present three-dimensional problem. Similar expressions for the other velocity components are omitted in the interest of space, as they are provided in Appendix A.

$$\tilde{U}_{i,j,k} = U_{i,j,k} + \Delta t\left(\frac{1}{\Delta x}(P_{i,j,k} - P_{i+1,j,k}) + g_x + \text{VISX} - \text{FUX} - \text{FUY} - \text{FUZ}\right) \tag{2.2}$$

Note that the terms over-scored with the tilde (~), denote any value at time $t=t+\Delta t$. The convective (FUX, FUY, FUZ) and viscous (VISZ) fluxes are defined by the following equations. The details for constant density three-dimensional laminar flows have been incorporated in an early study [Lilley, 1988] and the original computer code [Lilley, 1991].

$$\text{FUX} = \frac{1}{4\Delta x}\Big\{(U_{i,j,k}+U_{i+1,j,k})^2 + \hat{\alpha}|U_{i,j,k}+U_{i+1,j,k}|(U_{i,j,k}-U_{i+1,j,k}) - (U_{i-1,j,k}+U_{i,j,k})^2 - \hat{\alpha}|U_{i-1,j,k}+U_{i,j,k}|(U_{i-1,j,k}-U_{i,j,k})\Big\} \tag{2.3}$$

$$\text{FUY} = \frac{1}{4\Delta y}\Big\{(V_{i,j,k}+V_{i+1,j,k})(U_{i,j,k}+U_{i,j+1,k}) + \hat{\alpha}|V_{i,j,k}+V_{i+1,j,k}|(U_{i,j,k}-U_{i,j+1,k}) - (V_{i,j-1,k}+V_{i+1,j-1,k})(U_{i,j-1,k}+U_{i,j,k}) - \hat{\alpha}|V_{i,j-1,k}+V_{i+1,j-1,k}|(U_{i,j-1,k}-U_{i,j,k})\Big\} \tag{2.4}$$

$$\text{FUZ} = \frac{1}{4\Delta z}\Big\{(W_{i,j,k}+W_{i+1,j,k})(U_{i,j,k}+U_{i,j,k+1}) + \hat{\alpha}|W_{i,j,k}+W_{i+1,j,k}|(U_{i,j,k}-U_{i,j,k+1}) - (W_{i,j,k-1}+W_{i+1,j,k-1})(U_{i,j,k-1}+U_{i,j,k}) - \hat{\alpha}|W_{i,j,k-1}+W_{i+1,j,k-1}|(U_{i,j,k-1}-U_{i,j,k})\Big\} \tag{2.5}$$

$$\text{VISX} = \nu\Big\{\frac{1}{\Delta x^2}(U_{i+1,j,k}-2U_{i,j,k}+U_{i-1,j,k}) + \frac{1}{\Delta y^2}(U_{i,j+1,k}-2U_{i,j,k}+U_{i,j-1,k}) + \frac{1}{\Delta z^2}(U_{i,j,k+1}-2U_{i,j,k}+U_{i,j,k-1})\Big\} \tag{2.6}$$

The donor-cell coefficient ($\hat{\alpha}$) in the above equations represents the amount of upstream differencing which is used when determining the first-derivatives of the convective terms. The introduction of the coefficient is used to insure numerical stability without avoidable round-off errors. The necessary level of upstream differencing may be performed by using the following equation [Lilley, 1988].

$$\hat{\alpha} = \zeta \cdot \max\left\{\frac{|U|\Delta t}{\Delta x} : \frac{|V|\Delta t}{\Delta y} : \frac{|W|\Delta t}{\Delta z}\right\} \tag{2.7}$$

where $1.2 < \zeta < 1.5$

Scalar Quantities

For any scalar quantity, ϕ, the same types of equations as Eqs(2.2-2.6) may be employed to obtain an explicit equation for time-advanced scalar quantities. For example, the heat transport equation of Eq(1.3) may be approximated by the following set of equations.

$$\tilde{T}_{i,j,k} = T_{i,j,k} + \Delta t(\text{VIST} - \text{FTX} - \text{FTY} - \text{FTZ}) \tag{2.8}$$

where:

$$\text{FTX} = \frac{1}{2\Delta x}\Big\{U_{i,j,k}(T_{i,j,k} + T_{i+1,j,k}) + \hat{\alpha}|U_{i,j,k}|(T_{i,j,k} - T_{i+1,j,k}) - U_{i-1,j,k}(T_{i-1,j,k} + T_{i,j,k}) - \hat{\alpha}|U_{i-1,j,k}|(T_{i-1,j,k}-T_{i,j,k})\Big\} \tag{2.9}$$

$$\text{FTY} = \frac{1}{2\Delta y}\Big\{V_{i,j,k}(T_{i,j,k} + T_{i+1,j,k}) + \hat{\alpha}|V_{i,j,k}|(T_{i,j,k} - T_{i+1,j,k}) - V_{i-1,j,k}(T_{i-1,j,k} + T_{i,j,k}) - \hat{\alpha}|V_{i-1,j,k}|(T_{i-1,j,k}-T_{i,j,k})\Big\} \tag{2.10}$$

$$\text{FTZ} = \frac{1}{2\Delta z}\Big\{W_{i,j,k}(T_{i,j,k} + T_{i+1,j,k}) + \hat{\alpha}|W_{i,j,k}|(T_{i,j,k} - T_{i+1,j,k}) - W_{i-1,j,k}(T_{i-1,j,k} + T_{i,j,k}) - \hat{\alpha}|W_{i-1,j,k}|(T_{i-1,j,k}-T_{i,j,k})\Big\} \tag{2.11}$$

$$\text{VIST} = \alpha\Big\{\frac{1}{\Delta x^2}(T_{i+1,j,k}-2T_{i,j,k}+T_{i-1,j,k}) + \frac{1}{\Delta y^2}(T_{i,j+1,k}-2T_{i,j,k}+T_{i,j-1,k}) + \frac{1}{\Delta z^2}(T_{i,j,k+1}-2T_{i,j,k}+T_{i,j,k-1})\Big\} \tag{2.12}$$

The value of $\hat{\alpha}$ in the above equations is the same value as was determined in the previous section.

Buoyancy

The Boussinesq approximation is used to simulate the effects of buoyancy. The basis of this approximation is that while constant density may be used in the solution process, changes in density due to temperature differences may be modelled through the use of a coefficient of thermal expansion. In any, or all, of the momentum equations, the following term may replace the existing term representing exterior forces due to gravity.

$$\beta g_i(T - T_o) \tag{2.13}$$

Typically, in a transient analysis, the reference temperature, T_o, is given the value of the temperature within the room at time t=0. Using this approximation, Eq(2.2) for the y-component of velocity (V) would include the following term on the right-hand side.

$$\beta g_y(T_{i,j,k} - T_o) \tag{2.14}$$

Finite Difference Approximations - Turbulent Flow

As mentioned previously, the turbulent equations require different finite-difference representations than those approximating the laminar flow. Because the mean velocity values need only to be considered when imposing the continuity equation, the finite-difference equation of Eq(2.1) may be used to impose the conservation of mass for turbulent, as well as laminar flow.

Momentum Equations

For convenience and ease of implementation into a numerical scheme, the momentum equations derived for turbulent flow, Eq(1.4), will be re-written using a new term, Γ_i.

$$\frac{\partial U_i}{\partial t} + \frac{\partial}{\partial x_j}(U_i U_j) = - \frac{\partial}{\partial x_i}\left(\frac{P}{\rho}\right) + g_i + \Gamma_i \tag{2.15}$$

where

$$\Gamma_i = \frac{\partial}{\partial x_j}\left(\nu_t \left(\frac{\partial U_i}{\partial x_j} + \frac{\partial U_j}{\partial x_i} \right) - \frac{2}{3} k \delta_{ij} \right) \tag{2.16}$$

This new momentum equation may be easily manipulated to form explicit equations for the time-advanced velocities. Using notation consistent with finite-difference approximations, the following equation may be written for the x-component of velocity (U).

$$\tilde{U}_{i,j,k} = U_{i,j,k} + \Delta t\left(\frac{1}{\Delta x}(P_{i,j,k} - P_{i+1,j,k}) + g_x + \text{GAMMAX} - \text{FUX} - \text{FUY} - \text{FUZ}\right) \tag{2.17}$$

Because the convective terms FUX, FUY, and FUZ are identical to the terms detailed previously, they may be determined from the equations Eq(2.3), Eq(2.4), and Eq(2.5). The finite-difference representation of the term, Γ_i, is not included in this section. This term and other terms which will be introduced later, are comprised of a complex arrangement of first and second derivatives. For this reason, finite-difference discussions for each of these terms and functions is presented in Appendix B.

Turbulent Energy Equation

For simplicity, the turbulent energy equation for low-Reynolds flow, Eq(1.19), is re-written through the use of a new term (Π) and a new function (Θ).

$$\frac{\partial k}{\partial t} + \frac{\partial}{\partial x_j}(U_j k) = \Theta(k) + \nu_t \Pi - \varepsilon \tag{2.18}$$

where Π and Θ are defined by

$$\Pi = \frac{\partial U_i}{\partial x_j}\left(\frac{\partial U_i}{\partial x_j} + \frac{\partial U_j}{\partial x_i}\right) \tag{2.19}$$

$$\Theta(k) = \frac{\partial}{\partial x_j}\left(\frac{\nu_t \, \partial k}{\sigma_k \partial x_j}\right) \tag{2.20}$$

Time-advanced values for the turbulent energy may be determined explicitly from the following equation.

$$\tilde{k}_{i,j,k} = k_{i,j,k} + \Delta t(\text{THETAK} + \nu_t \cdot \text{PI} - \text{FKX} - \text{FKY} - \text{FKZ} - \varepsilon) \tag{2.21}$$

Because the turbulent energy (k) is a scalar quantity, the terms FKX, FKY, and FKZ may be determined from the equations similar to Eq(2.9), (2.10), and (2.11). Because the new terms of Π and Θ are similar in nature to Γ_i, the finite-difference representations of Π and Θ are also given in Appendix B.

Turbulent Energy Dissipation Equation

Similar to the turbulent energy, the equation for the dissipation of turbulent energy may be written as

$$\frac{\partial \varepsilon}{\partial t} + \frac{\partial}{\partial x_j}(U_j \varepsilon) = \Theta(\varepsilon) + \frac{C_1 F_1 \nu_t \varepsilon}{k} \Pi - C_2 F_2 \frac{\varepsilon^2}{k} + E \qquad (2.22)$$

The time-advanced values of the turbulent energy dissipation may then be determined explicitly from the following equation.

$$\tilde{\varepsilon}_{i,j,k} = \varepsilon_{i,j,k} + \Delta t \left(\text{THETAE} + \frac{C_1 F_1 \nu_t \varepsilon}{k} \text{PI} - C_2 F_2 \frac{\varepsilon^2}{k} + E - \text{FEX} - \text{FEY} - \text{FEZ} \right) \qquad (2.23)$$

Solution Procedure

Now that the finite-difference issues have been addressed, the numerical scheme or algorithm by which the equations are solved, may be discussed.

Time Step Selection

This project uses a solution algorithm which is completely explicit. Simply stated, this means that the time-advanced values ($t=t_1+\Delta t$) are determined from values and derivatives evaluated at the previous time ($t=t_1$). Because the method is explicit, restrictions must be placed on the size of the time step to insure numerical stability.

The first time step criterion is based on the obvious condition that material should not be allowed to move a distance greater than the cell size over a given time step. This criterion is sometimes referred to as the "cell transit time" and is given by the following equation.

$$(\Delta t)_1 = \zeta \cdot \min\left\{\frac{\Delta x}{|U_{max}|} : \frac{\Delta y}{|V_{max}|} : \frac{\Delta z}{|W_{max}|}\right\} \tag{2.24}$$

where $\frac{1}{4} < \zeta < \frac{1}{3}$

The second criterion maintains that if the kinematic viscosity is considered non-zero, momentum cannot diffuse more than one cell during a time step. Therefore,

$$(\Delta t)_2 = \frac{1}{2\nu} \cdot \min\left\{((\Delta x)^2 : (\Delta y)^2 : (\Delta z)^2)\right\} \tag{2.25}$$

Similarly,

$$(\Delta t)_3 = \frac{1}{2\nu}\left(\frac{1}{(\Delta x)^2} + \frac{1}{(\Delta y)^2} + \frac{1}{(\Delta z)^2}\right)^{-1} \tag{2.26}$$

When the energy equation is used to determine temperature values and model buoyancy, the following additional criterion must be enforced [Hirt & Cook, 1972]. This imposes the condition that heat cannot diffuse more than one cell during a given time step.

$$(\Delta t)_4 = \frac{1}{2\alpha}\left(\frac{1}{(\Delta x)^2} + \frac{1}{(\Delta y)^2} + \frac{1}{(\Delta z)^2}\right)^{-1} \tag{2.27}$$

Because each of these time step criteria must be met, the overall time step for the simulation is taken as the minimum value of all imposed criteria.

Laminar Solution Algorithm

Several methods exist for the simultaneous solution of the continuity and momentum equations. The computer programs developed for this project employ a method introduced by Hirt and Cook [1972].

Equation Eq(2.2) may be used to obtain time-advanced velocities. These new velocities may, or may not, satisfy the continuity equation. The mass divergence (D) at each cell may be calculated using the continuity equation as

$$D = \frac{1}{\Delta x}(\tilde{U}_{i,j,k} - \tilde{U}_{i-1,j,k}) + \frac{1}{\Delta y}(\tilde{V}_{i,j,k} - \tilde{V}_{i,j-1,k}) + \frac{1}{\Delta z}(\tilde{W}_{i,j,k} - \tilde{W}_{i,j,k-1}) \qquad (2.28)$$

Because the flow is assumed to be incompressible, the value of |D| must be smaller than some prescribed value to insure that the time-advanced velocities satisfy the continuity equation. If |D| is greater than the acceptable value, the cell pressure is corrected by the following amount.

$$\Delta P = - \overline{\beta}\, D \qquad (2.29)$$

where

$$\overline{\beta} = \frac{\omega}{2\Delta t}\left(\frac{1}{(\Delta x)^2} + \frac{1}{(\Delta y)^2} + \frac{1}{(\Delta z)^2}\right)^{-1} \qquad (2.30)$$

ω is a relaxation factor ($1 < \omega < 2$) which is used to accelerate the pressure convergence process.

The new velocity values at the new time step may then be updated using the following equations.

$$\tilde{U}_{i,j,k_{NEW}} = \tilde{U}_{i,j,k_{OLD}} + \frac{\Delta P \Delta t}{\Delta x} \tag{2.31}$$

$$\tilde{U}_{i-1,j,k_{NEW}} = \tilde{U}_{i-1,j,k_{OLD}} - \frac{\Delta P \Delta t}{\Delta x} \tag{2.32}$$

$$\tilde{V}_{i,j,k_{NEW}} = \tilde{V}_{i,j,k_{OLD}} + \frac{\Delta P \Delta t}{\Delta y} \tag{2.33}$$

$$\tilde{V}_{i,j-1,k_{NEW}} = \tilde{V}_{i,j-1,k_{OLD}} + \frac{\Delta P \Delta t}{\Delta y} \tag{2.34}$$

$$\tilde{W}_{i,j,k_{NEW}} = \tilde{W}_{i,j,k_{OLD}} + \frac{\Delta P \Delta t}{\Delta z} \tag{2.35}$$

$$\tilde{W}_{i,j,k-1_{NEW}} = \tilde{W}_{i,j,k-1_{OLD}} + \frac{\Delta P \Delta t}{\Delta z} \tag{2.36}$$

The mass divergence of the updated velocities is calculated using Eq(2.28). Continual updates in cell pressure and velocities are made until |D| is less than the acceptable value (generally on the order of 10^{-6}). A flowchart for this process is given in Figure 2.2, which illustrates the iterative process for each time step.

Turbulent Solution Algorithm

The algorithm for the calculation of turbulent flow is almost identical to the procedure for laminar flow discussed in the previous section. The differences between the two methods are:

- Different equations are used for the calculation of the velocities.
- The explicit equations of Eq(2.21) and Eq(2.23) are solved at the same time as the explicit equations for the velocity components.
- Boundary conditions for the turbulent equations are added.
- The additional turbulent parameters must be determined (R_T, ν_t, etc.).

Because the iteration procedure on the velocity components is unchanged from the laminar scheme, the flowchart of Figure 2.2 may also be used to illustrate the algorithm for the solution of turbulent flow. The only changes would be those mentioned above.

Boundary Conditions

Perhaps the most important discussion pertaining to the numerical approximation of room air flow focuses on the boundary conditions which are imposed. In this section, the potential boundary conditions at each of the three boundaries are described. A table of these boundary conditions is also provided at the end of this section in Table 2.2.

Inlet

A uniform velocity distribution is generally assumed over the inlet area. Imposing this boundary condition allows the tangential velocity to be set equal to zero ($U_t=0$). The normal velocity component (U_n) is then determined based on the desired air flow rate (ACH) using the following equation.

$$U_{jet} = \frac{ACH \cdot Vol_{room}}{3600 \cdot A_{in}} \tag{2.37}$$

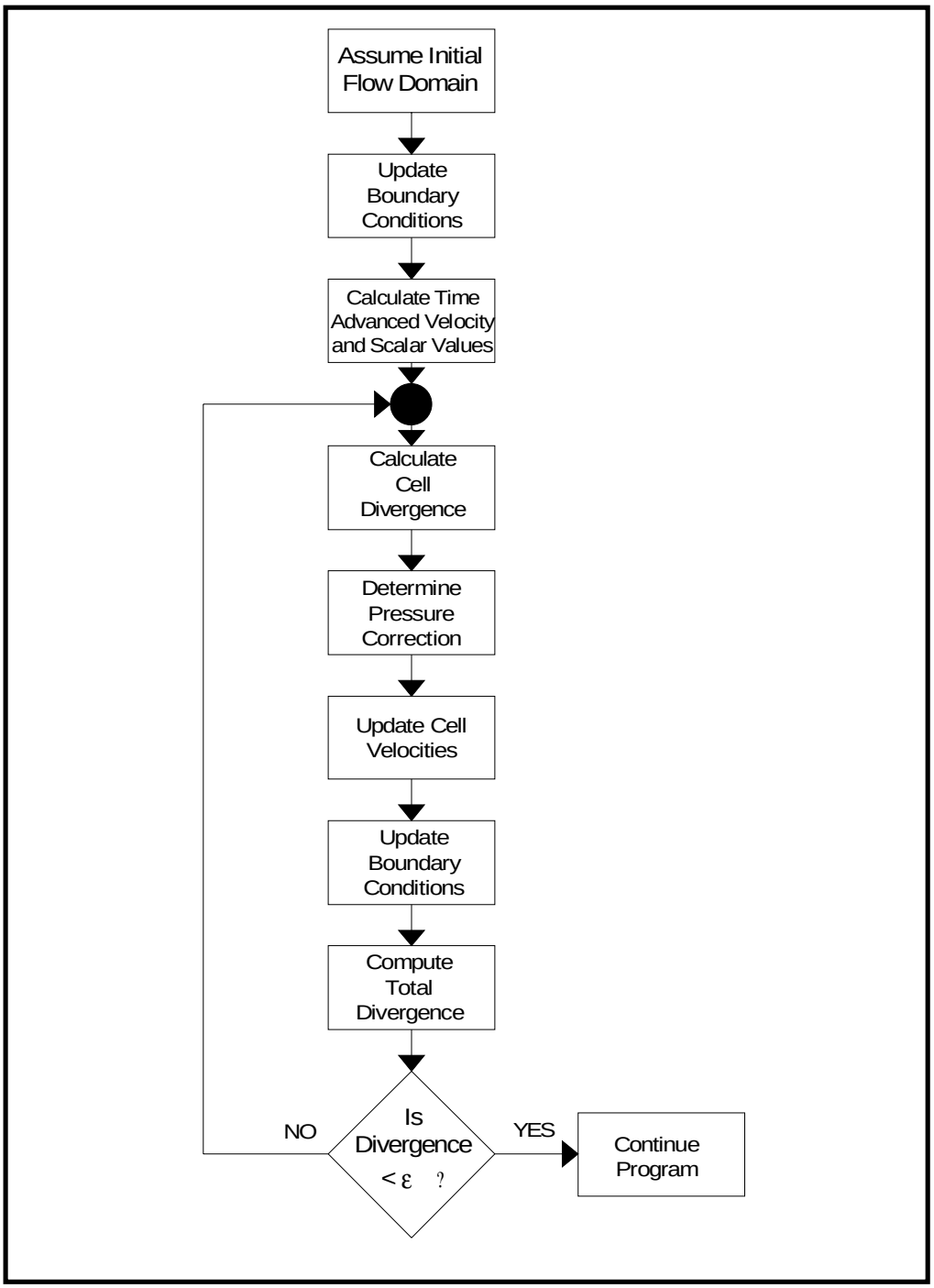

Figure 2.2. Solution Algorithm

The desired air flow rate of Eq(2.37) could be taken as the nominal value (15, 30, 50, or 100 ACH). Because volumetric flow values were measured during the experimental process, actual values may be used, rather than the nominal values. However, discrepancies between actual and nominal values may be considered negligible.

Because the flow is considered uniform, scalar quantities are considered constant over the room inlet. Therefore, the inlet temperature may be set as a simulation parameter. The kinetic energy and dissipation rate at the inlet may be determined from the following equations given by Awbi [1989].

$$k_{in} = \frac{3}{2} I_u^2 U_{jet}^2 \tag{2.38}$$

$$\varepsilon_{in} = \frac{k_{in}^{3/2}}{\lambda H} \tag{2.39}$$

where I_u^2 = turbulence intensity of the x-velocity
λ = constant (≈ 0.005)
H = room height or square root of inlet area (m)

The value of I_u^2 may be taken as 0.14 in the absence of any measured values. Different values of k_{in} and ε_{in} have been shown to have little effect on the results of simulations [Awbi, 1989].

Although convenient, the use of this uniform velocity profile boundary condition may be in direct contradiction with experimental evidence. Various factors, including a temperature difference between the room and supply air, may create velocity profiles at the entrance which are far from uniform.

Figure 2.3 on the following page shows the inlet velocity magnitude (airspeed) profiles for several flow rates based on the experimental results. These values were

measured at locations 12.7 cm (z/W=0.32) from the side wall and 18.0 cm (x/W=0.45) downstream from the inlet. In each case, horizontal lines are used to illustrate the approximate location of the inlet.

As shown by the figure, the uniform profile assumption loses validity as the air flow rates into the room decrease. In each case, there exists a relationship between the inlet velocity and the y-location at the inlet. Therefore, significant errors in the over-all simulation may be introduced through the assumption of an uniform velocity profile at the inlet.

In addition to the uniform profile boundary condition, simulations will also be performed using estimated inlet profiles which are based on the plots shown in Figure 2.3. Figure 2.4 shows alternative approximating functions superimposed with the experimental velocity profiles at the inlets. The equations for these functions are given in Table 2.1.

These alternative approximations consist of piecewise linear functions. The simplest of these new approximations is for 15 ACH. For this case, the inlet is approximated by reducing the area by one-half and doubling the inlet velocity to achieve the same volumetric air flow rate. More complex functions are used to model the profile for 50 and 100 ACH.

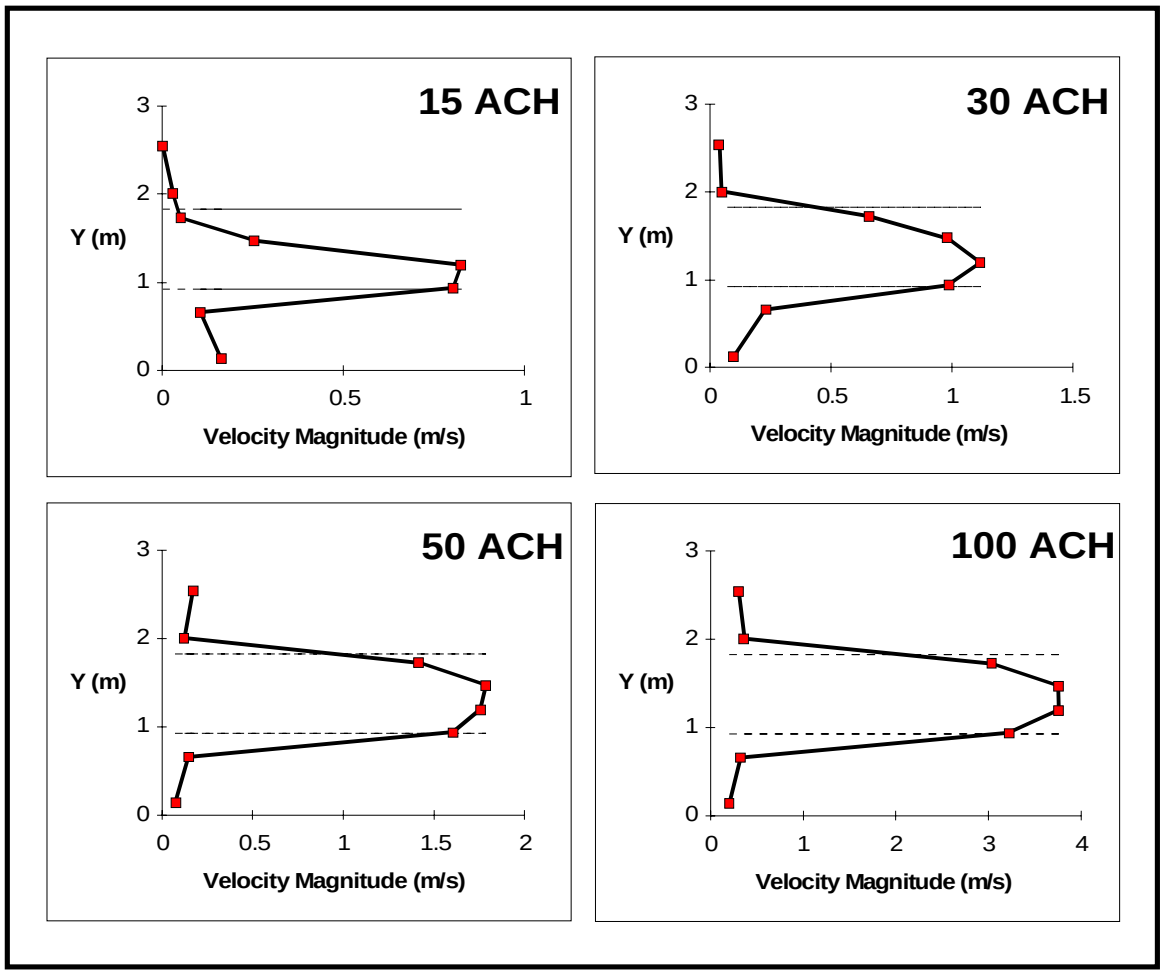

Figure 2.3. Experimental Inlet Velocity Profiles

As shown by the figure, these new profile approximations model the behavior of the inlet better than a uniform profile. However, the values of the new profiles are generally less than the experimental values. This occurs primarily because the inlet used to model the flow is slightly larger than the actual room inlet. More information on this is discussed later in the error analysis.

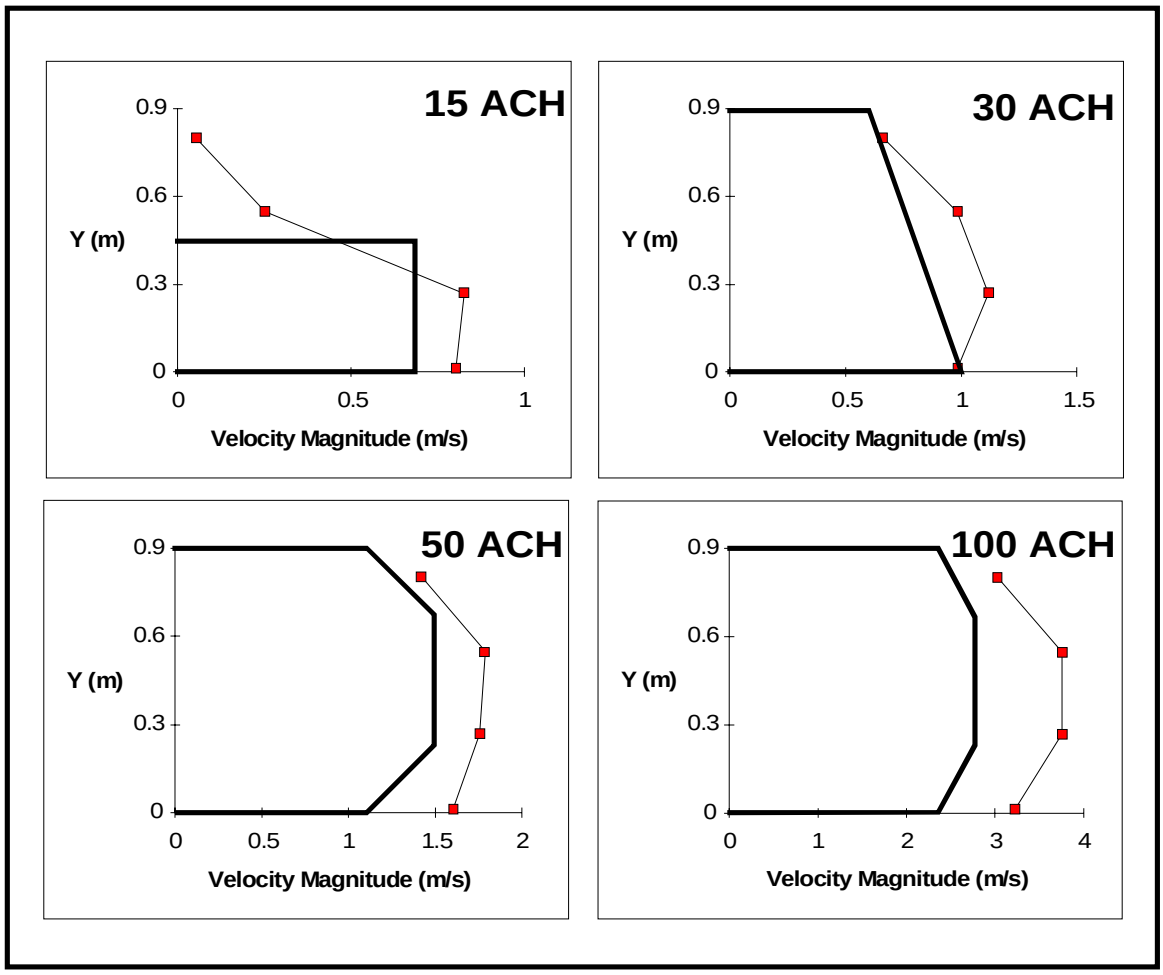

Figure 2.4. Approximation of Inlet Profiles

Using a non-uniform velocity profile at the inlet will obviously affect the profiles of the turbulent kinetic energy(k) and its rate of dissipation (ε). Therefore, equations Eq(2.38) and Eq(2.39) may be used in conjunction with the new velocity profiles to approximate the distribution of these variables at the inlet.

While the desired volumetric flow rate is maintained through the use of the approximated profiles, certain flow characteristics will inevitably be altered as well. These characteristics include the turbulent Reynolds number and momentum diffusion at

the inlet. Only through simulation can it be determined how the use of approximated profiles will affect the flow.

TABLE 2.1

INLET PROFILE APPROXIMATIONS

Flow Rate (ACH)	**Uniform Profile (m/s)**	**Profile Approximation (m/s)**
15	0.345	$0.690 \quad \left(0 < y < \frac{h}{2}\right)$ $0 \quad \left(\frac{h}{2} < y < h\right)$
30	0.690	$1.0 - \frac{0.4y}{h} \quad (0 < y < h)$
50	1.150	$1.1 + \frac{8y}{5h} \quad \left(0 < y < \frac{h}{4}\right)$ $1.5 \quad \left(\frac{h}{4} < y < \frac{3h}{4}\right)$ $2.7 - \frac{8y}{5h} \quad \left(\frac{3h}{4} < y < h\right)$
100	2.300	$2.35 + \frac{8y}{5h} \quad \left(0 < y < \frac{h}{4}\right)$ $2.75 \quad \left(\frac{h}{4} < y < \frac{3h}{4}\right)$ $3.95 - \frac{8y}{5h} \quad \left(\frac{3h}{4} < y < h\right)$

Outlet

Similar to the room inlet, a uniform velocity distribution may be assumed over the room outlet. Because there is no experimental data available on the outlet profile, this is the only feasible outlet boundary condition. Tangential velocities are considered zero (U_t=0) and the normal velocity is computed from a mass balance on the room as given by the following equation.

$$U_{out} = U_{jet} \frac{(\rho A)_{in}}{(\rho A)_{out}} \tag{2.40}$$

Because a constant density flow is assumed, Eq(2.40) simply allows the exit velocity to be determined by the ratio of the inlet area to the outlet area. The uniform distribution forces the gradients of all scalar properties to be zero at the exit. Therefore,

$$\frac{\partial k}{\partial x_n} = \frac{\partial \varepsilon}{\partial x_n} = \frac{\partial T}{\partial x_n} = 0 \tag{2.41}$$

Walls

While most researchers tend to agree on the inlet and outlet boundary conditions, there is significant discrepancy concerning the boundary conditions at the walls.

Because the walls are impermeable, the normal velocities (U_n) must be zero at the boundaries. The simplest way of imposing tangential velocity (U_t) values is to allow either free-slip or no-slip conditions. However, this conditions may only be imposed when the wall functions are not used in conjunction with the k-ε model. The imposition of a boundary condition based on Eq(1.19) is very difficult. Therefore, some researchers have simplified Eq(1.19), and have imposed the following boundary condition [Murakami, et al., 1989,1990].

$$\left.\frac{\partial U_t}{\partial x_n}\right|_{wall} = \frac{mU_t}{y_n} \tag{2.42}$$

where m = constant (1/7)
y_n = normal distance from the wall to the cell center (m)
U_t = tangential velocity component at y_n (m/s)

Regardless of whether wall functions or a low-Reynolds model is being used, boundary conditions for the turbulent energy may be fixed by the following equation.

$$\frac{\partial k}{\partial x_n} = 0 \tag{2.43}$$

If a low-Reynolds model is used, boundary conditions for ε may be imposed several ways, including any one of the following conditions.

[Lam and Bremhorst, 1981] $$\frac{\partial \varepsilon}{\partial x_n} = 0 \tag{2.44a}$$

[Lam and Bremhorst, 1981] $$\varepsilon = \nu \frac{\partial^2 k}{\partial x_n^2} \tag{2.44b}$$

[Chen, 1990] $$\varepsilon = \frac{2\nu k}{y_n^2} \tag{2.44c}$$

When wall functions are used, boundary conditions may be imposed using Eq(1.21) and Eq(1.22). However, successful results have been achieved by replacing the use of two different values of ε by one value obtained from the following equation [Murakami, et al., 1989].

$$\varepsilon = \frac{(C_\mu^{1/2} k)^{3/2}}{\kappa y_n} \tag{2.45}$$

where C_μ = constant (0.09)
κ = von Karman constant (0.4)

In addition to velocities and turbulent parameters, boundary conditions for the heat transport equation must be imposed at the walls. The simplest boundary condition involves assuming that there is no temperature gradient at the wall boundaries ($\partial T/\partial x_n=0$). This boundary condition implies no heat transfer at the walls. If an adiabatic condition actually existed, the steady-state temperature distribution would approach the inlet temperature.

Figure 2.5 shows the illustration of a typical wall boundary, both physically and numerically. The numerical representation replaces the physical wall by fictitious cells which are used to impose the various boundary conditions.

The heat flux at the wall ($x_n=\Delta x_n$) due to convection is

$$\dot{q}'' = h(T_I - T_W) \tag{2.46}$$

As shown by the figure, temperatures are defined at cell centers. However, the heat flux at the boundary ($x_n=\Delta x_n$) must be maintained, and may be defined by Eq(2.47).

$$\dot{q}'' = - \left. k\frac{\partial T}{\partial x}\right|_{x_n=\Delta x_n} \tag{2.47}$$

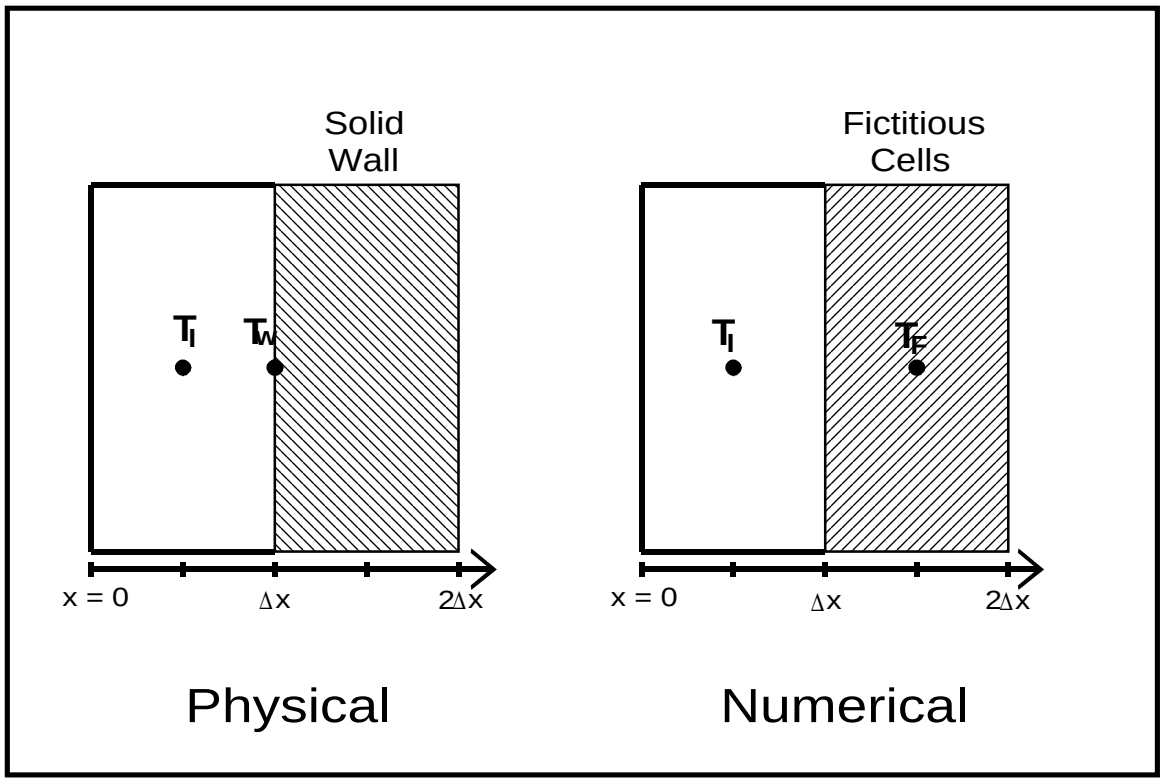

Figure 2.5. Wall Boundary

Using a forward-difference representation of the derivative, Eq(2.47) may be set equal to the convective heat flux of Eq(2.46) to solve for the necessary value of T_F which must be imposed. The resulting expression is given in Eq(2.48).

$$T_F = (1 - Nu_{\Delta x_n})T_I + (Nu_{\Delta x_n})T_W \tag{2.48}$$

where

$$Nu_{\Delta x_n} = \frac{h\Delta x_n}{k} \tag{2.49}$$

Tabulated values for the film coefficient (h) may be used. However, because values were determined during the experimental process, actual values should be used to better model the flow.

TABLE 2.2

BOUNDARY CONDITIONS

Boundary	**Velocities**	**Temperature**	**Turbulence Energy**	**Turbulence Dissipation**
INLET	$U_t=0$ $U_n=U_{jet}$	T_{in}	$k_{in}=\frac{3}{2}I_u^2U_{jet}^2$	$\varepsilon_{in}=\frac{k_{in}^{3/2}}{\lambda H}$
OUTLET	$U_t=0$ $U_n=U_{jet}\frac{A_{in}}{A_{out}}$	$\frac{\partial T}{\partial x_n}=0$	$\frac{\partial k}{\partial x_n}=0$	$\frac{\partial \varepsilon}{\partial x_n}=0$
WALLS *No Slip*	$U_n=0$ $U_t=0$			
WALLS *Free Slip*	$U_n=0$ $\frac{\partial U_t}{\partial x_n}=0$			
WALLS *low -Reynolds* [Chen, 1990]		$\frac{\partial T}{\partial x_n}=$ $\frac{h}{k}(T-T_w)$	$\frac{\partial k}{\partial x_n}=0$	$\varepsilon=\frac{2\nu k}{y_n^2}$
Walls *wall functions* [Murakami, et al.,1989]	$U_n=0$ $\left.\frac{\partial U_t}{\partial x_n}\right\|_w=\frac{mU_t}{y_n}$			$\varepsilon=\frac{(C_\mu^{1/2}k)^{3/2}}{\kappa y_n}$

CHAPTER III

ERROR ANALYSIS

When attempting to correlate or compare experimental results with numerical simulations, it is imperative that the issues of errors and uncertainties be addressed. In this chapter, the various sources for errors and uncertainties in both the experimental and numerical procedures for this project are identified. For simplicity, these discussions are presented on three levels, which represent how the errors and uncertainties may be classified. These levels are experimental, numerical, and analytical, as shown below in Table 3.1.

TABLE 3.1

CLASSIFICATION OF PROJECT ERRORS AND UNCERTAINTIES

Error	**Description**
Experimental	Errors introduced during the experimental investigation. (measurement uncertainties, etc.)
Numerical	Errors introduced during the numerical simulation. (finite-difference representations, grid size, etc.)
Analytical	Errors introduced during the analysis and comparison of the experimental data.

Experimental Errors

An in-depth analysis and discussion of the errors and uncertainties involved in the measurement of the air flow within the room has already been performed by Spitler [1990]. The results of this analysis may be summarized by Table 3.2, which contains the uncertainties which are important to this project.

TABLE 3.2

EXPERIMENTAL UNCERTAINTIES

Measurement	**Uncertainty**
Inlet Temperature	± 0.5 ºC
Outlet Temperature	± 0.6 ºC
Volumetric Flow Rate	± 2 %
Airspeed	+12/-23 % +10/-14 fpm (+12/-23 % +0.05/-0.07 m/s)

The temperature uncertainties were based on the individual measurement uncertainties as well as a statistical analysis of a sample of temperature measurements. The uncertainty in the volumetric flow rate was determined by errors in the flow and fan configuration, as well as errors in manometer readings. The sources of error which comprised the airspeed uncertainty were determined to be the perturbation error, sensor orientation, and the sensor accuracy. A very conservative estimate of ±10% was given to the perturbation error and great care was taken to reduce errors due to sensor orientation.

Therefore, actual experimental errors in airspeed measurements were probably less than the value indicated in Table 3.2.

Numerical Errors

The errors introduced during the numerical simulation are discussed in this section. The following list contains those areas of the numerical simulation which may possibly influence the propagation of errors of the project.

- Finite-difference approximations
- Grid size
- Grid coverage
- Boundary conditions

Finite-Difference Approximation Errors

Because numerical solutions consist of approximate solutions of unsolvable partial differential equations, errors are introduced in the approximation of the derivative terms. First and second derivative terms are approximated through the use of a Taylor series expansion. Therefore,

$$\frac{\partial \phi}{\partial x} = \frac{\phi_{i+1} - \phi_i}{\Delta x} + E(\Delta x) \tag{3.1}$$

$$\frac{\partial^2 \phi}{\partial x^2} = \frac{\phi_{i-1} - 2\phi_i + \phi_{i+1}}{(\Delta x)^2} + E(\Delta x^2) \tag{3.2}$$

While Eq(3.1) displays the first derivative via the forward difference method, a similar expression may be used for the backward difference method. The terms $E(\Delta x)$ and $E(\Delta x^2)$ represent the errors associated with each approximation. Thus, first and second-order accuracy is obtained for the first and second derivatives, respectively.

Grid Size

As shown by the error terms of Eq(3.1) and Eq(3.2), the resolution of the grid is a strong factor in the magnitude of the overall simulation error. Clearly, as the cell dimensions are reduced, the terms more closely approximate a true derivative and the error is reduced. Time and computational constraints, however, limit the resolution of the computational mesh.

As increasingly finer grids are used, computed values will begin to show less sensitivity to the grid size. At some point in this process, it will become apparent that noticeable increases in accuracy are no longer obtained, and the feasibility limit on the grid resolution has been reached.

Grid Coverage

Errors introduced by grid coverage are associated with the question "How well does the computational mesh cover the physical domain?" In the case of this project's simulations, some approximations were made. These approximations were made to allow the use of a uniform mesh, evenly spaced in all three directions ($\Delta x=\Delta y=\Delta z$).

As shown in Figure 1.1, the physical dimensions of the experimental room were 15 x 9 x 9 ft (4.57 x 2.74 x 2.74 m). However, the air flow was simulated using a room of size 4.5 x 2.75 x 2.75 m. Therefore, each dimension of the numerically simulated room differs by approximately 1%, excluding any uncertainties in measurements of the experimental room.

The physical dimensions of the inlet and outlet are 15.75 x 35.58 in (0.4 x 0.9 m). The inlet and outlet were modelled, however, by assigning width and height dimensions which were 1/6 and 1/3 the dimension of the room height. Thus, the dimensions were 0.458 x 0.916 m. The resulting error is +14% for the width and +2% for the height.

Thus, the inlet area is being modelled by an area which is approximately 16.5% larger than the actual experimental area. Because simulations are performed and compared on the basis of the volumetric flow rate, the normal components of velocity at the inlet for the modelled room will be slightly less than the experimental room, depending upon what type of velocity profile is being used.

Boundary Conditions

As discussed in the end of the previous chapter, the numerical solution may assume a uniform velocity distribution at the inlet, which was shown to quite questionable. Even the approximated forms of the velocity profiles may not match the experimental results well enough to prevent discrepancies between the experimental and numerical data. This discrepancy in the velocity profiles will not only affect the velocity distribution near the jets, but will also affect the nature of the turbulent kinetic energy and dissipation distributions as well.

In addition to the velocity distribution at the inlet, there may exist pressure gradients at the inlet and exit ignored during the numerical simulation which would cause discrepancies between numerical and experimental results.

Analytical Errors

Two significant sources exist for errors which may be introduced during the analysis and comparison of the experimental data. The first involves the determination of velocity magnitudes. Because the experimental data consists of airspeeds, the individual components of velocity determined during the numerical simulations, must be resolved into a single magnitude of velocity. The difficulty arises because velocities are defined using the Marker-and-cell formulation on the faces of the cells, rather than at the cell center (see Figure 2.1). Since each of the three velocity components is defined at

different locations, some method of approximation must be used in determining the velocity components at the center of the cell. This problem may be solved by assuming that a component of velocity varies linearly within the cell, so that the following approximations may be made at the cell center.

$$U_{x,y,z} = \frac{1}{2}(U_{i,j,k} + U_{i-1,j,k}) \tag{3.4}$$

$$V_{x,y,z} = \frac{1}{2}(V_{i,j,k} + V_{i,j-1,k}) \tag{3.5}$$

$$W_{x,y,z} = \frac{1}{2}(W_{i,j,k} + W_{i,j,k-1}) \tag{3.6}$$

$$|\mathbf{V}|_{x,y,z} = \left[U^2_{x,y,z} + V^2_{x,y,z} + W^2_{x,y,z}\right]^{1/2} \tag{3.7}$$

By using the above equations, velocity magnitudes may be determined from the numerical results for (x,y,z) coordinates. However, the second source of error arises if numerical results are not available for the same coordinates at which data was collected during the experimental investigation. An interpolation scheme must be used to obtain approximate results of the numerical simulations at each of the experimental coordinates. While several methods of interpolating data exists, this project uses a linear interpolation scheme to approximate values which fall within a volume bounded by eight numerically determined values.

In addition to these potential errors, an additional issue must be addressed which is more of a strong concern than an error. In Chapter 4, contour plots are presented for the velocity magnitudes. These plots were created by the statistical package Systat™. Using discrete data points from the experimental and numeric investigations, the software

uses a quadratic interpolation scheme to approximate values within the room. While it would appear that values between data points are sufficiently estimated, there is a tendency to generate "artifacts" while extrapolating values near the wall. These artifacts generally appear as unusually high values. The distances between the walls and the nearest data points range between 12 to 40 cm. Therefore, one must be careful when interpreting the plots, particularly when looking at phenomena near the boundaries.

CHAPTER IV

RESULTS & DISCUSSION

Overview of Simulations

Although the previous experimental research has provided a significant amount of data, only four of the experimental tests (15, 30, 50, and 100 ACH) were investigated. Only the side wall inlet configuration of Table 1.4 was used. The other configurations and experimental tests have been saved for continuation studies. In addition to the flow rates, other parameters were varied during the investigation process. These parameters in included inlet boundary conditions, wall boundary conditions, and the two forms of the k-ε model. A summary of these parameters is given in Table 4.1

TABLE 4.1

INVESTIGATION PARAMETERS

Parameter	**Variations**
Flow Rate	15, 30, 50, and 100 ACH
Flow Type	Laminar, Turbulent with wall functions, and low-Reynolds turbulent models
Wall Boundary Conditions	Free-slip and No-slip
Inlet Profiles	Uniform and Approximated

As described by Table 4.1, a total of 48 different combinations of investigation parameters were simulated. However, significantly more simulations were performed, as up to five different grid resolutions were used. These grid resolutions are given in Table 4.2, below.

TABLE 4.2

GRID RESOLUTIONS

Name	Abbreviation	X Cells	Y Cells	Z Cells	Cell Size (m)
Very Coarse	VC	10	6	6	0.458
Coarse	C	20	12	12	0.229
Fine	F	30	18	18	0.153
Very Fine	VF	40	24	24	0.115
Ultra Fine	UF	46	30	30	0.092

Table 4.3 details the various properties of air and other numerical parameters used during all simulations. It is important to note that the density value used is a "base density." The temperature differences within the room will obviously create density differences throughout the room, which are the cause of buoyant effects. However, because the maximum temperature difference is only 9 ^{o}C, flow may be approximated through the use of a single value of the density.

TABLE 4.3

FLOW PARAMETERS

Parameter		Value
Density	(ρ)	1.19 kg/m^3
Kinematic Viscosity	(ν)	1.56×10^{-5} $\frac{m^2}{s}$
Thermal Conductivity	(k)	0.026 $\frac{W}{m \cdot {}^oK}$
Specific Heat	(C_p)	1003.6 $\frac{J}{kg \cdot {}^oK}$
Thermal Expansion Coefficient	(β)	3.47×10^{-3} $\frac{1}{{}^oK}$
Inlet Temperature	(T_{in})	21 ^oC
Initial Temperature	(T_{init})	30 ^oC
Wall Temperature	(T_w)	30 ^oC

Visualization of three-dimensional CFD results is a difficult problem. One way of presenting data graphically is to show "slices" of the flow, in which one of the (x,y,z) coordinates is held constant. Contours of constant values may then be made, showing the distribution of velocity magnitudes on that plane in the room. To provide plots for several planes for each of the simulations would tend to be confusing. Therefore, unless explicitly noted otherwise, all graphical results will be plotted on one of the two planes shown in Figure 4.1.

Because the numerical simulations provide values for the individual velocity components, it is possible to plot results using arrows representing the direction as well as the relative magnitude of each of the velocity vectors. However, data was chosen not to be presented in this manner when performing comparisons to experimental data since the experimental data consists only of air speeds, without any resolution into velocity

components. Because vector plots would provide informative insight into the room air flow pattern, velocity vector plots, with discussions, are presented later, at the end of this chapter.

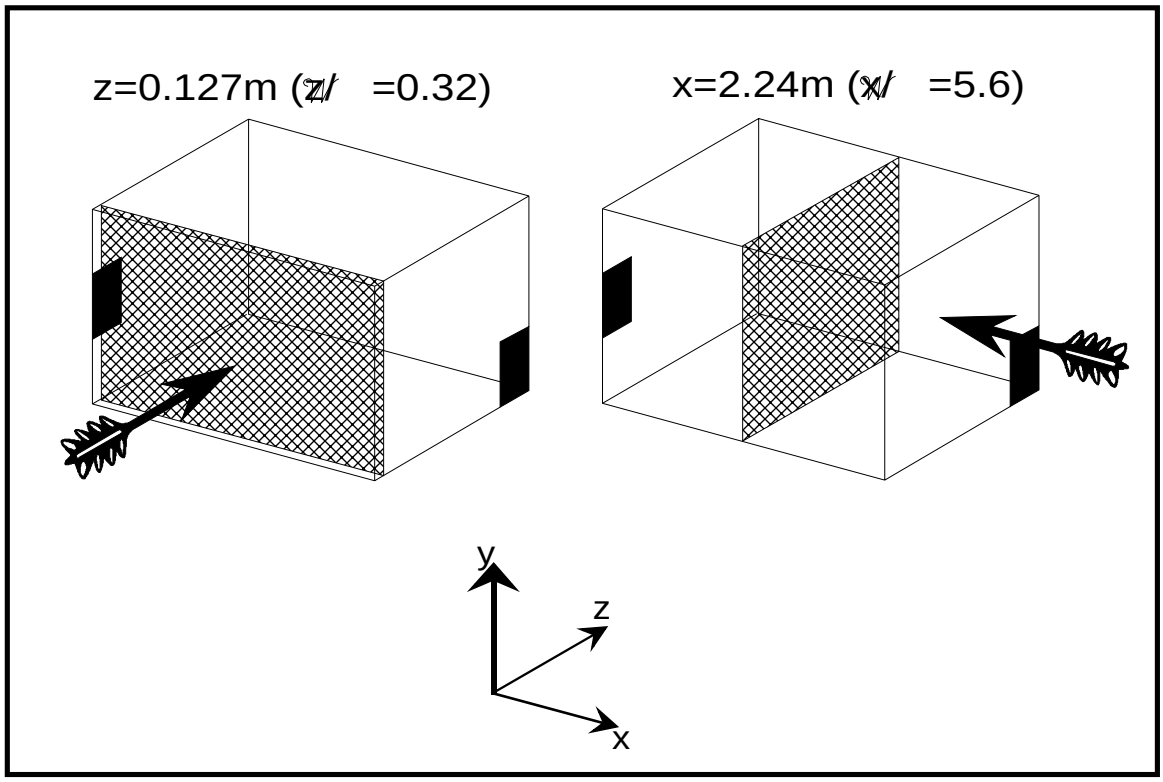

Figure 4.1. Description of Plot Views

Grid Size

As shown in Table 4.2, five different grid sizes were investigated. Rather than attempt to display results for all grid resolutions, this section attempts to determine the

optimum grid size for all subsequent plots. To compare grid sizes, the simple case of 100 ACH was used and results were compared at two different constant (x,z) lines. Both lines were located 0.127 m (z/W=0.32) from the side wall. One line was located 0.470 m (x/W=1.18), while the second was located 2.24 m (x/W=5.6) downstream of the inlet. Figure 4.2 illustrates the location of these lines, as "dots" are used to show the location of the discrete points along the lines.

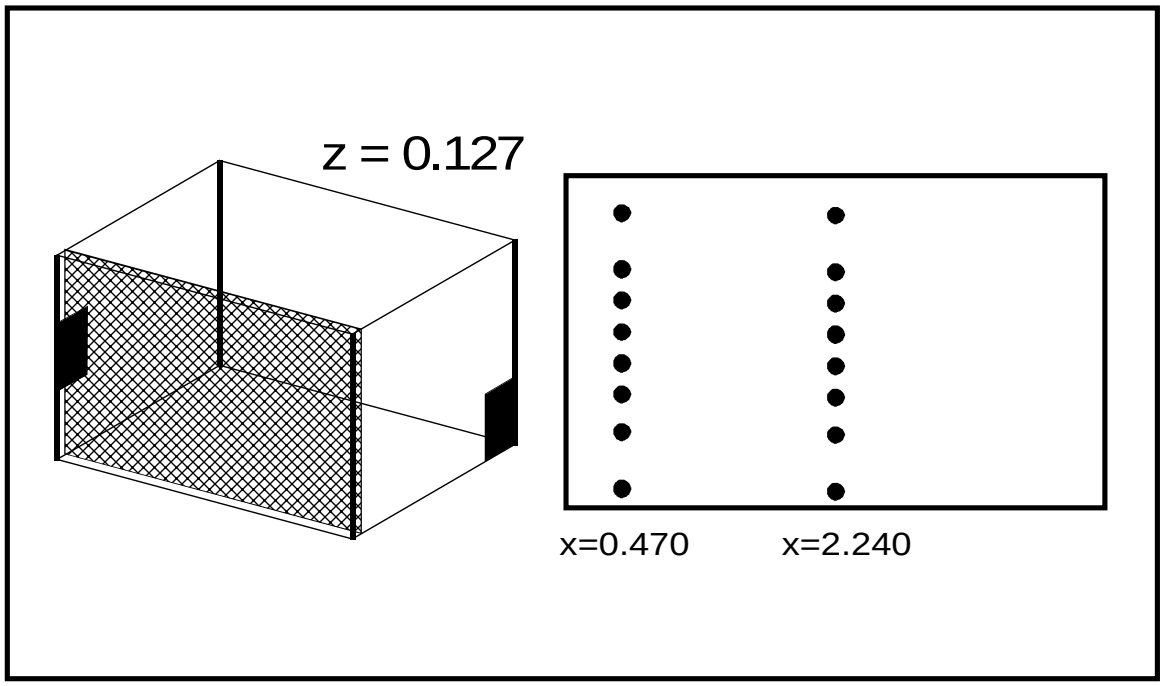

Figure 4.2. Location of Grid Comparisons

Figure 4.3 on the following page displays the velocity magnitude results for these locations using the five grid resolutions of Table 4.2.

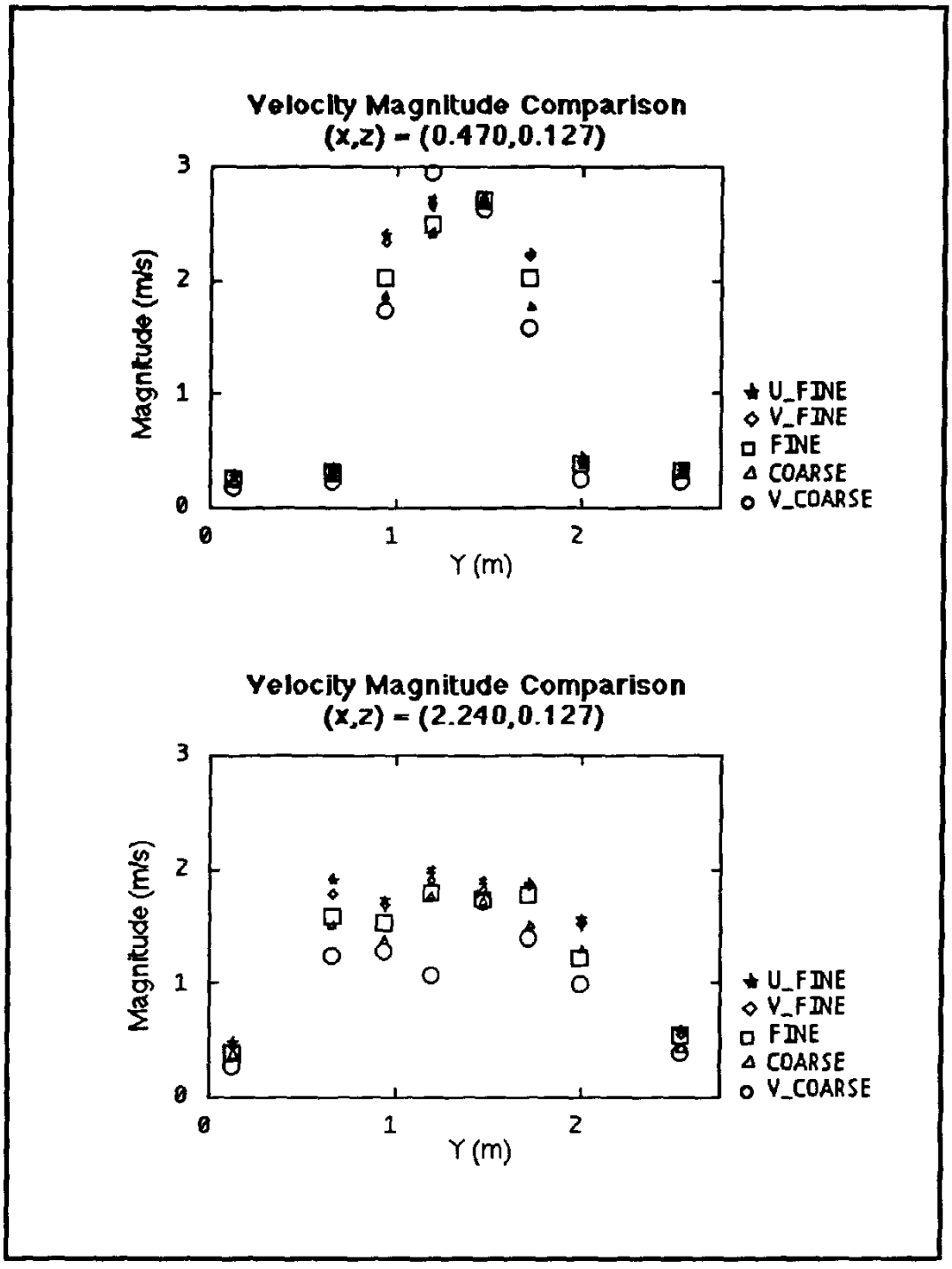

Figure 4.3. Grid Size Comparison

An inspection of the data in Figure 4.3 illustrates that the velocity magnitudes for each location seem to "converge" on a value as the grid size decreases. While one would expect this convergent process to continue for even finer meshes than the five investigated, for the purpose of this project the Very Fine mesh appears to provide sufficient accuracy. The sufficiency of a "grid-independent solution" is emphasized when the necessary computational time is considered. Therefore, all subsequent results in the report will be presented for the Very Fine (40x24x24) mesh.

In addition to the comparison of velocity magnitudes, the grid resolutions were compared on the basis of computational time. Figure 4.4 shows the computational time required by each grid size for the same simulation as Figure 4.3, using an IBM RISC-6000 computer.

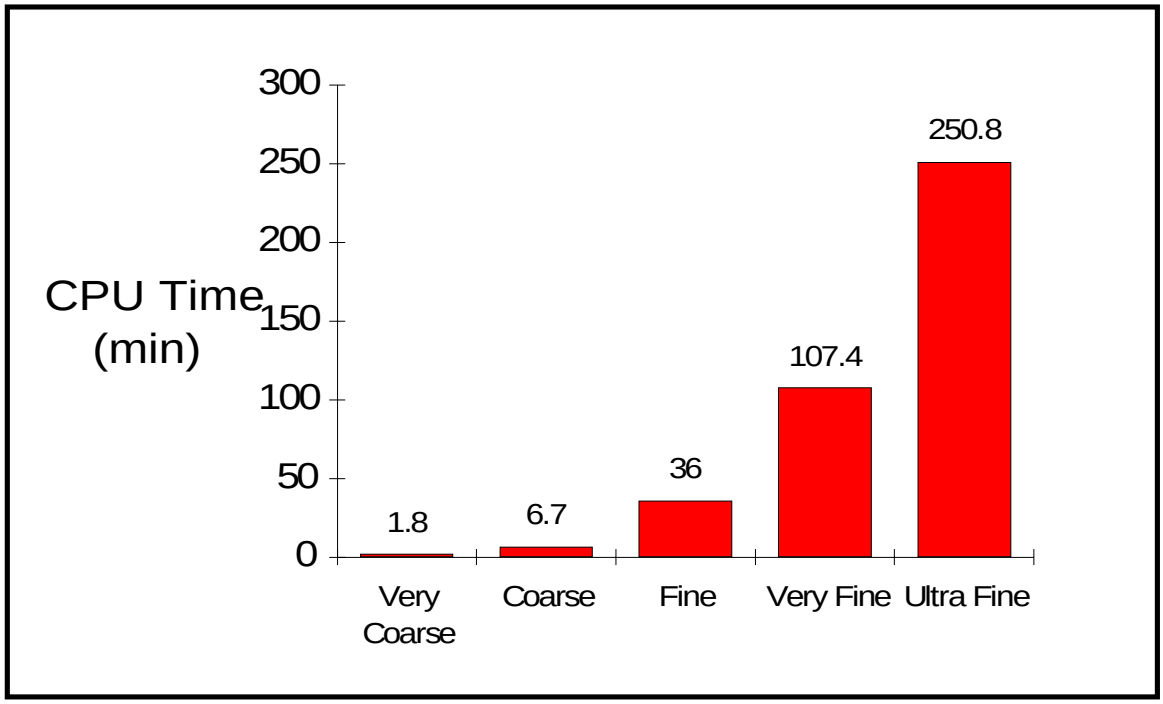

Figure 4.4. Computational Time for Grid Sizes

Inlet Profiles

Chapter 2 described how the common assumption of a uniform inlet velocity profile could be replaced by some form of an approximated velocity profile. This section briefly illustrates the advantage of an approximated profile over a uniform profile.

As shown by Figure 2.4, the most dramatic case of a non-uniform profile occurs at the lowest flow rate, 15 ACH. Therefore, this flow rate will be used to compare the uniform profile with the approximated profile.

Figure 4.5 shows plots of the velocity magnitudes for the uniform and the experimental profile in the region immediately near the inlet. Two primary characteristics are displayed which serve to show the inadequacy of the approximation. First, the velocity magnitude values for the uniform inlet are considerably less than the experimentally measured values. Second, the uniform profile approximation generates a jet which is larger in cross-sectional area than the experimental jet. The increase in jet size is expected, as the uniform profile assumes an inlet jet occupying the entire cross-sectional area of the inlet. As shown earlier in Figure 2.4 and now in Figure 4.5, the experimental profile appears to only occupy the lower half of the inlet area.

Figure 4.6 shows the effect of reducing the inlet area. As shown by the figure, reducing the inlet area not only results in increased velocity magnitudes, but also produces a jet which matches better in size with the experimental profile. Thus, a simple comparison of Figures 4.5 and 4.6 emphasizes how a uniform inlet assumption is very inconsistent with the experimental data.

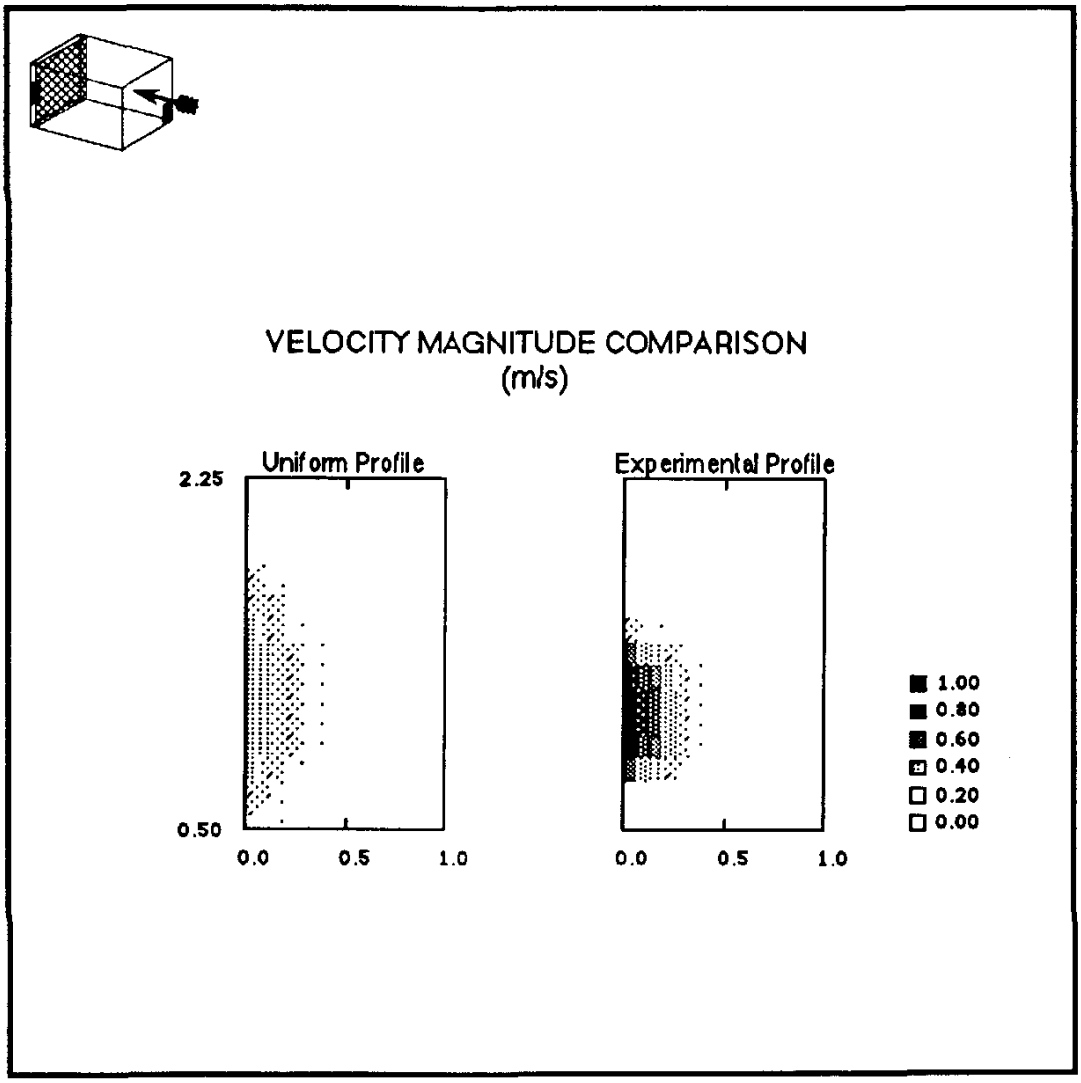

Figure 4.5. Velocity Magnitude Distribution Using Uniform Inlet Profile (15 ACH)

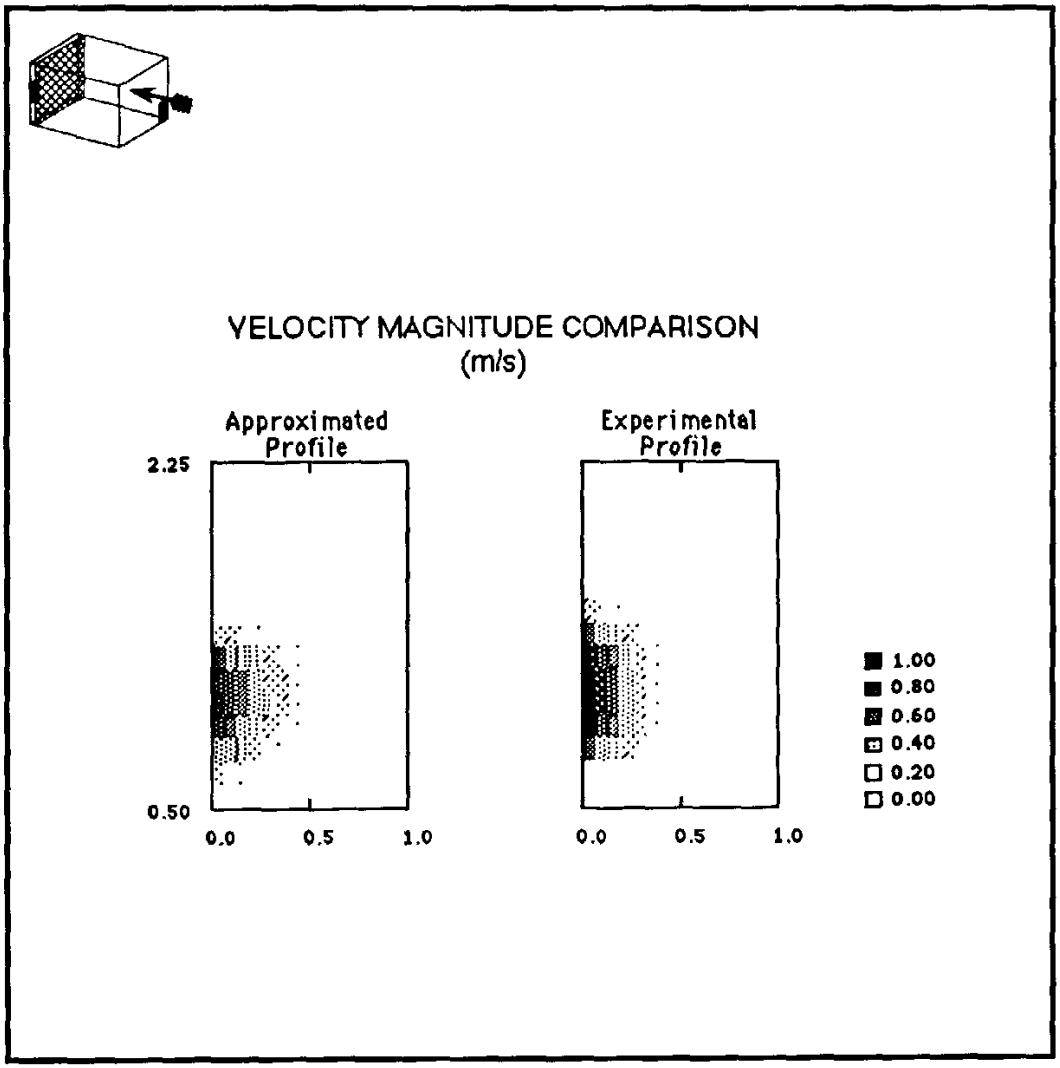

Figure 4.6. Velocity Magnitude Distribution Using an Approximated Inlet Profile (15 ACH)

While Figures 4.5 and 4.6 certainly highlight the need for some form of an assumed profile, even more convincing evidence may be obtained by viewing the inlet jets from the side. Figure 4.7 on the following page shows the entering jets for the

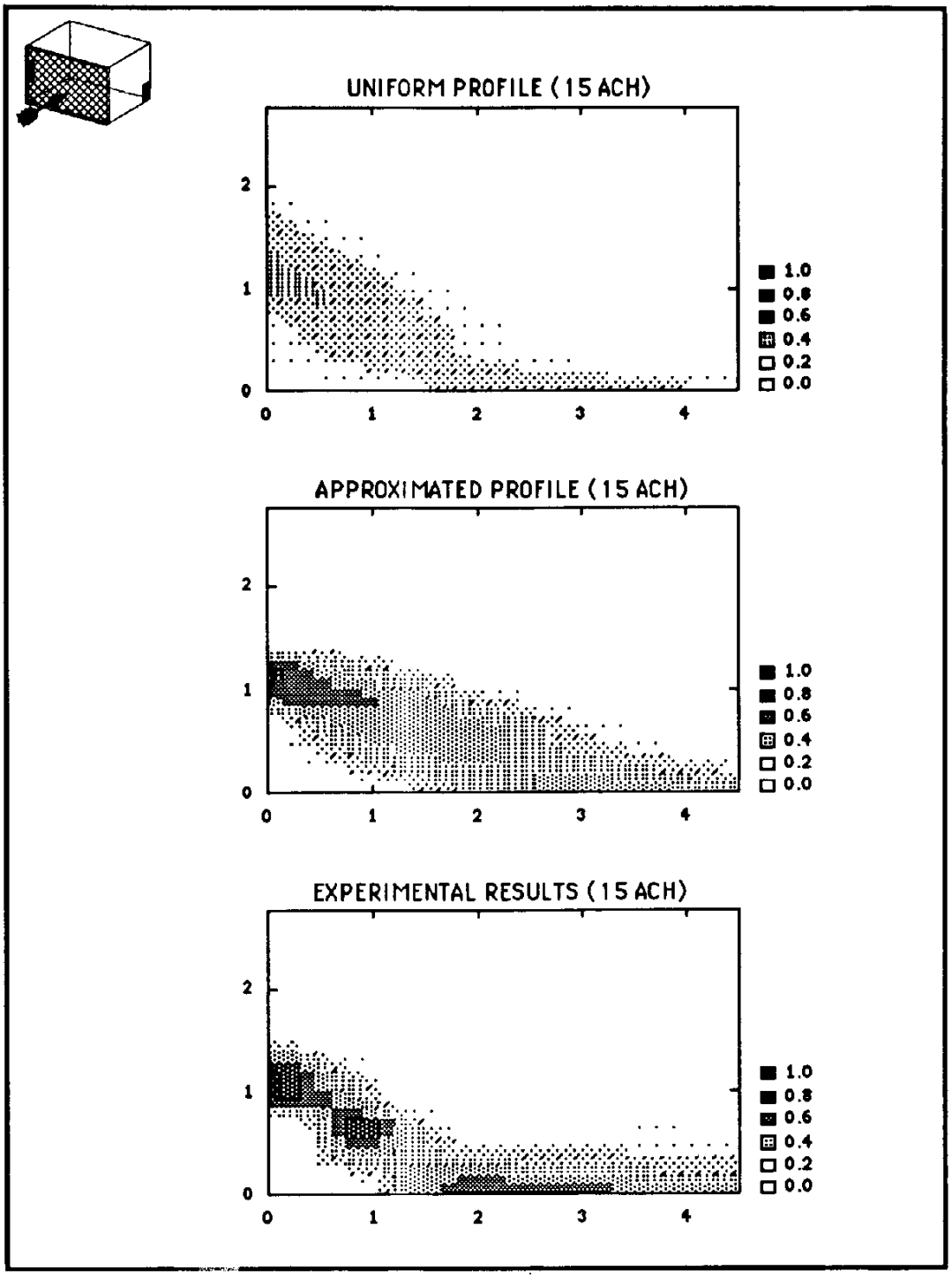

Figure 4.7. Comparison of Inlet Jets Using Uniform and Approximated Inlet Jets (15 ACH)

conditions of Figure 4.5 and 4.6. In addition, a plot of the experimental results is included for comparison.

A simple analysis of Figures 4.5 - 4.7 shows that the simulation error is decreased when the approximated inlet profile is used. Thus, discrepancies to experimental data are reduced in the region near the inlet, and should also be reduced "downstream" of the inlet jet.

The graphical comparison of the uniform and assumed profiles results sufficiently proves that the uniform velocity profile is somewhat inconsistent with experimental data. Because the use of approximated profiles at the inlet seems to provide more comparable results, all flow plots shown will be the result of simulations using the approximated profiles.

Wall Boundary Conditions

While normal velocities are certainly easy to describe at walls, tangential velocity boundary conditions may be imposed any one of several ways. When using the k-ε model with wall functions, the "power law" boundary condition must be used because the basis of the model is the imposition of the log profile at the wall. The laminar and low-Reynolds models do not necessarily require the same boundary condition. Therefore, free-slip and no-slip conditions were investigated to determine which, if either, of the conditions provided results more consistent with the experimental data.

Although slight differences in the results were noted at 50 and 100 ACH, significant differences were noted at the lower flow rates. The most drastic of these differences can be seen in Figure 4.8 on the following page, in which plots of 15 ACH for free-slip and no-slip simulations are presented in addition to the experimental results.

As shown by Figure 4.8, the imposition of no-slip conditions at the wall provide velocity magnitudes which are noticeably smaller than both the free-slip and

experimental results. Similar results, though less dramatic, were obtained for 30, 50, and 100 ACH. Therefore, the resulting plots in the following section were obtained using free-slip conditions at the walls for tangential velocities for the laminar and low-Reynolds models.

The use of free-slip conditions does not imply that slippage physically occurs at the wall. It merely means that from a computational stand-point, free-slip conditions better approximate the actual flow.

Buoyancy

Because simulations are performed for a jet entering a room with a temperature difference of 9 ^{o}C, it is expected that buoyant effects should be considered. Because the maximum external force on a control volume due to buoyancy is dependent only on the temperature difference and not the velocity, there may be cases in which the buoyant forces are negligible compared to the other forces. If these cases do exist, computational time could be reduced since the solution of the energy equation would not be required.

Simulations were performed for each of the four flow rates, ignoring buoyancy. The most dramatic differences, as expected, were produced when simulating 15 ACH. Figure 4.9 shows the result for this set of simulations.

Similar, though less drastic, results were obtained for 30 and 50 ACH. Only in the case of 100 ACH were the differences negligible. Therefore, all presentation of simulation results will be for simulations performed using the Boussinesq approximation for buoyancy.

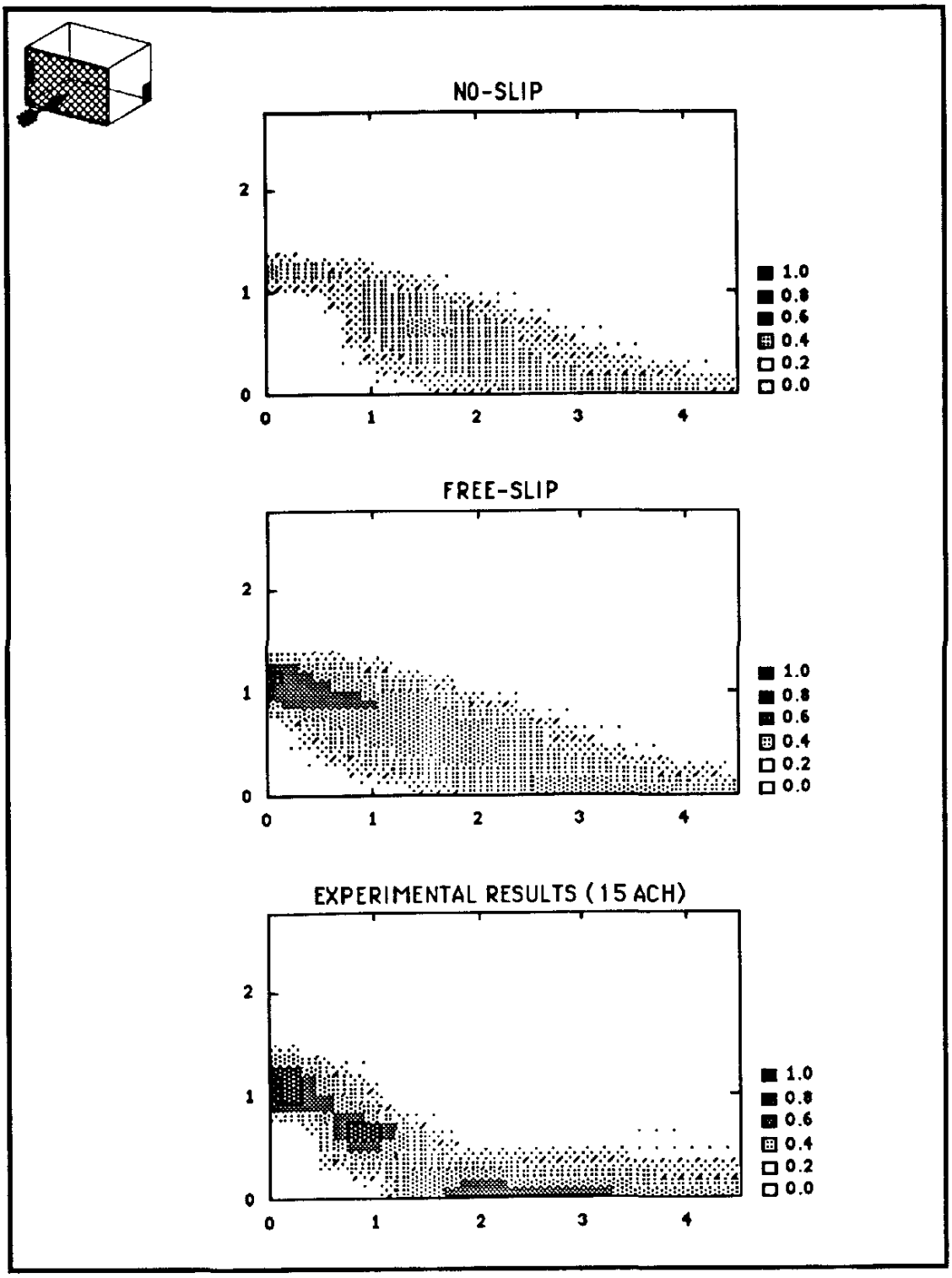

Figure 4.8. Comparison of Inlet Jets Using No-Slip and Free-Slip Conditions

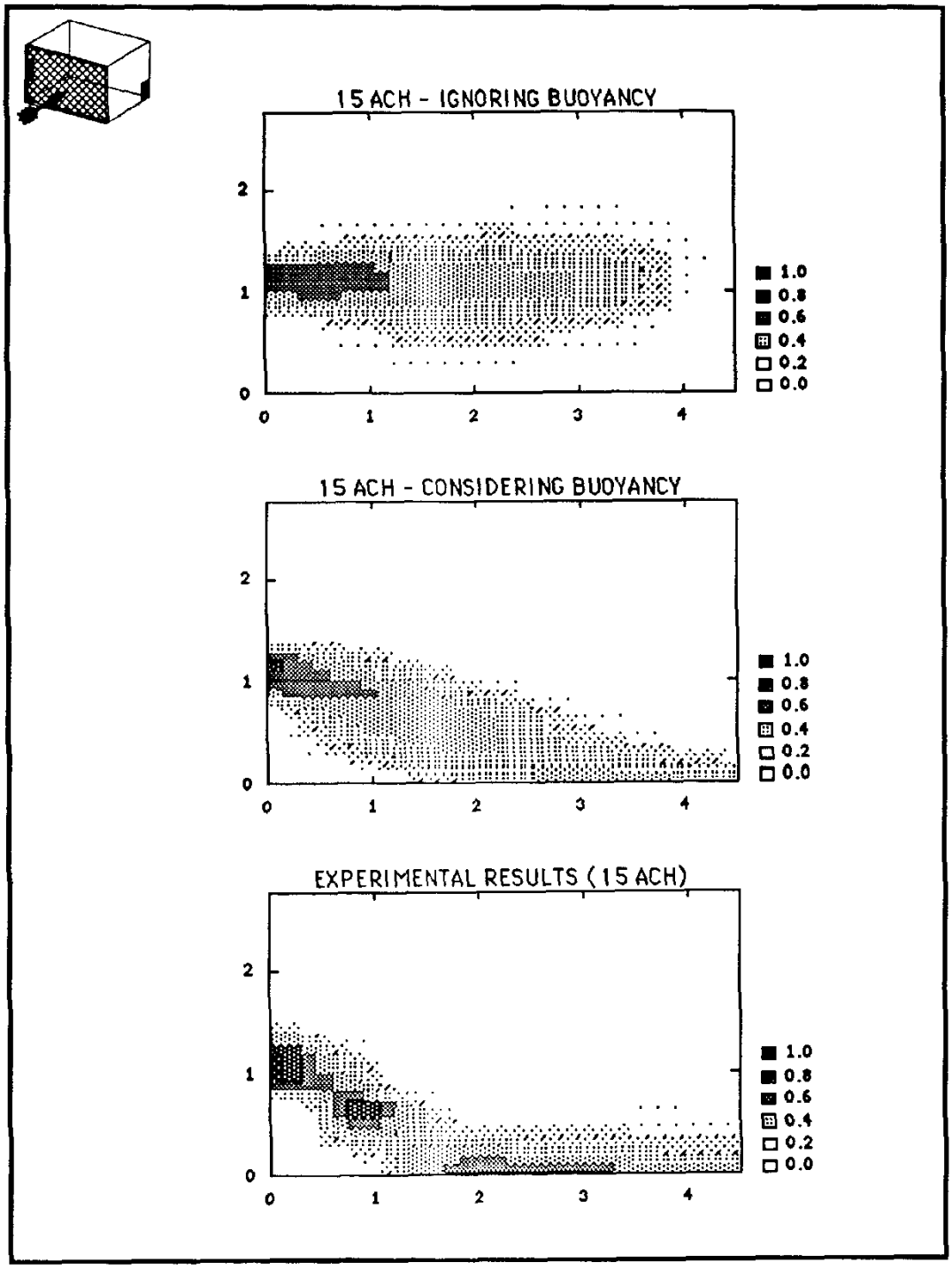

Figure 4.9. Simulation Comparisons With and Without the Consideration of Buoyancy

Simulation Results

The following pages contain the results of the simulations for 15, 30, 50, and 100 ACH, using the boundary conditions and grid size discussed earlier in this chapter.

Each page contains four plots, all of the same plane within the room. Laminar, turbulent/wall functions, and turbulent/low-Reynolds solutions are represented. The experimental results are included as the fourth plot to allow for easier comparison.

Although units are not shown in the plots, all velocity magnitude contours are given in 'meters per second' and axis labels are shown in 'meters'.

For convenience, the plots of each of the flow rates are presented in the two pages following the discussion page for the corresponding flow rate.

15 ACH

As shown by Figure 4.10, all three methods predicted the basic pattern of the flow. However, none of the methods sufficiently predicted the strong buoyant effect of the flow immediately upon entering the room. The low-Reynolds model appears to better approximate the inlet jet, although all the models appeared to have generated magnitudes which are slightly less than the experimental results. One possible reason for this may be found in Figure 4.11, which represents a lateral view from the center of the room. All three models predicted far more lateral diffusion, which would certainly help explain the reduced values in Figure 4.10. Despite variations in boundary conditions, this over-prediction of lateral diffusion still continued.

These figures also illustrate the extrapolation concern discussed in the previous chapter. As shown at the bottom of the experimental results in Figure 4.10, unusually high velocity magnitudes were extrapolated. Additionally, values are shown in the upper left corner of the experimental and laminar plots of Figure 4.11 which appear to be unrealistic with respect to the main pattern of the flow.

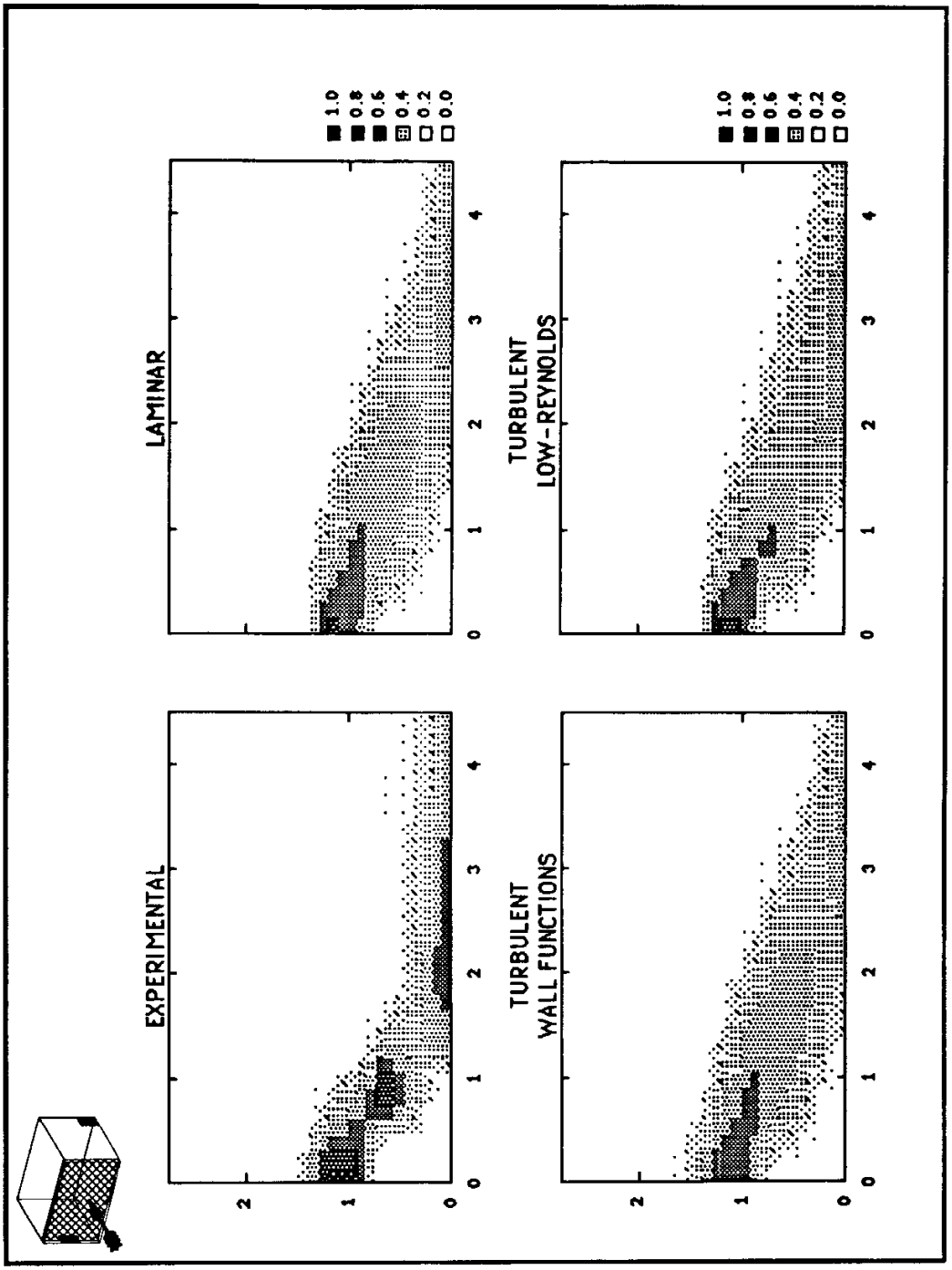

Figure 4.10. Simulation Results for 15 ACH (z=0.127 m)

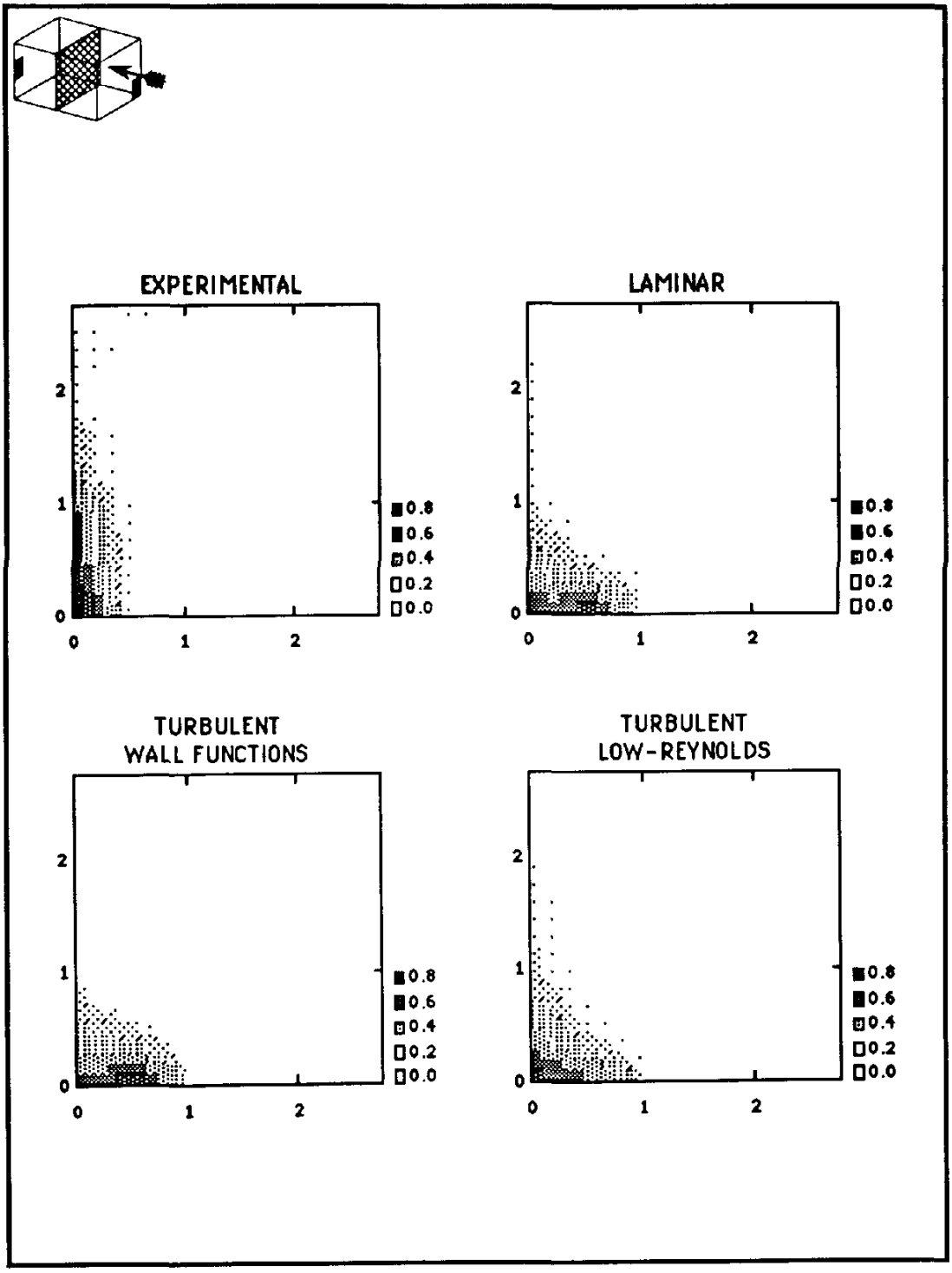

Figure 4.11. Simulation Results for 15 ACH (x=2.24 m)

30 ACH

As Figure 4.12 shows, the predicted flow patterns of 30 ACH appear to model the experimental flow pattern better than the predictions of the 15 ACH flow. However, the magnitudes are consistently less than the experimental results. In addition, the lateral plots of Figure 4.13 do not show predicted lateral diffusion which greatly exceeds the experimental flow.

This difference in velocity magnitudes may be due, in part, to the grid coverage. As discussed earlier, the computational inlet is approximately 16.5% greater than the actual inlet. If the experimental and numerical volumetric flow rates are equal, this inlet area difference creates numerical results which are on the order of 14% less than the experimental results. Another possible explanation is that a significant improvement in the inlet profile approximation may be necessary.

Based on Figures 4.12 and 4.13, it is difficult to discern which model is superior. However, it would appear that the low-Reynolds model more closely predicted both the pattern and magnitudes of the flow.

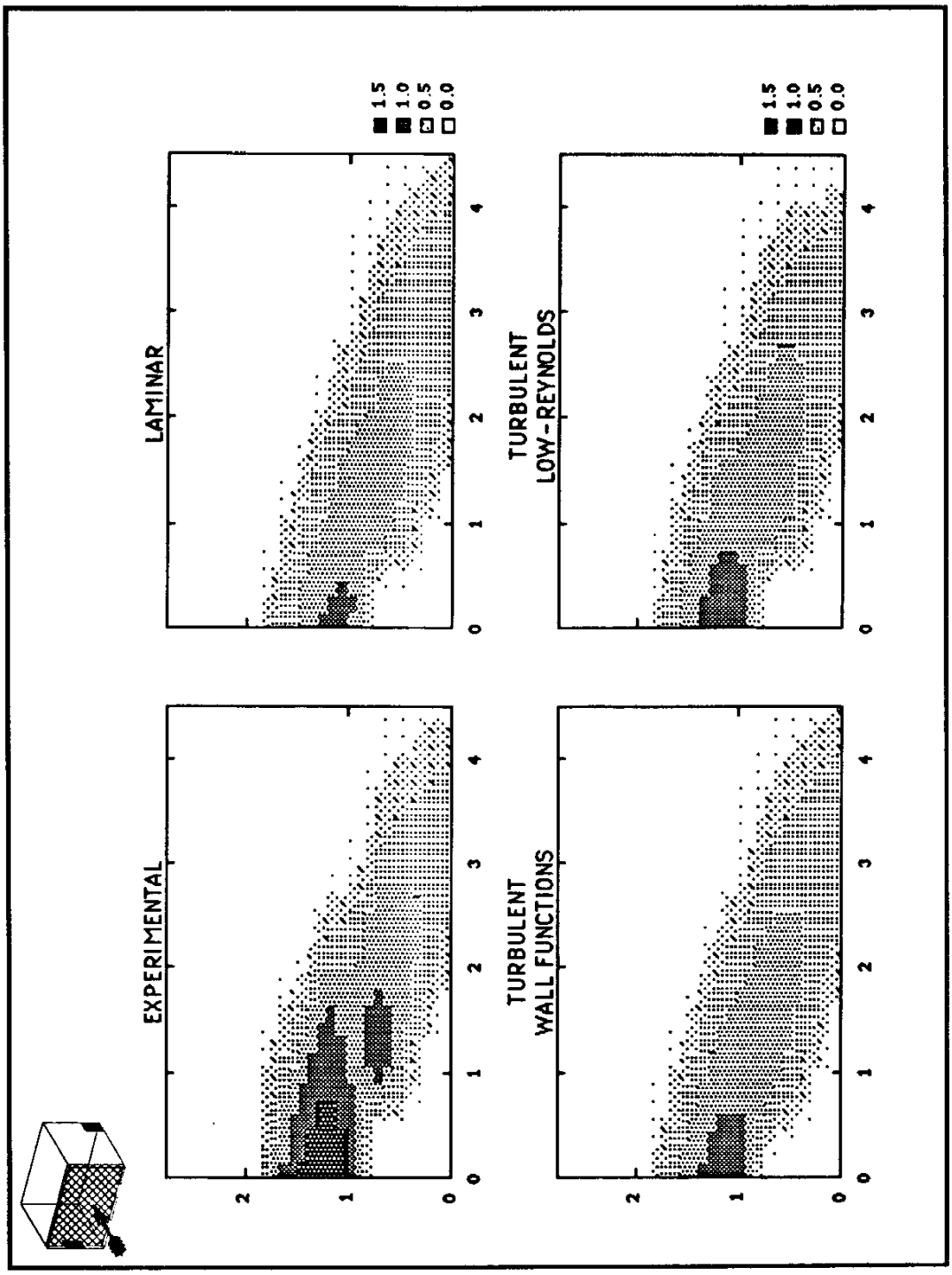

Figure 4.12. Simulation Results for 30 ACH (z=0.127 m)

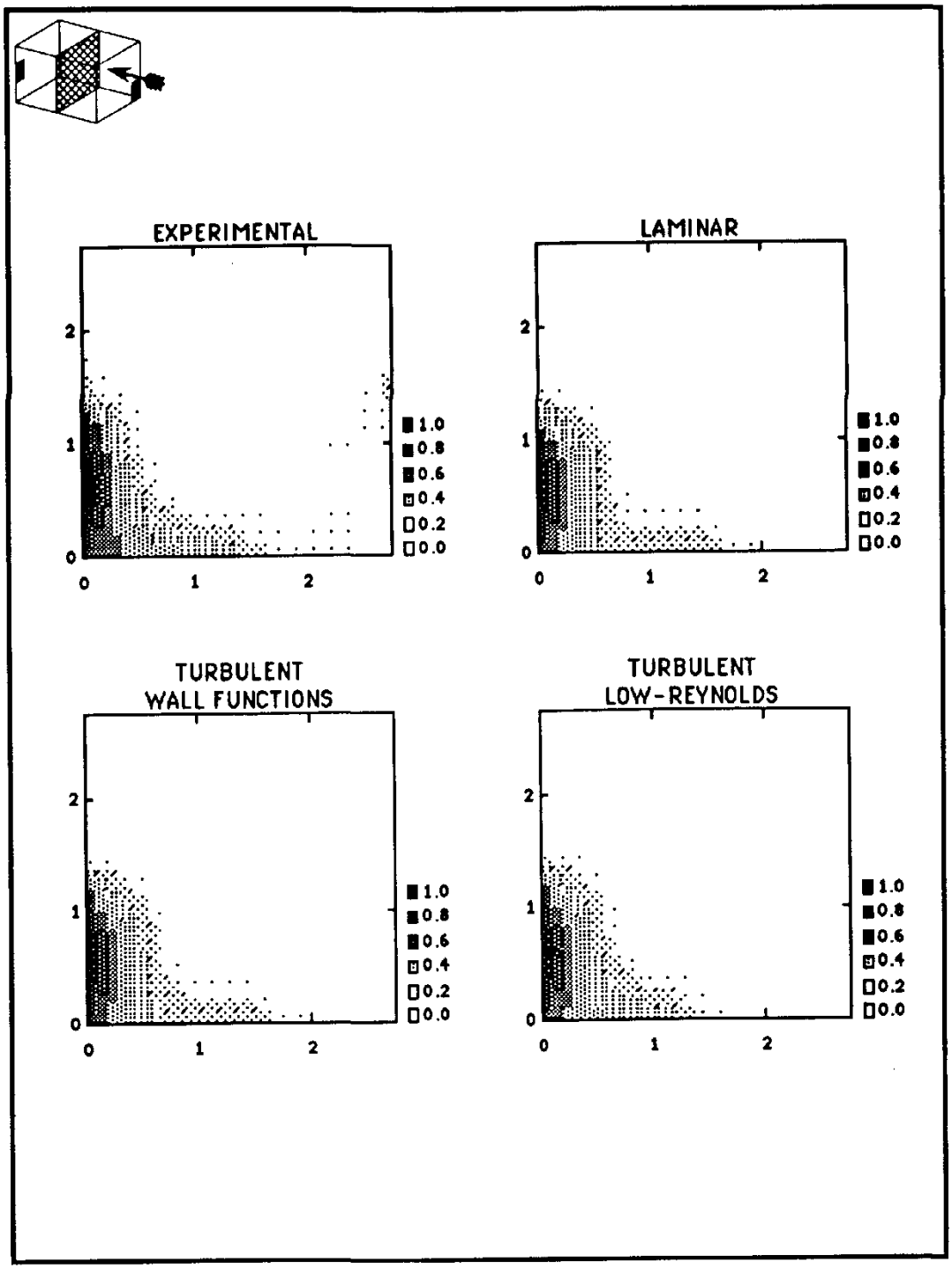

Figure 4.13. Simulation Results for 30 ACH (x=2.24 m)

50 ACH

Significant differences in the models begin to emerge at 50 ACH. As shown by Figure 4.14, the simulation results of all the models under-predicted the dissipation of the jet. Only the low-Reynolds model appeared to show significant dissipation as well as predicting magnitudes near the inlet which are in good agreement with the experimental data. In the case of the laminar and wall-function models, a jet was predicted which appeared to dissipate only due to the presence of the opposite wall. The experimental profile shows significant dissipation of the jet well before reaching the opposite wall.

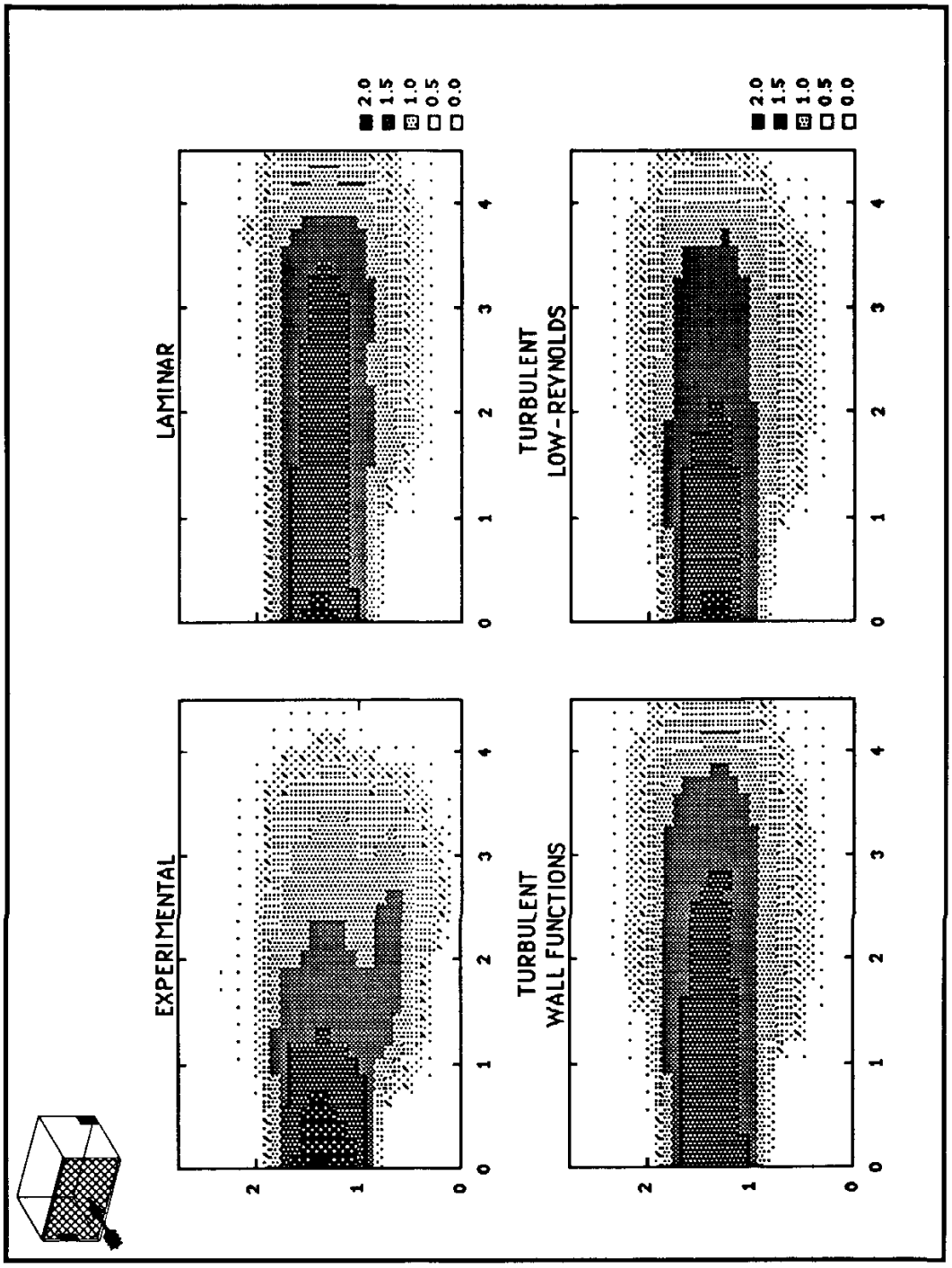

Figure 4.14. Simulation Results for 50 ACH (z=0.127 m)

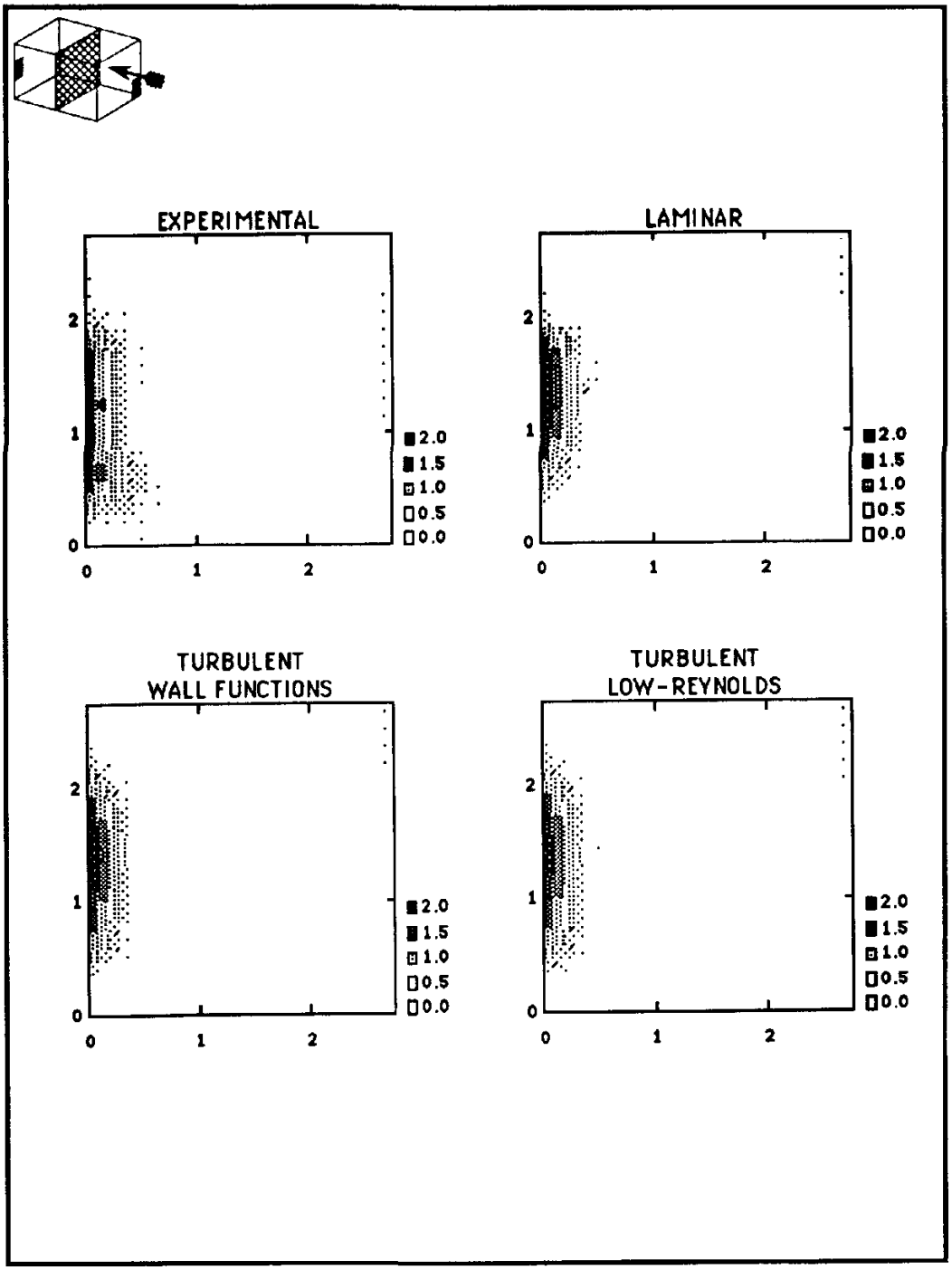

Figure 4.15. Simulation Results for 50 ACH (x=2.24 m)

100 ACH

As with the 50 ACH profiles, Figure 4.16 shows 100 ACH profiles which "under predicted" the amount of diffusion and reduction of magnitude as the jet entered the room. In fact, the laminar model appears to more closely approximate a stream striking the opposite wall, rather than a jet diffusing into a room. This is further shown by the lateral plot in Figure 4.17, in which the laminar jet appears to remain intact much more than the experimental jet, or the jets predicted by the turbulent models.

In terms of the turbulent predictors, the k-ε model with wall functions appears to better approximate the jet, particularly in the region near the inlet. One might expect this as the standard k-ε model was developed for fully turbulent flows.

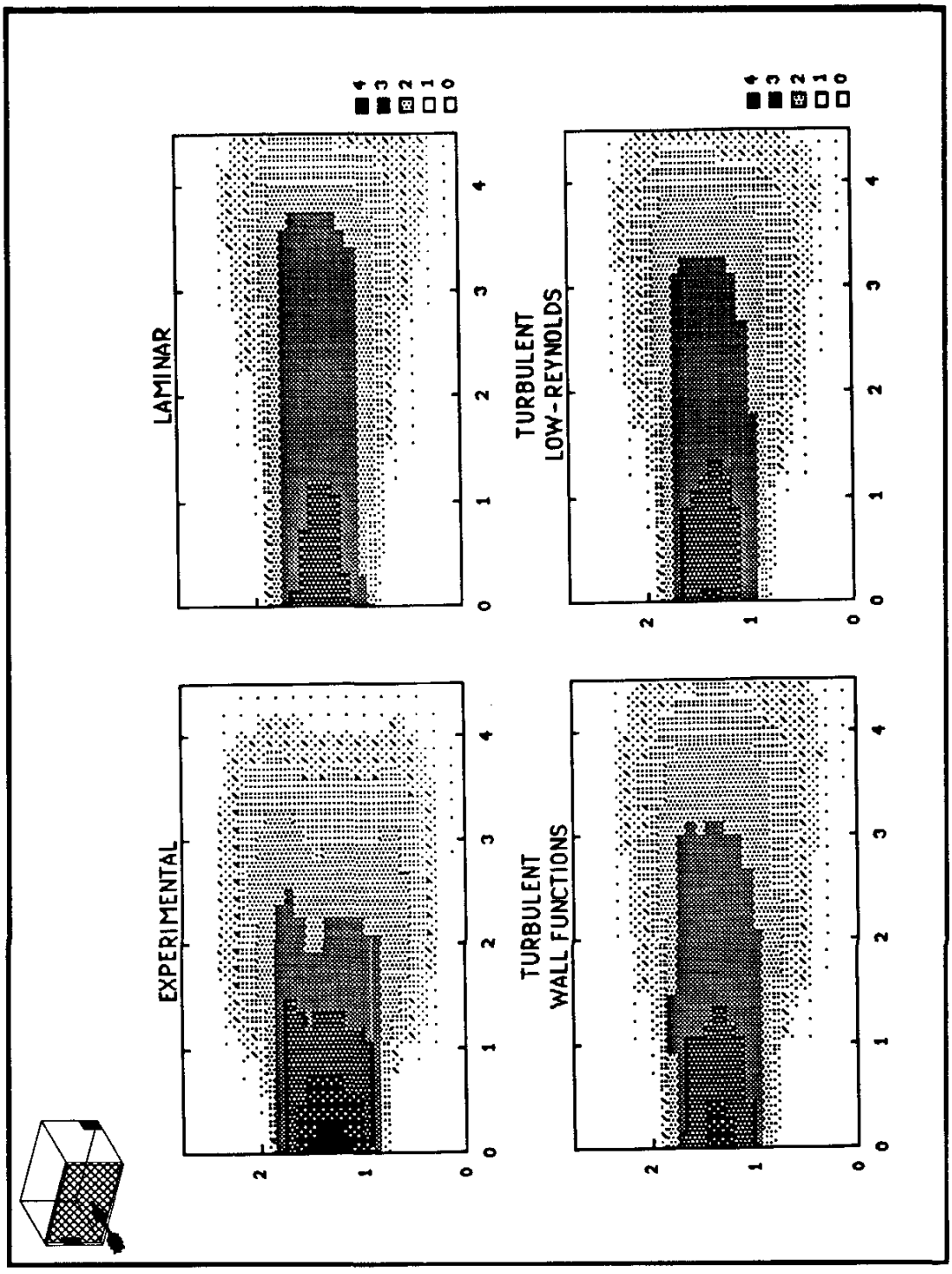

Figure 4.16. Simulation Results for 100 ACH (z=0.127 m)

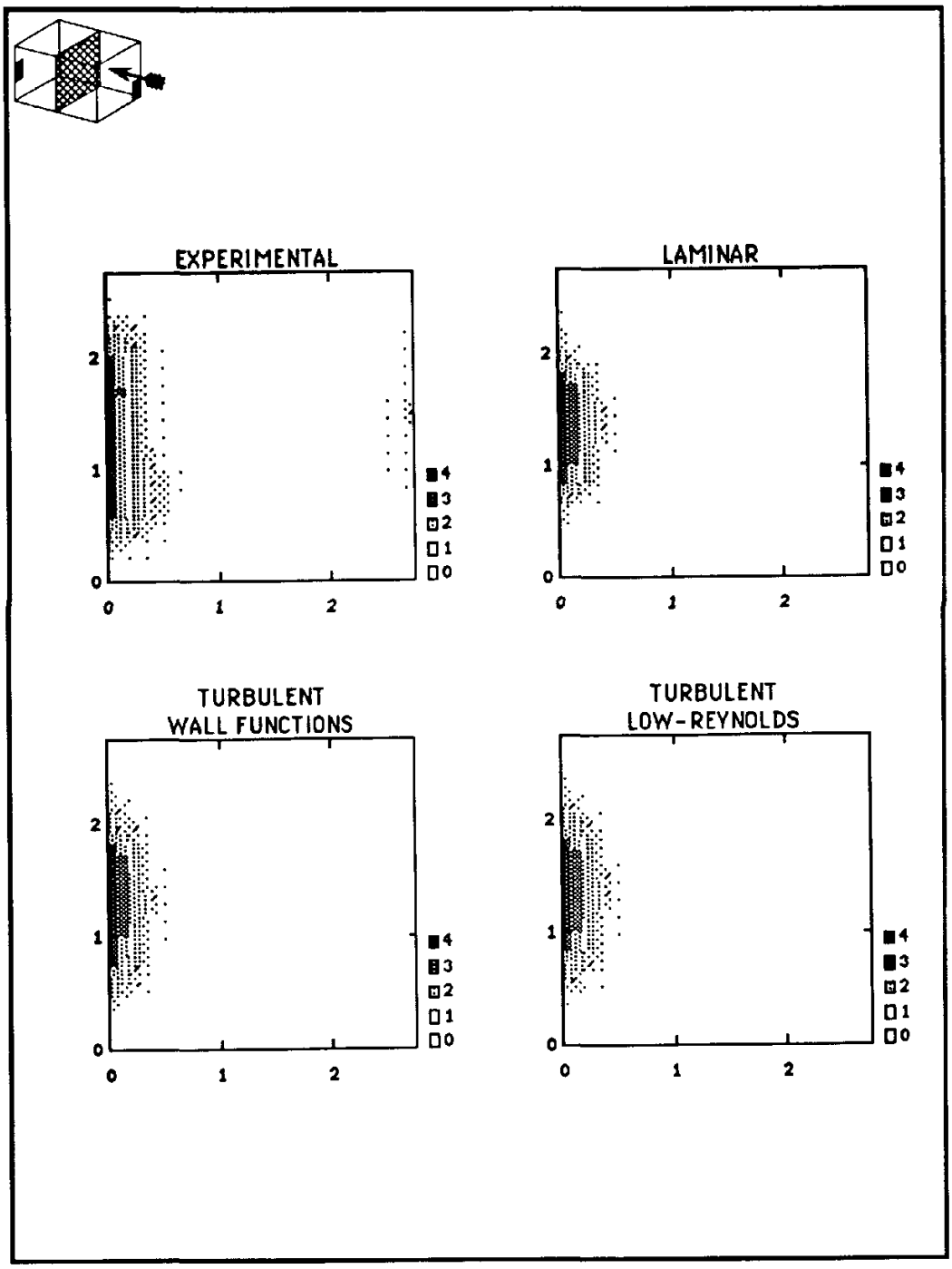

Figure 4.17. Simulation Results for 100 ACH (x=2.24 m)

Error Distributions

In most of the cases, a simple examination of the predicted profiles in comparison to the experimental profiles can adequately distinguish how well the flow is predicted by the various models. However, in an effort to highlight the extent to which predicted flows differ from the experimental results, plots have been generated for the absolute errors for each of the plots shown in Figures 4.10 - 4.17, where the absolute error is defined by the following equation.

$$E_{abs} = \left| V_{exp} - V_{num} \right|_{x,y,z} \tag{4.1}$$

These plots are presented on the following pages. Because the generated plots have been shown to contain unrealistic extrapolations, one must be careful as to the amount of confidence placed on the following error distributions. Despite this, the plots do adequately show the "problem areas" for each of the models, in addition to the relative amounts by which the models varied.

15 ACH

Figure 4.18 supports the previous statement concerning how the models did not sufficiently predict the immediate buoyant effects for the 15 ACH flow. As shown by the figure, values were predicted in the region where experimental evidence showed velocity magnitudes being decreased due to buoyant effects. However, the absolute error was reduced through the use of the low-Reynolds model.

Figure 4.19 demonstrates how the artifact problem surfaces while extrapolating values of the absolute error. These artifacts appear in the lower right portion of each of the plots. In addition, it is clear that the over-estimation of lateral diffusion by the models results in errors in the region where the jet actually remained intact, as well as in the area where the models estimated diffusion away from the wall.

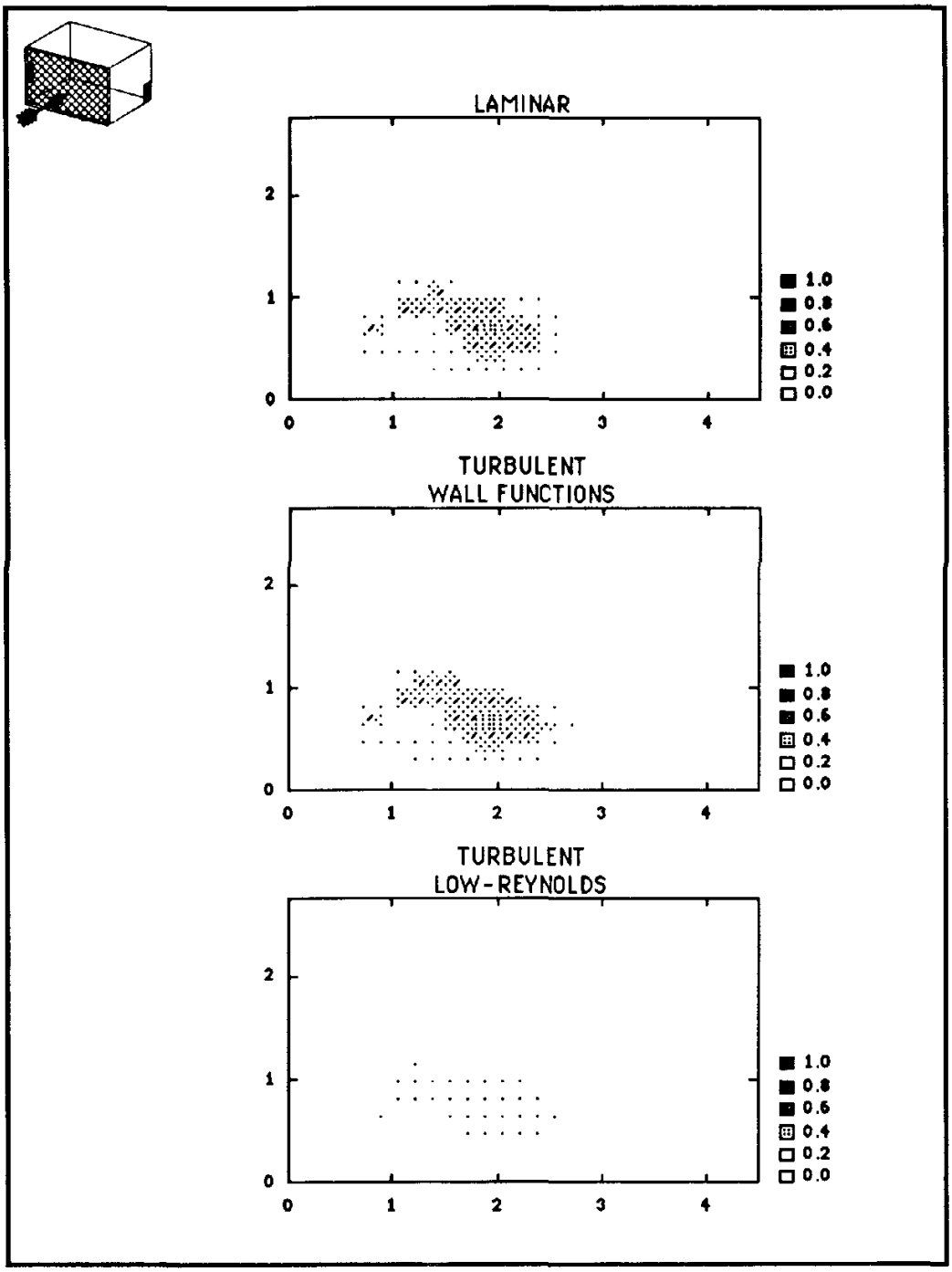

Figure 4.18. Error Distributions for 15 ACH (z=0.127 m)

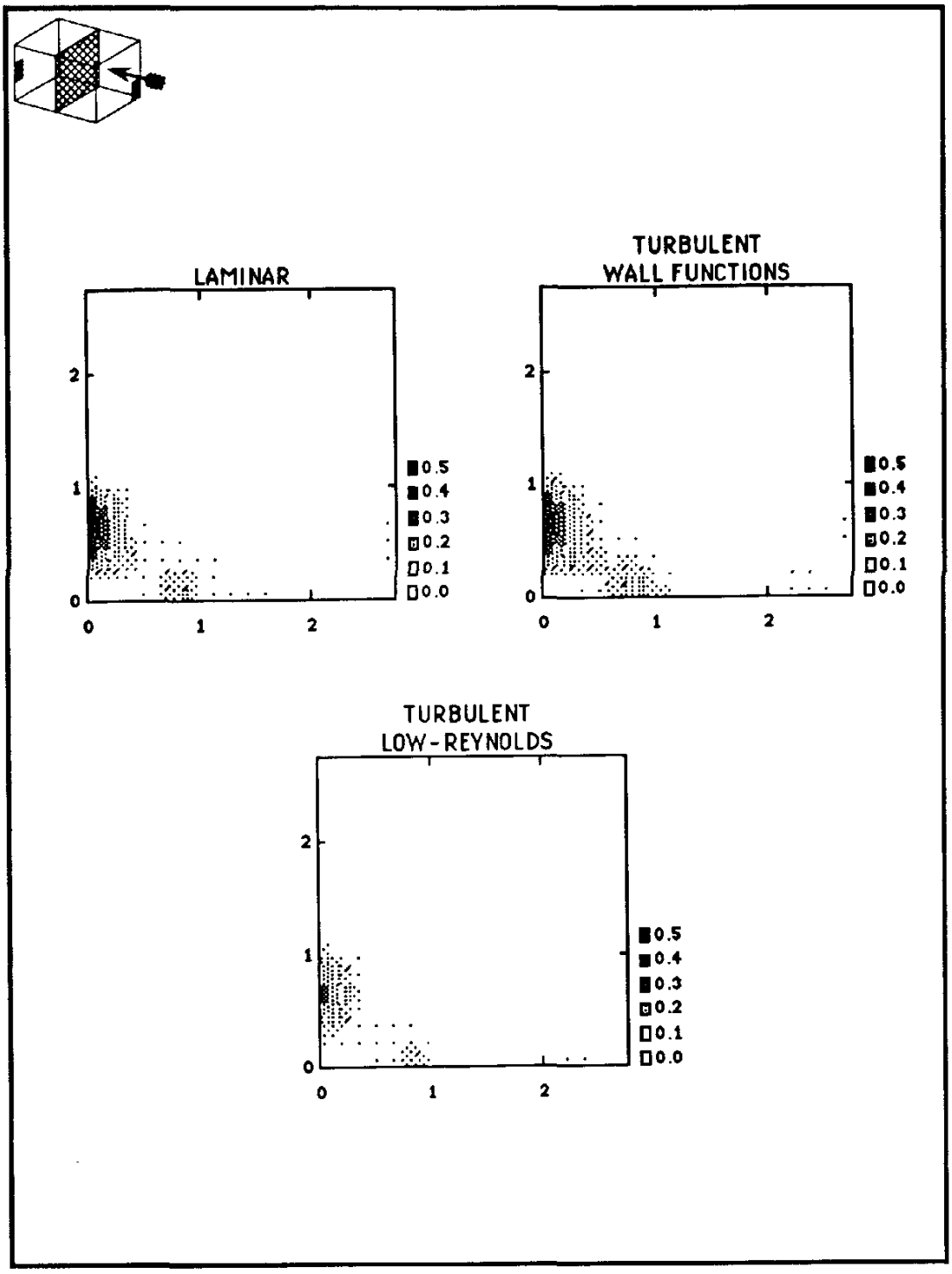

Figure 4.19. Error Distributions for 15 ACH (x=2.24 m)

30 ACH

The primary feature shown by Figure 4.20 is how the predicted velocity magnitudes were less than the actual magnitudes in the region immediately in front of the jet. The laminar model produced the greatest errors in the region, while the low-Reynolds model reduced the discrepancies.

Interesting "errors" appear just below the inlet entrance, which one would not expect after viewing the velocity magnitude distributions of Figure 4.12. These errors were probably introduced as results were extrapolated to the walls, as all three models in addition to the experimental results did not show any significant flow in this area.

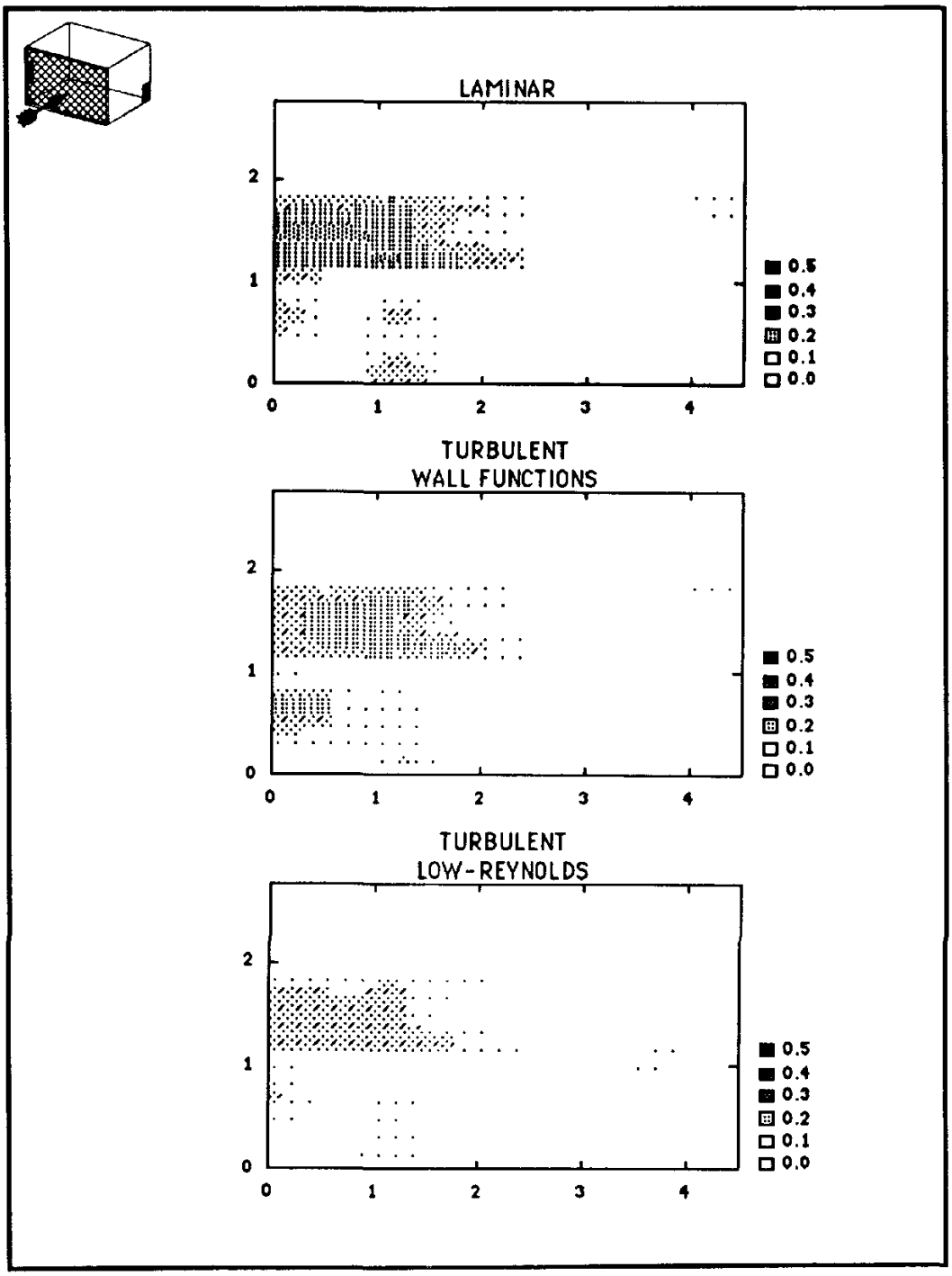

Figure 4.20. Error Distributions for 30 ACH (z=0.127 m)

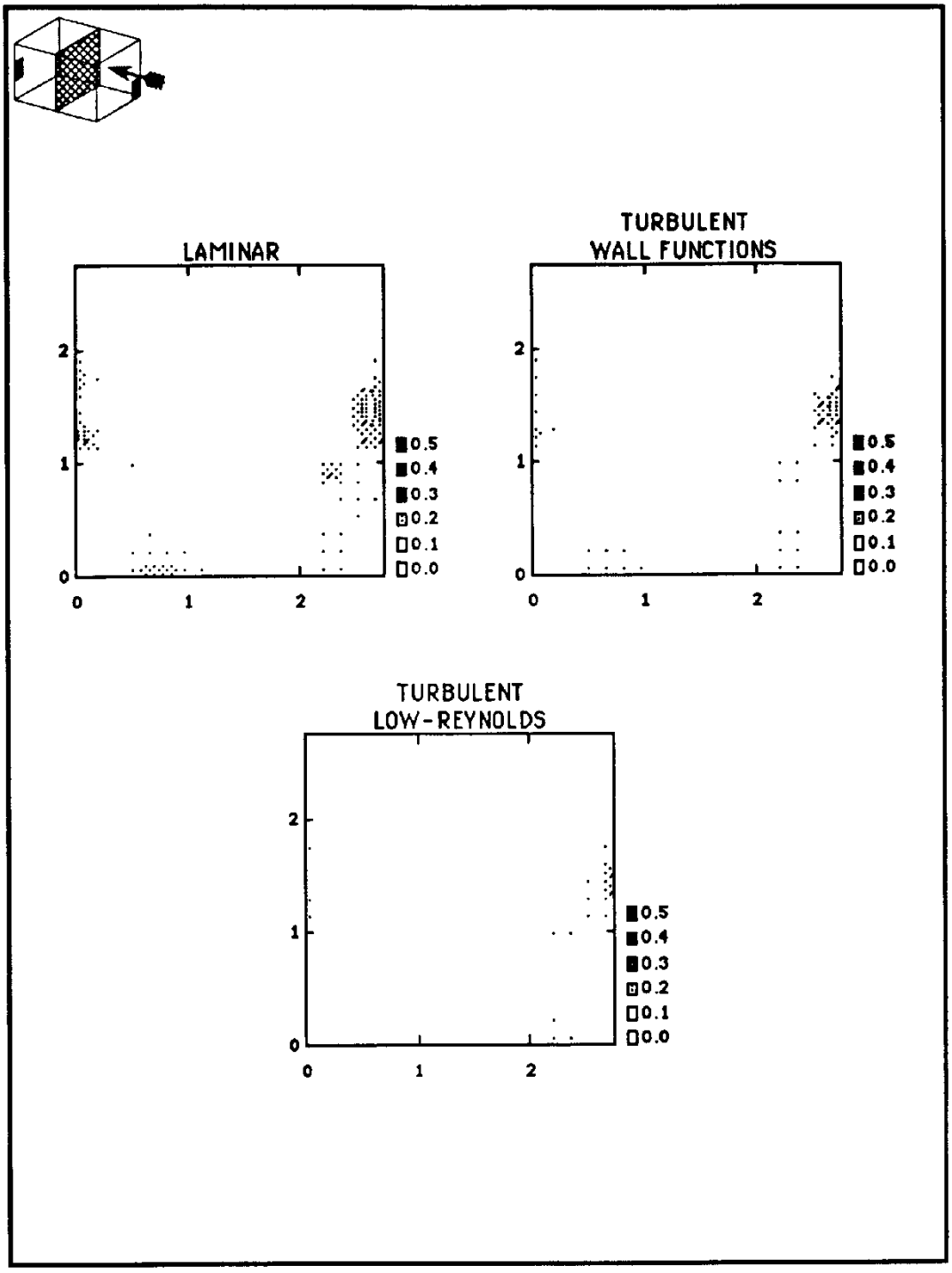

Figure 4.21. Error Distributions for 30 ACH (x=2.24 m)

50 ACH

At first glance, Figure 4.22 appears as if the coordinate system was altered and flow was entering from the opposite end of the room. In fact, this figure highlights how the models under-predicted the dissipation of the flow into the room. As shown by the figure, there is insignificant discrepancy in the region near the location of the inlet. There is severe discrepancy, especially for the laminar and wall function models, at the wall opposite the jet. The inability of these models to predict the diffusion into the room is further shown by the errors existing "beneath" the jet. In this region, the jet is diffusing into the room, perhaps partially due to buoyancy. While none of the models accurately predicted this, at least the low-Reynolds model reduced the discrepancy with experimental data.

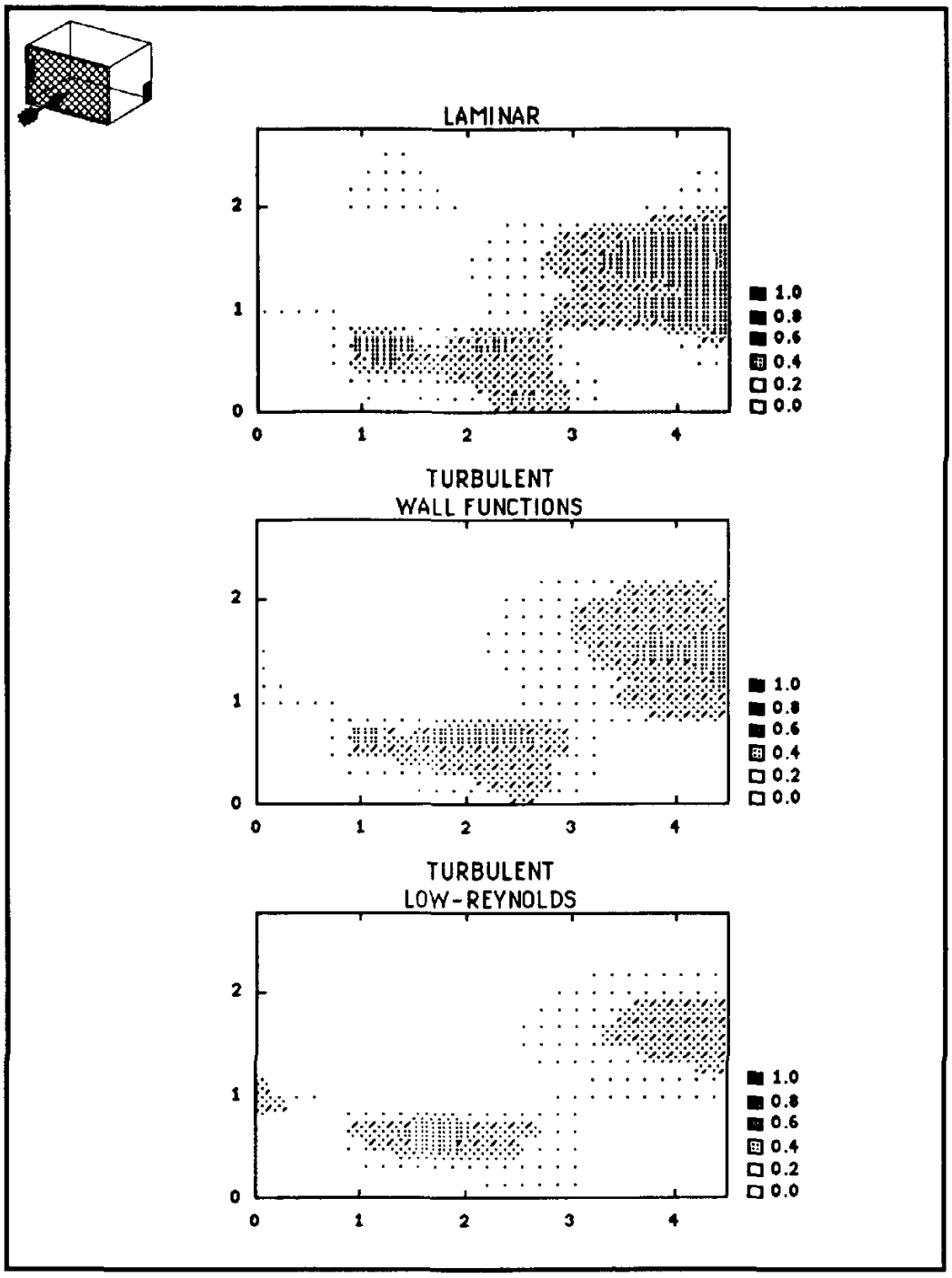

Figure 4.22. Error Distributions for 50 ACH (z=0.127 m)

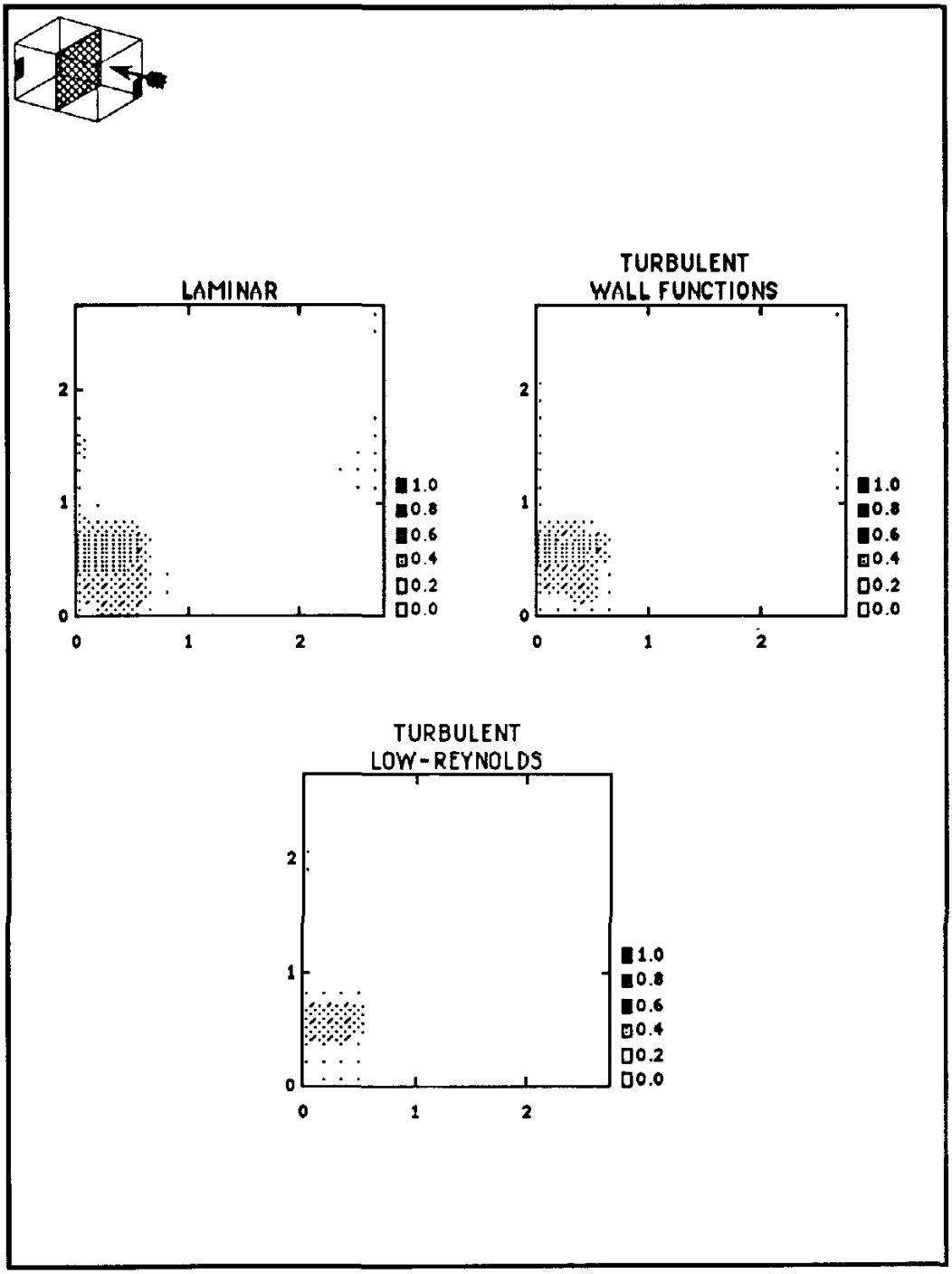

Figure 4.23. Error Distributions for 50 ACH (x=2.24 m)

100 ACH

The interesting regions of errors occurring at 100 ACH can be seen in Figure 4.25. Although it is difficult to discern, it would appear that the experimental results are showing the tendency of the jet to diffuse toward the outlet, which would be located at the lower right-hand corner of each of the plots. Again, this diffusion process appears to have been under-estimated by the models.

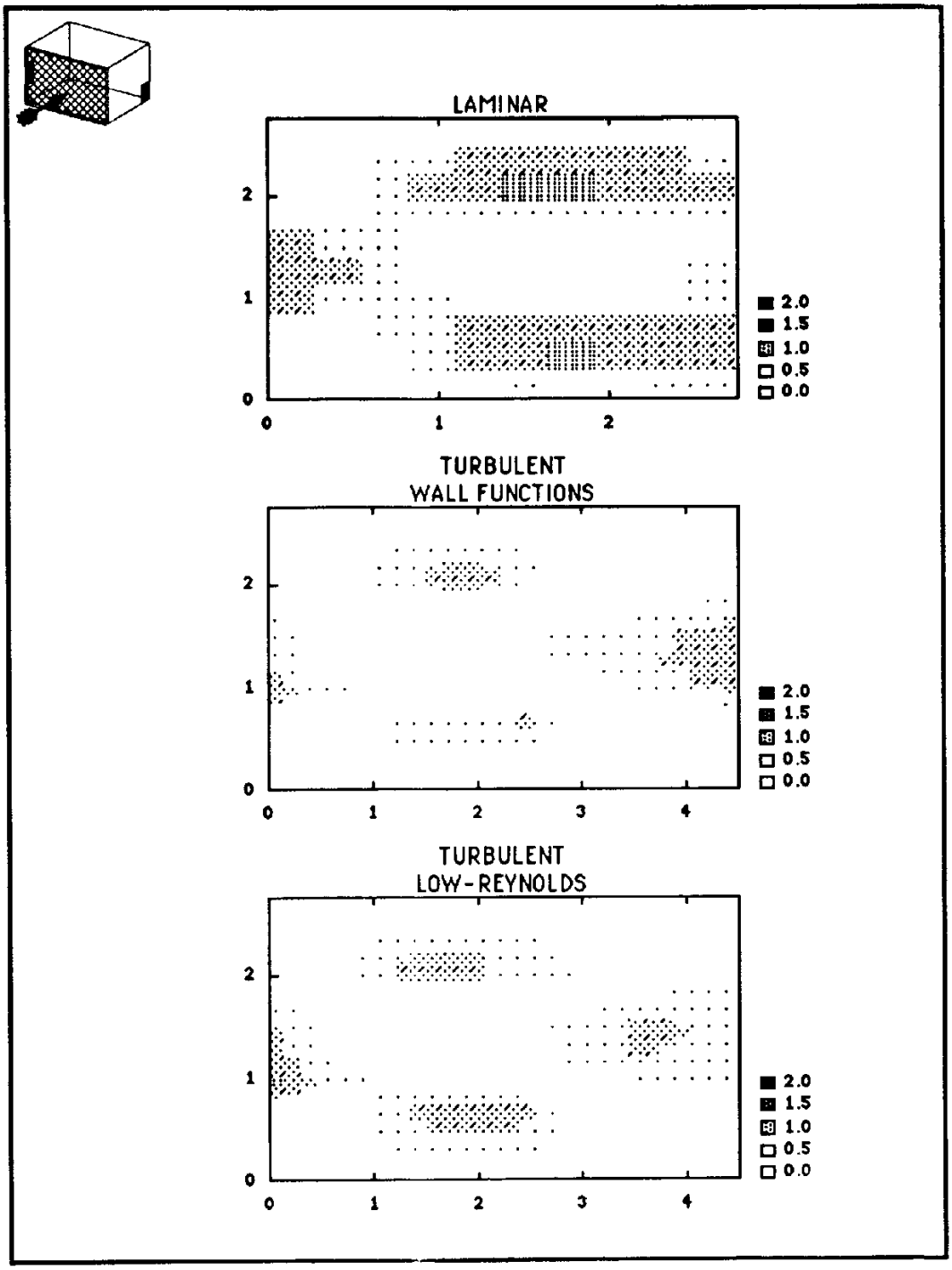

Figure 4.24. Error Distributions for 100 ACH (z=0.127 m)

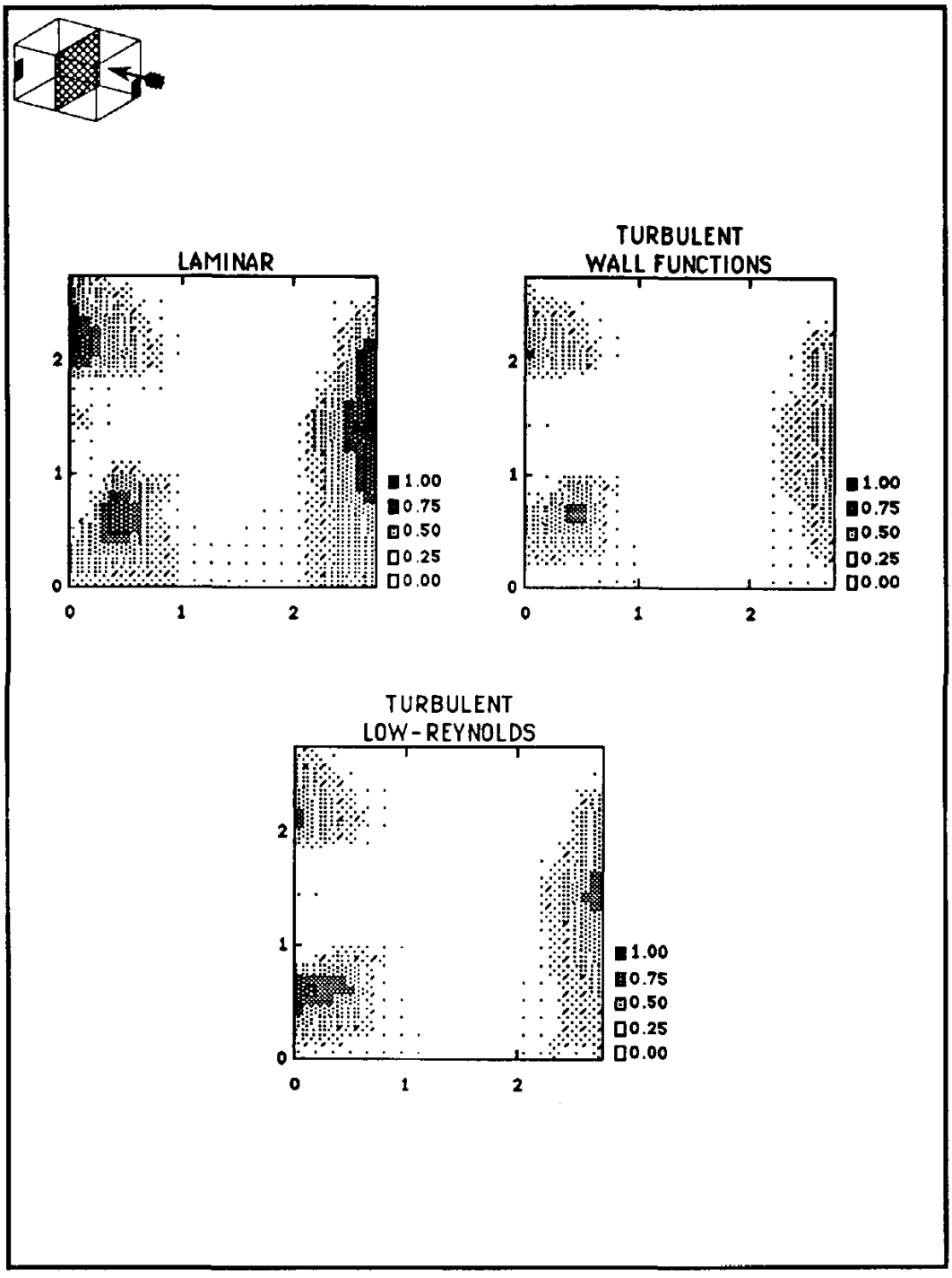

Figure 4.25. Error Distributions for 100 ACH (x=2.24 m)

Solution Errors

Figures 4.18 - 4.25 adequately show how the computed results differ from experimental results at various locations within the room. However, it is difficult to use these plots to compare the overall accuracy of the various methods for a given simulation. It is then necessary to define some type of global error which may be compared, regardless of the flow rate. This error could be defined several ways. For the purpose of comparison, the global error number (G.E.N.) will be defined by the following equation.

$$\text{G.E.N.} = \frac{\overline{E}_{abs}}{V_{max}} \tag{4.2}$$

where $\overline{E}_{abs}$ =Average absolute error $\left(\frac{1}{n}\sum E_{abs_i}\right)$

V_{max} = Maximum velocity magnitude from experimental data

The summation of Eq(4.2) is for all 896 points at which experimental data was collected (i.e., n=the number of experimental points).

Using Eq(4.2), values for the general error number were calculated and are given in Table 4.4. A graphical representation is also provided in Figure 4.26.

TABLE 4.4

GLOBAL ERROR NUMBER VALUES

Model	**15 ACH**	**30 ACH**	**50 ACH**	**100 ACH**
Laminar	0.0498	0.0570	0.0767	0.0796
Turbulent - Wall Functions	0.0505	0.0560	0.0683	0.0743
Turbulent - Low-Reynolds	0.0358	0.0449	0.0554	0.0596

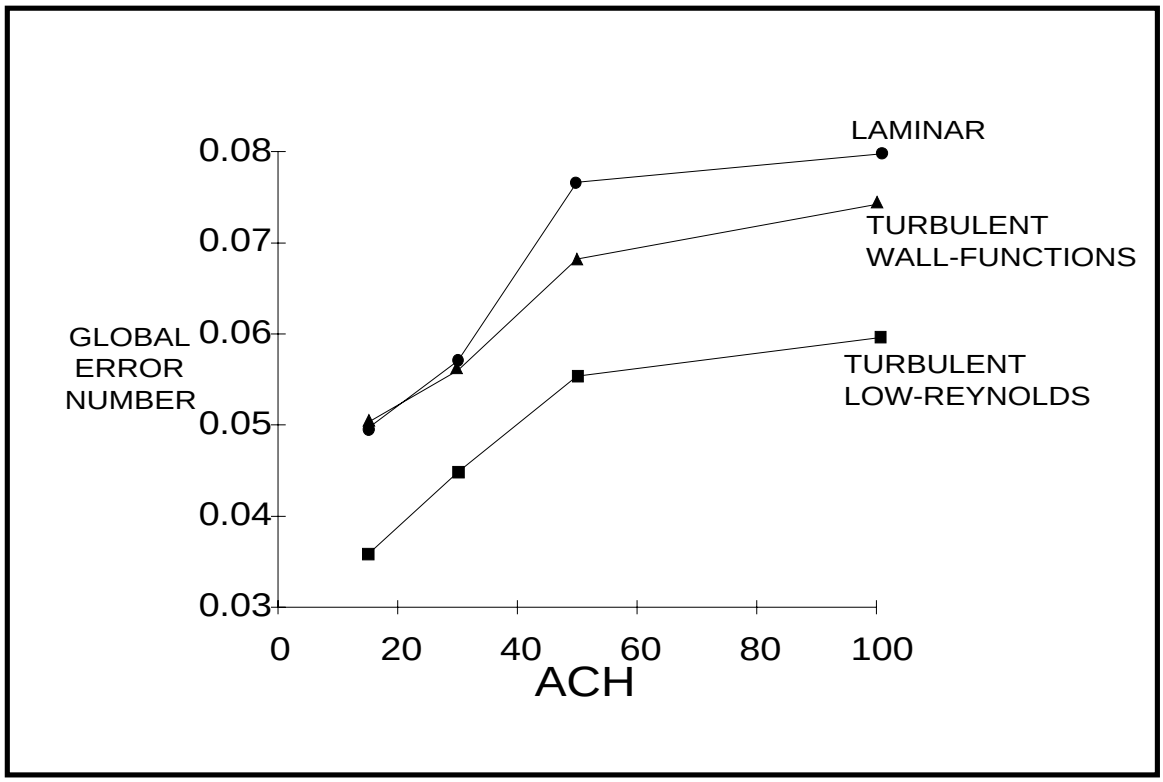

Figure 4.26. G.E.N. vs Flowrate Comparisons

As shown by Figure 4.26, the simulation error increases as the flow rate is increased. If the trends of the graph are examined, it would appear that as the flow rate is further increased beyond 100 ACH, there would exist some maximum global error number. However, the existence of such an upper limit on the solution error could only be proven by further comparison to experimental data.

For all three models, the strongest error sensitivity to the flow rate occurs for flows less than 50 ACH. In fact, the sensitivity for all three models (i.e., the slope of the lines) is nearly the same both above, and below 50 ACH.

An interesting fact is that the global error numbers for the laminar and turbulent wall function models do not begin to differ much until 50 ACH. One might expect such a relationship, as the standard k-ε model is considered valid for high Reynolds number

flow. Therefore, as the flow rate increases, so does its level of turbulence, until the level reaches a point in which the laminar model can no longer predict its behavior as well as the wall function model.

The basic trend of the graph, is what one would intuitively predict. That is, the laminar model contains the greatest global error, with the two turbulence models containing less discrepancies to the experimental data. For all flow rates, the difference between the G.E.N. for the low-Reynolds model and the other two models remains nearly constant.

Computational Time

While the previous discussion of computational time was concerned with grid size, it is important to address the computational requirements of each of the three modeling techniques.

All simulations were performed on an IBM RISC-6000 mainframe. Table 4.5 details the computational time (minutes) required by the computer to complete the simulations. Actual simulation times varied, as all simulations were performed in the background through the use of batch files.

TABLE 4.5

COMPUTATIONAL TIMES FOR MODELS

Computational Time (minutes)				
Model	**15 ACH**	**30 ACH**	**50 ACH**	**100 ACH**
Laminar	116.35	110.03	149.06	172.37
Turbulent - Wall Functions	178.13	169.37	235.77	253.92
Turbulent - Low-Reynolds	217.12	198.35	256.18	302.12

It is very important to note that any discussion on computational time is highly subjective and care should be taken when comparing the values in Table 4.5. Obviously, the necessary computational time is determined by the computer used for simulations. In addition, this subjectivity is due to two other reasons.

First, the computational time is strongly dependent on the size of the time step. Thus, the proper or improper selection of the simulation time step could significantly reduce or increase the necessary computational time.

The most significant subjectivity in the computational times of Table 4.5 involves the program being used to model the flow. While diligence was used during the program development, there is no guarantee concerning its computational efficiency. The use of other modeling algorithms would also increase or decrease the computational requirements. It is anticipated that modifications could be made to the program to increase its efficiency, including the use of initial velocity profiles within the room.

For the sake of discussion, it could be assumed that the relative times in Table 4.5 could be compared to determine the necessary computational requirements of a model in comparison to the others. Averaging the computational times of Table 4.5, and dividing by the smallest value, new computational times can be calculated. The values for these times are in Table 4.6.

TABLE 4.6

COMPUTATIONAL TIME COMPARISON

Model	**15 ACH**	**30 ACH**	**50 ACH**	**100 ACH**	**Average Time**
Laminar	1.0	1.0	1.0	1.0	1.0
Turbulent - Wall Functions	1.53	1.54	1.58	1.47	1.53
Turbulent - Low-Reynolds	1.87	1.80	1.71	1.75	1.78

These relative computational times reduce the subjectivity of a discussion on computational costs. Based on this data, it takes 53% more computational time to use the k-ε model with wall functions and 78% more time with the low-Reynolds model, than what it would to perform the simulations using only the laminar flow assumptions. Such a distribution is expected, as the low-Reynolds model requires the computation of several additional parameters including turbulent viscosity and local Reynolds numbers, in addition to the solution of the k-ε equations. The k-ε model with wall functions only requires the additional solution of the two partial differential equations, and no solution of any additional turbulent parameters.

Flow Patterns

While the contour plots of velocity magnitudes allow an adequate graphical comparison to be made between numerical and experimental data, the overall flow pattern is difficult to discern from the plots. In an effort to provide additional insight into the room air flow patterns, two-dimensional velocity vector plots are presented in this section for simulations of 15 and 100 ACH using the low-Reynolds model. For each flow rate, results are presented on four different planes within the room. Different scaling factors are used for each flow rate. Thus, the 15 ACH results are not scaled by the same ratio as the 100 ACH results.

15 ACH

Figure 4.27 shows how the buoyant forces act on the low velocity jet, causing the jet to travel downward upon entering the room. The jet appears to then travel along the floor, causing a slight amount of recirculation immediately beneath the inlet as well as near the central region by the far wall on the right side of the plot. The figure also shows that the upper half of the room is relatively unaffected by the presence of the low velocity jet.

Figure 4.28, located by the side wall adjacent to the outlet, shows very little sign of air movement, except for the region immediately in front of the outlet.

Figures 4.29 and 4.30 show the primary flow pattern in the lower half of the room. In Figure 4.29, it can be seen how the air flows along the floor toward the outlet. Slight recirculation is shown in the upper left portion of the plot. In Figure 4.30, the jet seems to disappear, as the only region showing significant flow is immediately downstream of the inlet. Thus, the air is flowing beneath this plane, leaving the upper half of the room relatively unaffected.

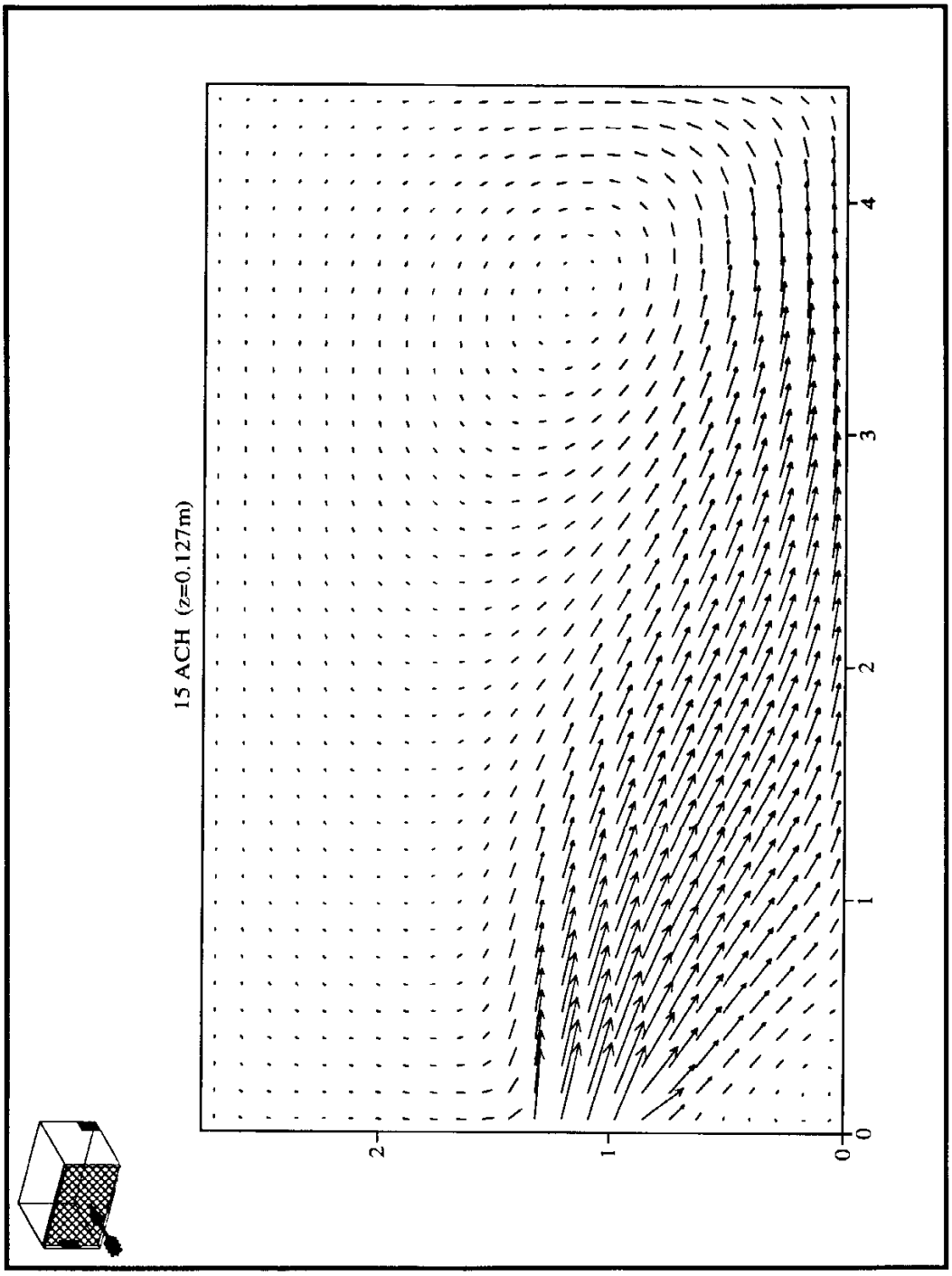

Figure 4.27. Flow Pattern for 15 ACH (z=0.127m)

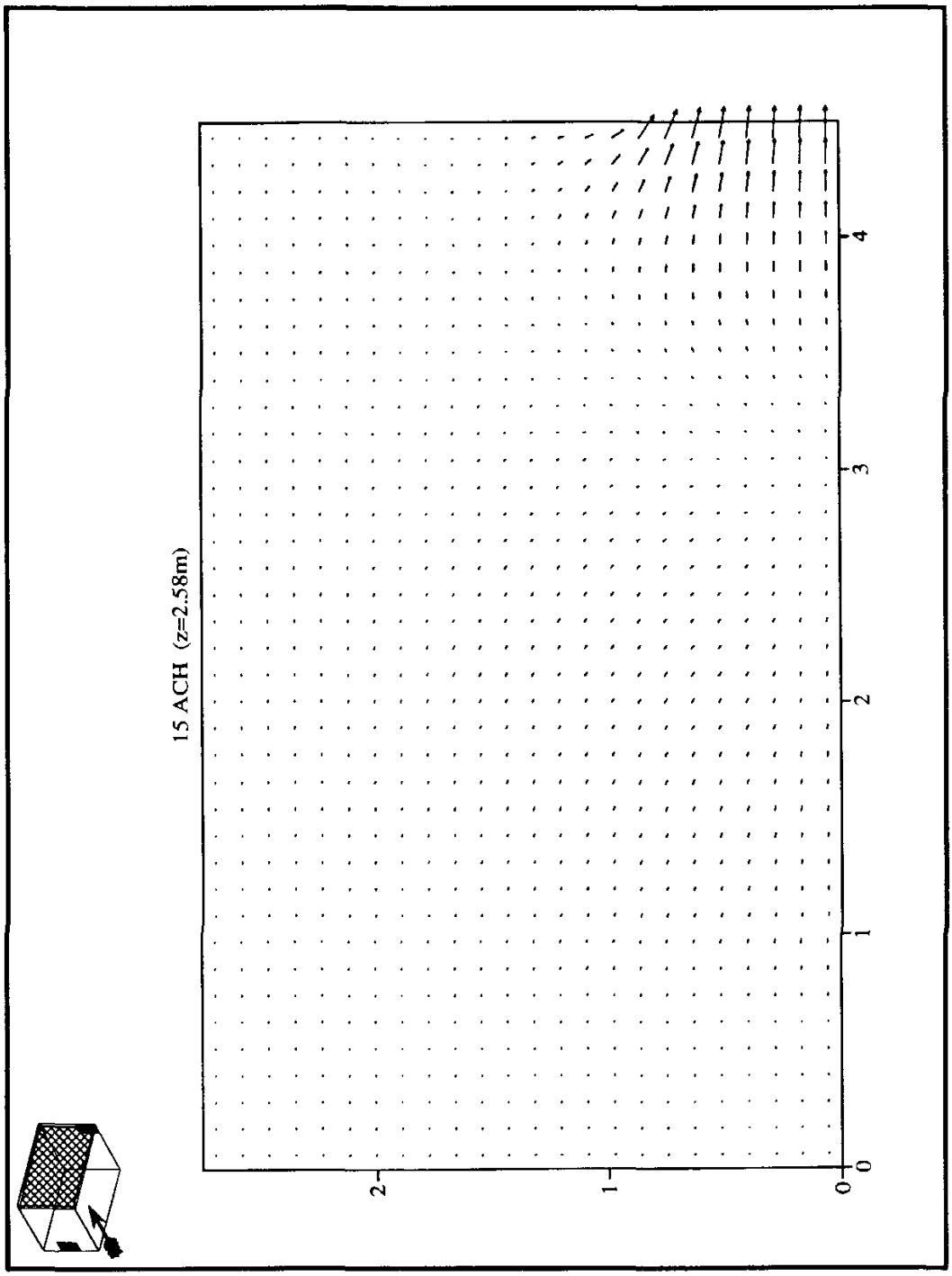

Flow Pattern for 15 ACH (z=2.58m)

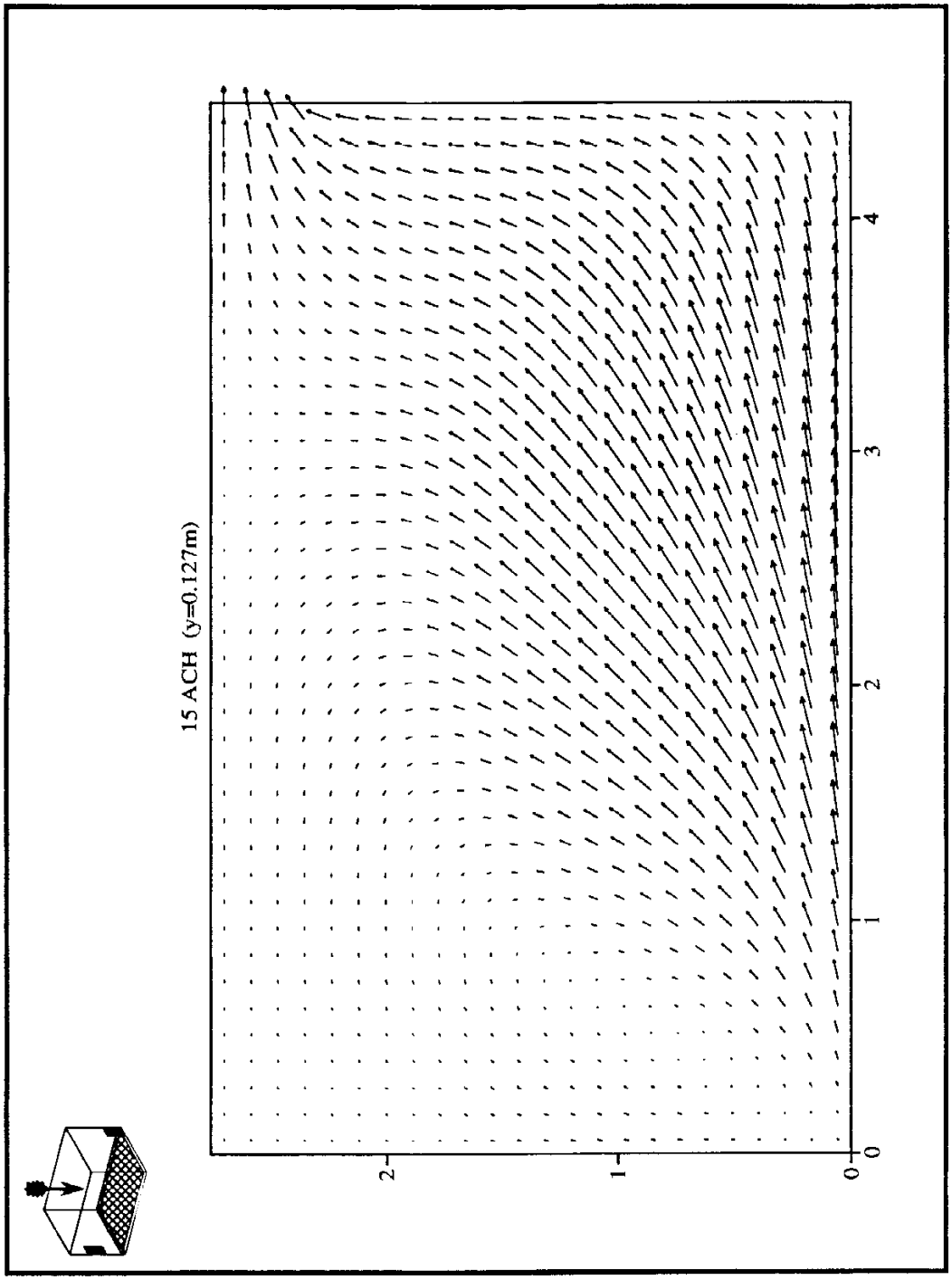

Flow Pattern for 15 ACH (y=0.127m)

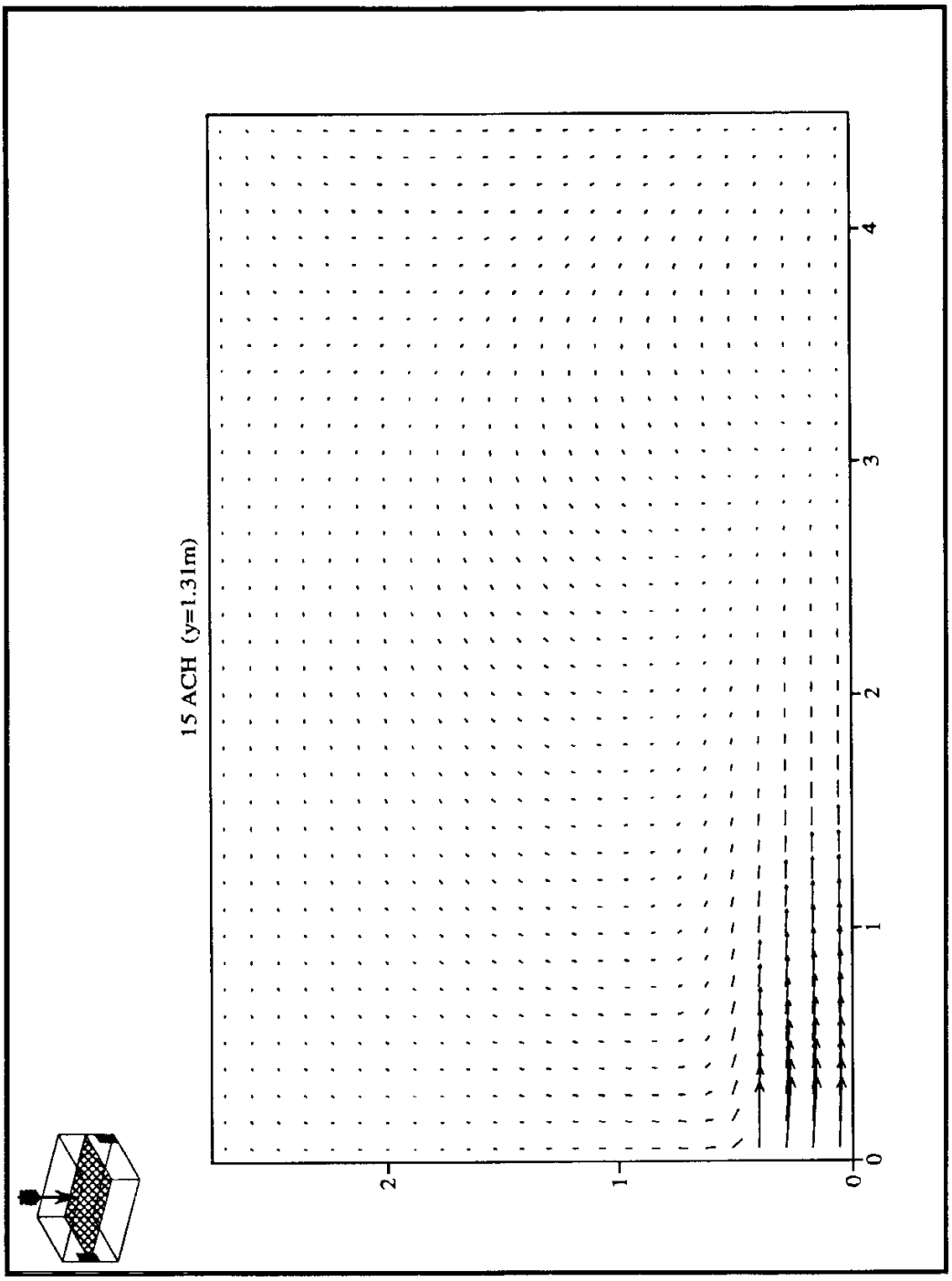

Flow Pattern for 15 ACH (y=1.31m)

100 ACH

The dramatic differences between the low and high velocity air flow patterns are highlighted with the plots of 100 ACH. The lack of dissipation mentioned earlier is shown in Figure 4.31, as the jet dissipates very little before reaching the far wall. Regions of recirculation appear above and below the jet, as it appears that some amount of entrainment occurs.

Figure 4.32 shows more air movement along the far wall for 100 ACH than what was previously shown for 15 ACH. Still, it would appear that there are some unaffected regions of the room, despite the significant increase in the inlet jet velocity.

Figure 4.33 shows a flow pattern along the floor which is quite similar to the flow pattern of 15 ACH at the same location. Figure 4.34 shows a jet being discharged along the side wall, before being diverted toward the outlet by the wall on the right side.

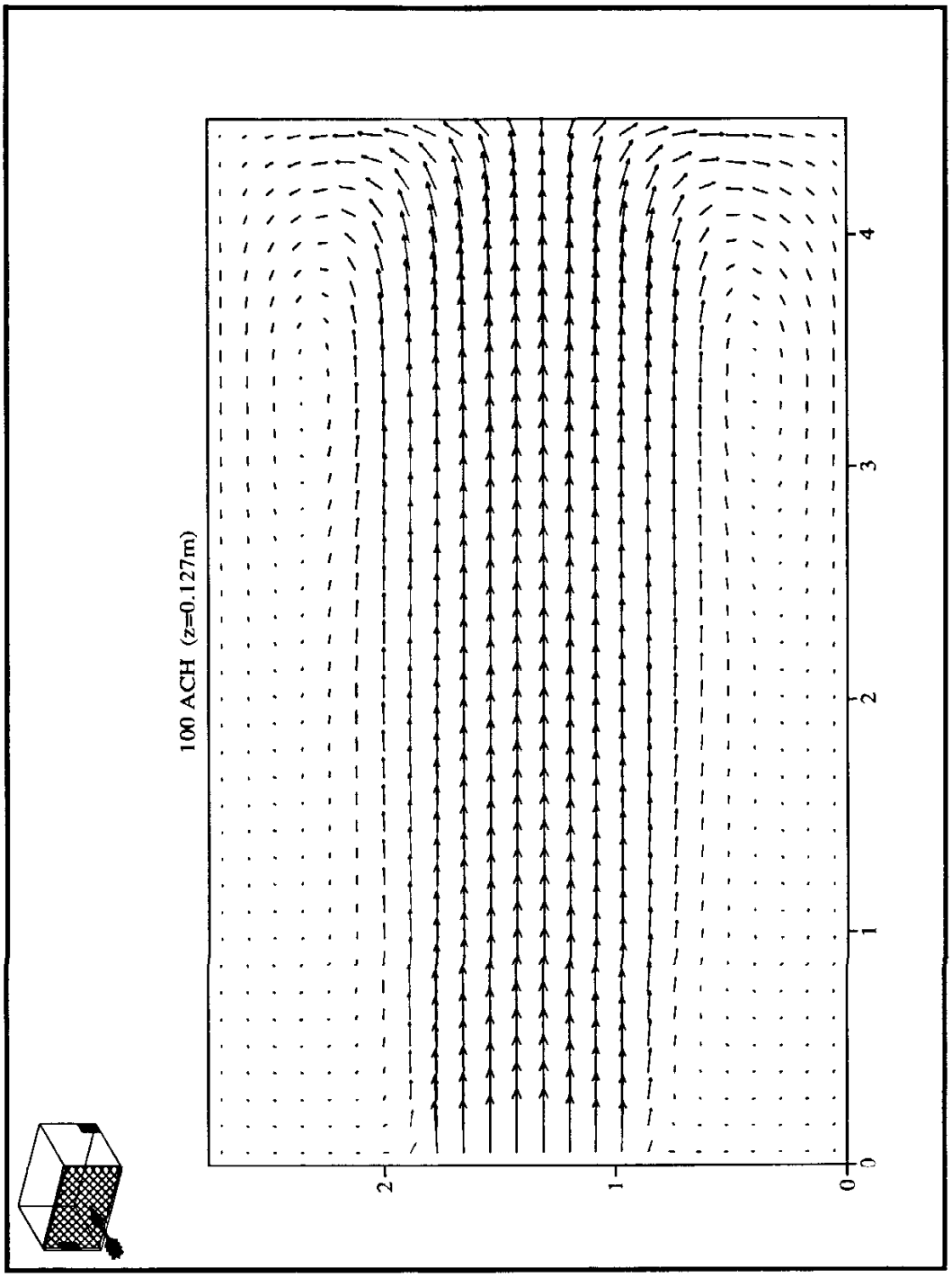

Figure 4.31. Flow Pattern for 100 ACH (z=0.127m)

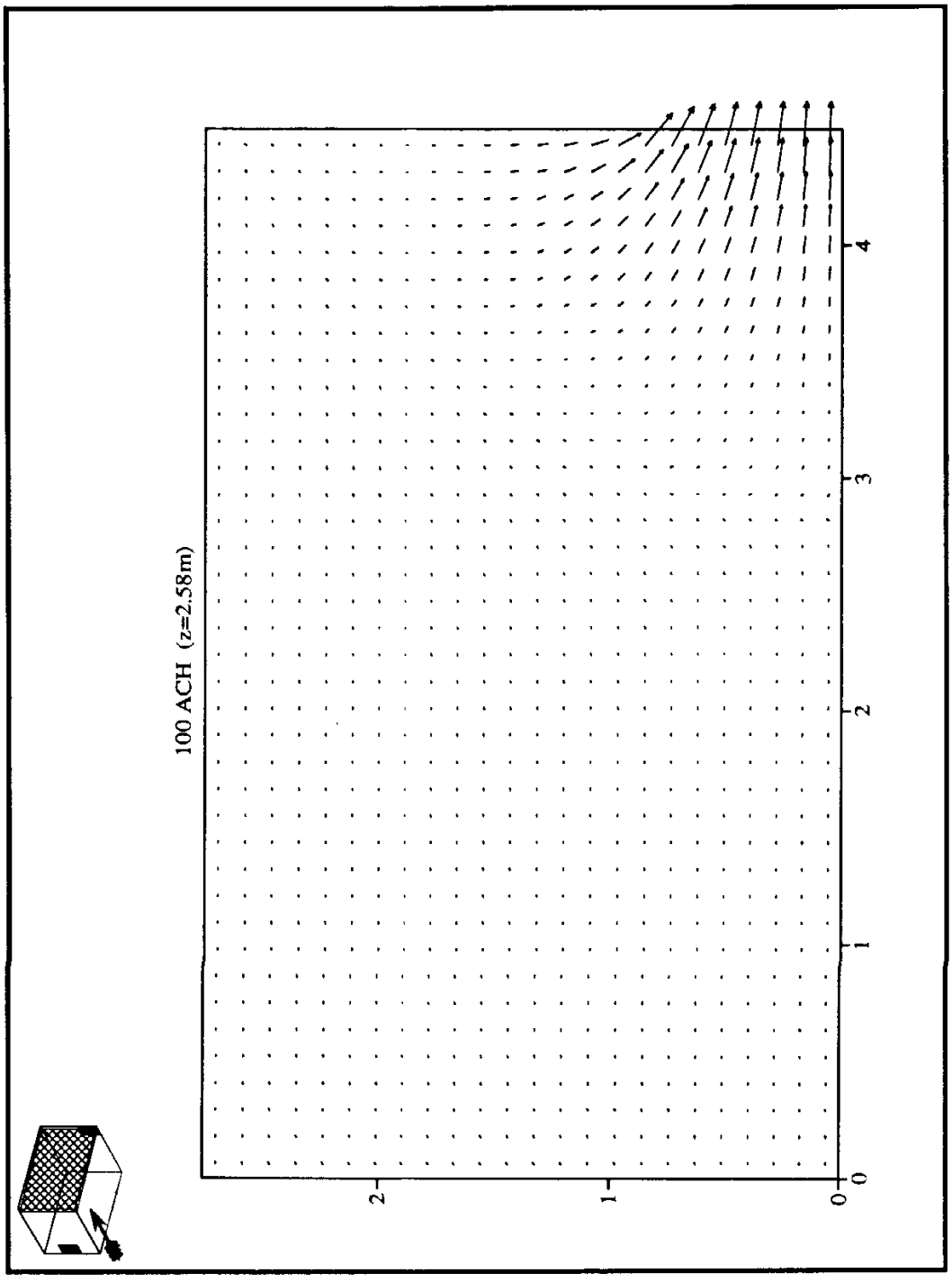

Figure 4.32. Flow Pattern for 100 ACH (z=2.58m)

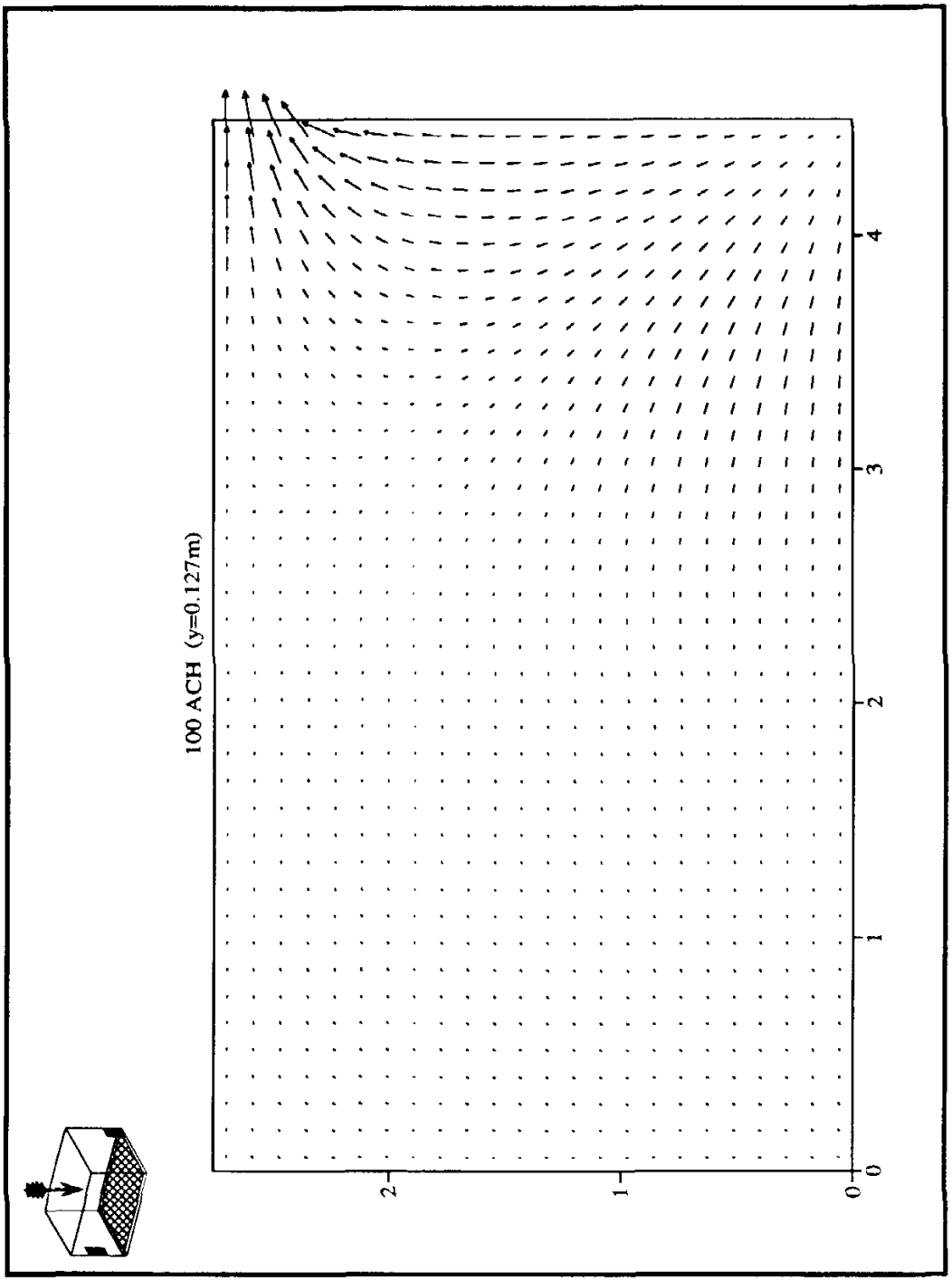

Figure 4.33. Flow Pattern for 100 ACH (y=0.127m)

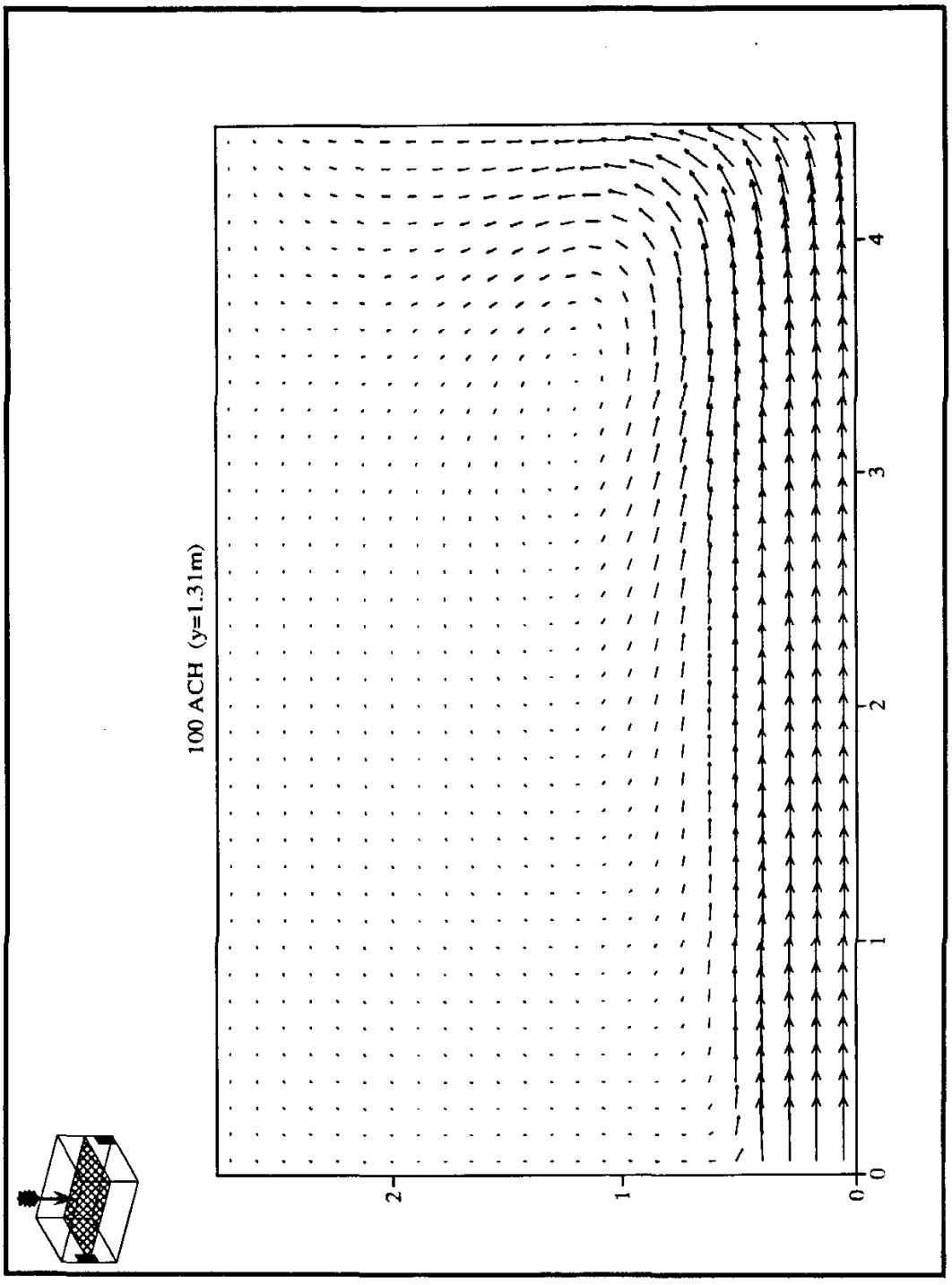

Figure 4.34. Flow Pattern for 100 ACH (y=1.31m)

CHAPTER V

CONCLUSIONS AND RECOMMENDATIONS

Summary

Application of computational fluid dynamic techniques to room flows was evaluated by comparing numerical predictions to experimental data. The room was 15 x 9 x 9 ft. with air flow rates of 15, 30, 50, and 100 ACH.

Computer code was developed to solve incompressible, buoyant flow problems with the room. Turbulence was modelled through the implementation of the k-ε model, both with the wall functions and in low-Reynolds form (Lam-Bremhorst version). Investigations were made concerning grid size, wall boundary conditions, and inlet profiles.

Conclusions

Based on the numerical simulations and comparisons to the experimental data during the course of this project, the following conclusions may be drawn.

(1) A 40 x 24 x 24 mesh was found to adequately model the flow. The use of this mesh provides approximately 25 times more discrete data points than what was provided by the experimental data. Any additional accuracy of a finer mesh was found to be insignificant in comparison to the additional computational time.

(2) Free-slip conditions at the wall when using the laminar and low-Reynolds models provide results in better agreement with the experimental data than the no-slip condition.

(3) The use of an approximate non-uniform inlet profile based on experimental data provided better comparisons than a uniform velocity profile. This project is

unique because most modeling situations will not have access to experimentally measured inlet profiles. However, this does highlight the need for particular attention when modeling the inlet profile.

(4) By defining a dimensionless global error number, the three modeling methods could be compared regardless of the flow rate. The low-Reynolds k-ε model was found to consistently generate better comparisons with the experimental data. Listed by increasing global error number, the methods are: low-Reynolds k-ε model, k-ε model with wall functions, and the laminar model.

(5) The k-ε model with wall functions required 53% more computational time and the low-Reynolds model required 78% more computational time than the laminar solution algorithm.

(6) There exists a strong trade-off between computational accuracy and required computational resources. While the use of the laminar model did not predict the flow as well as the turbulent equations, it did produce results which adequately modelled the general nature of the flow patterns at greatly reduced computational requirements. Therefore, depending on the application, the solution of the laminar continuity and momentum equations may sufficiently predict room air flow.

(7) Results were obtained which matched well with the experimental data. However, the following questions remain unanswered, and are topics for future research.

- Why do the models over-predict in some situations and under-predict in others?
- Why did the models have difficulty predicting the drastic buoyant effects exhibited at the low flow rates?
- Why do all three models predict more lateral diffusion at 15 ACH than what was experimentally measured?
- Why did the models, particularly the turbulence models, fail to predict the dissipation of the jet at the high flow rates?

Recommendations

(1) Develop a computer code which would allow greater flexibility in grid coverage, specifically an algorithm capable of variable grid size. This would allow the room to be better covered by the computational mesh and a finer grid could be used at the inlet.

(2) Perform simulations with varying turbulent parameters.

(3) Perform simulations on a typical personal computer to further investigate the feasibility of CFD use in a typical design situation.

(4) Better experimental data would allow a more extensive comparison to be made. The measurement of velocities, rather than velocity magnitudes, would be beneficial. Other desired modifications would include a finer experimental grid and the collection of measurements at the inlet.

(5) Investigate different algorithms for predicting convective heat transfer at the walls.

(6) Investigate the implementation of a contaminant transport model for use in studying indoor air quality.

(7) Investigate the simulation of ceiling diffusers to determine what numerical difficulties might arise when attempting to model the Coanda effect.

REFERENCES

Awbi, H.B. (1989). "Application of Computational Fluid Dynamics in Room Ventilation." Building and Environment. Vol. 24, No. 1. 1989.

Baker, A.J. and R.M. Kelso. (1990). "On Validation of Computational Fluid Dynamics Procedures for Room Air Motion Prediction." ASHRAE Transactions. Vol. 96, No. 1.

Chen, Q., A. Moser, and A. Huber. (1990). "Prediction of Buoyant, Turbulent Flow by a low-Reynolds Number k-ε Model." ASHRAE Transactions. Vol. 96, Pt. 1.

Gosman, A.D., P.V. Nielsen, A. Restivo, and J.H. Whitelaw. (1980). "The Flow Properties of Rooms with Small Ventilation Openings." Journal of Fluids Engineering. Vol. 102.

Harlow, F.H. and J.E. Welch. (1965). "Numerical Calculation of Time-Dependent Viscous Incompressible Flow of Fluid with Free-Surface." The Physics of Fluids. Vol. 8, No. 13.

Hinze, J.O. (1987). Turbulence (2nd Edition). McGraw-Hill. New York.

Hirt, C.W. and J.L. Cook. (1972). "Calculating Three-Dimensional Flows Around Structures and over Rough Terrain." Journal of Computational Physics. Vol. 10.

Hirt, C.W., B.D. Nichols, and N.C. Romero. (1975). "SOLA - A Numerical Solution Algorithm for Transient Fluid Flows." Report LA-5852, Los Alamos Scientific Laboratory.

Lam, C.G. and K. Bremhorst. (1981). "A Modified Form of the k-ε Model for Predicting Wall Turbulence." ASME Transactions. Vol. 103.

Launder, B.E. and D.B. Spalding. (1974). "The Numerical Computation of Turbulent Flows." Computer Methods in Applied Mechanics and Engineering. Vol. 3.

Lilley, D.G. (1988). "Three-Dimensional Flow Prediction for Industrial Mixing." ASME International Computers in Engineering Conference.

Lilley, D.G. (1991). Personal Communications. Oklahoma State University.

Murakami, S., S. Kato, and Y. Suyama. (1987). "Three-Dimensional Numerical Simulation of Turbulent Airflow in a Ventilated Room by Means of a Two-Equation Model." ASHRAE Transactions. Vol. 93, Pt. 2.

Murakami, S. and S. Kato. (1989). "Numerical and Experimental Study on Room Airflow. 3-D Predictions using the k-ε Turbulence Model." Building and Environment. Vol. 24, No. 1.

Murakami, S., S. Kato, and Y. Suyama. (1989). "Numerical Study on Diffusion Field as Affected by Arrangement of Supply and Exhaust Openings in Conventional-Flow-Type Clean Room." ASHRAE Transactions. Vol. 95, Pt. 2.

Murakami, S., S. Kato, and Y. Ishida. (1989). "3-D Numerical Simulation of Turbulent Air Flow in and Around Buildings Based on the k-ε Model with Generalized Curvilinear Coordinates." ASHRAE Transactions. Vol. 95, Pt. 2.

Murakami, S., S. Kato, and Y. Suyama. (1990). "Numerical Study of Flow and Contaminant Diffusion Fields as Affected by Flow Obstacles in Conventional-Flow-Type Clean Room." ASHRAE Transactions. Vol. 96, Pt. 2.

Nielsen, P.V., A. Restivo, and J.H. Whitelaw. (1978). "The Velocity Characteristics of Ventilated Rooms." Journal of Fluids Engineering. Vol. 100.

Patel, V.C., W. Rodi, and G. Scheurer. (1984). "Turbulent Models for Near-Wall and low-Reynolds Number Flows: A Review." AIAA Journal. Vol. 23, No. 9.

Rodi, W. (1980). "Turbulence Models for Environmental Problems." Prediction Methods for Turbulent Flows. W. Kollman, ed. Hemisphere/McGraw-Hill. New York.

Shih, T.M. (1984). Numerical Heat Transfer. Hemisphere Publishing Company. New York.

Spitler, J.D. (1990). "An Experimental Investigation of Air Flow and Convective Heat Transfer in Enclosures Having Large Ventilative Rates." Ph.D. Thesis. Department of Mechanical and Industrial Engineering, University of Illinois at Urbana-Champaign.

Spitler, J.D., C.O. Pederson, D.E. Fisher, P.F. Menne, and J. Cantillo. (1991). "An Experimental Facility for Investigation of Interior Convective Heat Transfer." ASHRAE Transactions. Vol. 97, Pt. 1.

APPENDIXES

APPENDIX A

FINITE-DIFFERENCE REPRESENTATIONS OF VELOCITIES

In Chapter 2, the finite-difference approximation was given for the explicit equation for the time-advanced x-component of velocity (U). The following are the equations and finite-difference representations of the other components of velocity. These details have been extracted from the earlier studies of Lilley [1988 and 1991].

$$\tilde{V}_{i,j,k} = V_{i,j,k} + \Delta t\left[\frac{1}{\Delta x}(P_{i,j,k} - P_{i,j+1,k}) + g_y + \text{VISY} - \text{FVX} - \text{FVY} - \text{FVZ}\right] \tag{A-1}$$

$$\text{FVX} = \frac{1}{4\Delta x}\Big\{ (U_{i,j,k}+U_{i,j+1,k})(V_{i,j,k} + V_{i+1,j,k}) + \hat{\alpha}|U_{i,j,k}+U_{i,j+1,k}|(V_{i,j,k}-V_{i+1,j,k}) \\ - (U_{i-1,j,k}+U_{i,j,k})(V_{i-1,j,k}+V_{i,j,k}) - \hat{\alpha}|U_{i-1,j,k}+U_{i-1,j+1,k}|(V_{i-1,j,k}-V_{i,j,k}) \Big\} \tag{A-2}$$

$$\text{FVY} = \frac{1}{4\Delta y}\Big\{ (V_{i,j,k}+V_{i+1,j,k})^2 + \hat{\alpha}|V_{i,j,k}+V_{i,j+1,k}|(V_{i,j,k}-V_{i,j+1,k}) \\ - (V_{i,j-1,k}+V_{i,j,k})^2 - \hat{\alpha}|V_{i,j-1,k}+V_{i,j,k}|(V_{i,j-1,k}-V_{i,j,k}) \Big\} \tag{A-3}$$

$$\text{FVZ} = \frac{1}{4\Delta z}\Big\{ (W_{i,j,k}+W_{i,j+1,k})(V_{i,j,k}+V_{i,j,k+1}) + \hat{\alpha}|W_{i,j,k}+W_{i,j+1,k}|(V_{i,j,k}-V_{i,j,k+1}) \\ - (W_{i,j,k-1}+W_{i,j+1,k-1})(V_{i,j,k-1}+V_{i,j,k}) - \hat{\alpha}|W_{i,j,k-1}+W_{i,j+1,k-1}|(V_{i,j,k-1}-V_{i,j,k}) \Big\} \tag{A-4}$$

$$\text{VISY} = \nu\Big\{ \frac{1}{\Delta x^2}(V_{i+1,j,k}-2V_{i,j,k}+V_{i-1,j,k}) + \frac{1}{\Delta y^2}(V_{i,j+1,k}-2V_{i,j,k}+V_{i,j-1,k}) \\ + \frac{1}{\Delta z^2}(V_{i,j,k+1}-2V_{i,j,k}+V_{i,j,k-1}) \Big\} \tag{A-5}$$

$$\tilde{V}_{i,j,k} = V_{i,j,k} + \Delta t\left[\frac{1}{\Delta x}(P_{i,j,k} - P_{i,j+1,k}) + g_y + \text{GAMMAY} - \text{FVX} - \text{FVY} - \text{FVZ}\right] \tag{A-6}$$

$$\tilde{W}_{i,j,k} = W_{i,j,k} + \Delta t\left[\frac{1}{\Delta x}(P_{i,j,k} - P_{i,j,k+1}) + g_z + \text{VISZ} - \text{FWX} - \text{FWY} - \text{FWZ}\right] \tag{A-7}$$

$$\text{FWX} = \frac{1}{4\Delta x}\{(U_{i,j,k}+U_{i,j,k+1})(W_{i,j,k} + W_{i+1,j,k}) + \hat{\alpha}|U_{i,j,k}+U_{i,j,k+1}|(W_{i,j,k}-W_{i+1,j,k}) \tag{A-8}$$
$$- (U_{i-1,j,k}+U_{i-1,j,k+1})(W_{i-1,j,k}+W_{i,j,k}) - \hat{\alpha}|U_{i-1,j,k}+U_{i-1,j,k+1}|(W_{i-1,j,k}-W_{i,j,k})\}$$

$$\text{FWY} = \frac{1}{4\Delta y}\{(V_{i,j,k}+V_{i,j,k+1})(W_{i,j,k}+W_{i,j+1,k}) + \hat{\alpha}|V_{i,j,k}+V_{i,j,k+1}|(W_{i,j,k}-W_{i,j+1,k}) \tag{A-9}$$
$$- (V_{i,j-1,k}+V_{i,j-1,k+1})(W_{i,j-1,k}+W_{i,j,k}) - \hat{\alpha}|V_{i,j-1,k}+V_{i,j-1,k+1}|(W_{i,j-1,k}-W_{i,j,k})\}$$

$$\text{FWZ} = \frac{1}{4\Delta z}\{(W_{i,j,k}+W_{i,j,k+1})^2 + \hat{\alpha}|W_{i,j,k}+W_{i,j,k+1}|(W_{i,j,k}-W_{i,j,k+1}) \tag{A-10}$$
$$- (W_{i,j,k-1}+W_{i,j,k})^2 - \hat{\alpha}|W_{i,j,k-1}+W_{i,j,k}|(W_{i,j,k-1}-W_{i,j,k})\}$$

$$\text{VISZ} = \nu\left\{\frac{1}{\Delta x^2}(W_{i+1,j,k}-2W_{i,j,k}+W_{i-1,j,k}) + \frac{1}{\Delta y^2}(W_{i,j+1,k}-2W_{i,j,k}+W_{i,j-1,k}) \right. \tag{A-11}$$
$$\left. + \frac{1}{\Delta z^2}(W_{i,j,k+1}-2W_{i,j,k}+W_{i,j,k-1})\right\}$$

$$\tilde{W}_{i,j,k} = W_{i,j,k} + \Delta t\left[\frac{1}{\Delta x}(P_{i,j,k} - P_{i,j,k+1}) + g_z + \text{GAMMAZ} - \text{FWX} - \text{FWY} - \text{FWZ}\right] \tag{A-12}$$

APPENDIX B

FINITE-DIFFERENCE REPRESENTATIONS OF FIRST DERIVATIVES

For any value (ϕ), its first derivative with respect to a spatial coordinate ($\partial\phi/\partial x$) may be approximated by one of several ways. Two of these ways are referred to as the forward and backward difference approximations, which are shown in the following equations.

Forward Difference

$$\frac{\partial \phi}{\partial x} \approx \frac{1}{\Delta x}(\phi_{i+1} - \phi_i) \tag{B-1}$$

Backward Difference

$$\frac{\partial \phi}{\partial x} \approx \frac{1}{\Delta x}(\phi_i - \phi_{i-1}) \tag{B-2}$$

Both of the equations may be expressed in the following general form.

$$\frac{\partial \phi}{\partial x} \approx \frac{1}{\Delta x}(A\phi_{i-1} + B\phi_i + C\phi_{i+1}) \tag{B-3}$$

where A=0, B=-1, C=1 for forward difference
A=-1, B=1, C=0 for backward difference

"Cross derivatives" may be represented in a similar manner.

$$\frac{\partial^2 \phi}{\partial x \partial y} \approx \frac{1}{\Delta x \Delta y}\left[A(\phi_{i-1,j-1} - \phi_{i-1,j} - \phi_{i,j-1}) + B\phi_{i,j} + C(\phi_{i+1,j+1} - \phi_{i,j+1} + \phi_{i+1,j})\right] \tag{B-4}$$

Rather than strictly use either the forward or backward difference method, this investigation will alternate the two methods for approximating the first derivatives, based on the simulation time step. It is very important to note that this method is only applied for the source terms of the equations (i.e., the terms generally appearing on the right-hand side of the partial differential equations).

For odd time steps, the forward difference method will be used. Conversely, even time steps will use the backward difference method.

Using these expressions, the various derivative terms discussed earlier in the report may be expanded and defined.

$$\Theta(k) = \frac{\partial}{x_j}\left(\frac{\nu_t \partial k}{\sigma_k \partial x_j}\right)$$
$$= \frac{\nu_t}{\sigma_k}\left(\frac{\partial^2 k}{\partial x^2}+\frac{\partial^2 k}{\partial y^2}+\frac{\partial^2 k}{\partial z^2}\right)+\frac{1}{\sigma_k}\left(\frac{\partial \nu_t \partial k}{\partial x \partial x}+\frac{\partial \nu_t \partial k}{\partial y \partial y}+\frac{\partial \nu_t \partial k}{\partial z \partial z}\right)$$

$$Q(\varepsilon) = \frac{\partial}{x_j}\left(\frac{\nu_t \partial \varepsilon}{\sigma_\varepsilon \partial x_j}\right)$$
$$= \frac{\nu_t}{\sigma_\varepsilon}\left(\frac{\partial^2 \varepsilon}{\partial x^2}+\frac{\partial^2 \varepsilon}{\partial y^2}+\frac{\partial^2 \varepsilon}{\partial z^2}\right)+\frac{1}{\sigma_\varepsilon}\left(\frac{\partial \nu_t \partial \varepsilon}{\partial x \partial x}+\frac{\partial \nu_t \partial \varepsilon}{\partial y \partial y}+\frac{\partial \nu_t \partial \varepsilon}{\partial z \partial z}\right)$$

$$\Pi = \frac{\partial U_i}{\partial x_j}\left(\frac{\partial U_i}{\partial x_j}+\frac{\partial U_j}{\partial x_i}\right)$$
$$= 2\left(\frac{\partial U}{\partial x}\right)^2+\frac{\partial U}{\partial y}\left(\frac{\partial U}{\partial y}+\frac{\partial V}{\partial x}\right)+\frac{\partial U}{\partial z}\left(\frac{\partial U}{\partial z}+\frac{\partial W}{\partial x}\right)$$
$$+\frac{\partial V}{\partial x}\left(\frac{\partial V}{\partial x}+\frac{\partial U}{\partial y}\right)+2\left(\frac{\partial V}{\partial y}\right)^2+\frac{\partial V}{\partial z}\left(\frac{\partial V}{\partial z}+\frac{\partial W}{\partial y}\right)$$
$$+\frac{\partial W}{\partial x}\left(\frac{\partial W}{\partial x}+\frac{\partial U}{\partial z}\right)+\frac{\partial W}{\partial y}\left(\frac{\partial W}{\partial y}+\frac{\partial V}{\partial z}\right)+2\left(\frac{\partial W}{\partial z}\right)^2$$

$$\Gamma_i = \frac{\partial}{\partial x_j}\left(\nu_t\left(\frac{\partial U_i}{\partial x_j}+\frac{\partial U_j}{\partial x_i}\right)-\frac{2}{3}k\delta_{ij}\right)$$

$$\Gamma_x = -\frac{2\partial k}{3\partial x}+\nu_t\left(2\frac{\partial^2 U}{\partial x^2}+\frac{\partial^2 U}{\partial y^2}+\frac{\partial^2 U}{\partial z^2}+\frac{\partial^2 V}{\partial x \partial y}+\frac{\partial^2 W}{\partial x \partial z}\right)+2\frac{\partial \nu_t \partial U}{\partial x \partial x}+\frac{\partial \nu_t}{\partial y}\left(\frac{\partial U}{\partial y}+\frac{\partial V}{\partial x}\right)+\frac{\partial \nu_t}{\partial z}\left(\frac{\partial U}{\partial z}+\frac{\partial W}{\partial x}\right)$$

$$\Gamma_y = -\frac{2\partial k}{3\partial y} + \nu_t\left(\frac{\partial^2 V}{\partial x^2} + 2\frac{\partial^2 V}{\partial y^2} + \frac{\partial^2 V}{\partial z^2} + \frac{\partial^2 U}{\partial x \partial y} + \frac{\partial^2 W}{\partial y \partial z}\right) + \frac{\partial \nu_t}{\partial x}\left(\frac{\partial V}{\partial x} + \frac{\partial U}{\partial y}\right) + 2\frac{\partial \nu_t \partial V}{\partial y \partial y} + \frac{\partial \nu_t}{\partial z}\left(\frac{\partial V}{\partial z} + \frac{\partial W}{\partial y}\right)$$

$$\Gamma_z = -\frac{2\partial k}{3\partial z} + \nu_t\left(\frac{\partial^2 W}{\partial x^2} + \frac{\partial^2 W}{\partial y^2} + 2\frac{\partial^2 W}{\partial z^2} + \frac{\partial^2 U}{\partial x \partial z} + \frac{\partial^2 V}{\partial y \partial z}\right) + \frac{\partial \nu_t}{\partial x}\left(\frac{\partial W}{\partial x} + \frac{\partial U}{\partial z}\right) + \frac{\partial \nu_t}{\partial y}\left(\frac{\partial W}{\partial y} + \frac{\partial V}{\partial z}\right) + 2\frac{\partial \nu_t \partial W}{\partial z \partial z}$$